REGISTRATION-BASED MOTION AND DEFORMATION ANALYSIS OF CARDIOVASCULAR IMAGE SEQUENCES

Estanislao Oubel

The cover image design by
Estanislao Oubel
Milton Hoz de Vila

Copyright ©2009 by E. Oubel. All rights reserved.
No part of this publication may be reproduced in any form by print, photocopy, digital format or by any other means without prior written permission of the author.

ISBN XX-XXX-XXXX-X

Printed by

PHD THESIS

REGISTRATION-BASED MOTION AND DEFORMATION ANALYSIS OF CARDIOVASCULAR IMAGE SEQUENCES

Estanislao Oubel

UNIVERSIDAD DE ZARAGOZA
Instituto de Investigación en Ingeniería de Aragón

BIOMEDICAL ENGINEERING
Joint PhD Program from Universidad de Zaragoza and Universitat Politécnica de Catalunya

Thesis Director: **Dr. Alejandro F. Frangi**
Universitat Pompeu Fabra, Barcelona, Spain

Reading Committee:

The research described in this thesis was carried out at the research group for Computational Imaging and Simulation Technologies in Biomedicine (CISTIB), UPF, Barcelona. This work was funded by a FPU scholarship (AP2003-1535) from the Spanish Ministry of Education

Introduction

The estimation of morphological changes of biological tissues over time is an ubiquitous problem in medical imaging. Image registration methods are suitable to solve this kind of problems since they allow to establish dense point correspondences between images, which in turn can be used to quantify deformation. Given a discrete image sequence $I(\mathbf{x}, t) = I(\mathbf{x}, 0), I(\mathbf{x}, 1) \cdots, I(\mathbf{x}, N-1)$, in the context of this thesis, sequence registration means to find a transformation $\mathbf{T}(\mathbf{x}, t) : (\mathbf{x}, 0) \rightarrow (\mathbf{x}', t)$ that puts into correspondence points belonging to the same sequence. This term must not be confused with its meaning in the context of intersubject sequence registration [1], where the objective is to find a transformation $\mathbf{T_{12}}(\mathbf{x_1}, t_1) : (\mathbf{x_1}, t_1) \rightarrow (\mathbf{x_2}, t_2)$ that establishes correspondences between points of different sequences $I_1(\mathbf{x_1}, t_1)$ and $I_2(\mathbf{x_2}, t_2)$. In this thesis we have focused on two challenging applications such as wall motion estimation in cerebral aneurysms from Digital Subtraction Angiography (DSA), and deformation estimation of the heart from Tagged Magnetic Resonance Imaging (T-MRI) [2, 3]. Figures 1 and 2 show examples of the images used in this thesis.

The quantification of pulsation in cerebral aneurysms is important for studying the connection between haemodynamics and rupture. One of the hypothesis that explain the rupture of aneurysms is the stress concentration on the vessel wall. This can be quantified by computing wall shear stress values from computational fluid dynamics (CFD) simulations. Wall motion information can be used in this context to impose boundary conditions in CFD simulations performed on non-rigid models as described in Chapter 1.

Wall motion estimation in cerebral aneurysms is also important since the potential connection between pulsation and risk of rupture, as reported in [4–6]. The underlying hypothesis is that rupture owes to a weakness of the vessel wall, which

should change the pulsation amplitude of the aneurysm. To study the interrelationships between rupture and pulsation it is necessary to quantify this pulsation, which can be performed by measuring displacements of the vessel wall over the cardiac cycle.

Most of wall motion values reported in the literature correspond to experiments with phantoms [5, 7], simulated images [8], or experimental models [9]. Only a few attempts of in-vivo quantification have been reported in human beings [4, 10]. In this thesis we have developed an automatic method to quantify wall motion in cerebral aneurysms from DSA sequences. This method was then applied to study the relationship between rupture status and pulsation (Chapter 2).

Methods for cardiac deformation estimation are important for studying the behavior of the heart under normal, pathological, and simulated conditions. Among other applications, these methods are useful for studying the mechanical effects of cardiac diseases [11] and for the development of electro-mechanical models. Pairwise registration maximizing the Mutual Information (MI) between component volumes of T-MRI sequences has been successfully applied for recovering displacement fields of the heart [12, 13]. This motivated us to study extensions of methods based on information theory both for inclusion of spatial and temporal information.

Normally, the similarity metrics used in image registration methods are based on pixel intensity information. Such metrics ignore spatial information in the pixel neighborhood that could provide valuable information for guiding the registration process. We have explored the use of metrics based on wavelets transforms for non rigid registration of 2D T-MRI sequences (Chapter 3).

Joint sequence registration refers to the simultaneous alignment of all the frames in the sequence, opposite to the pairwise approach in which all frames are successively registered (one by one) to the first (or previous) one of the sequence. We have developed a novel method for recovering cardiac displacement fields by joint alignment of T-MRI sequences (Chapter 4), and applied it for studying regional strain differences between patients with myocardial infarction and a group of healthy subjects (Chapter 5).

The results of this research have been presented in several conferences, and submitted to scientific journals for their publication. A list of these publications can be found after the Chapter 5. In the same list, we have added other publications resulting from colaborations with external groups, to which we have contributed with the experience obtained during these years in the field of image registration.

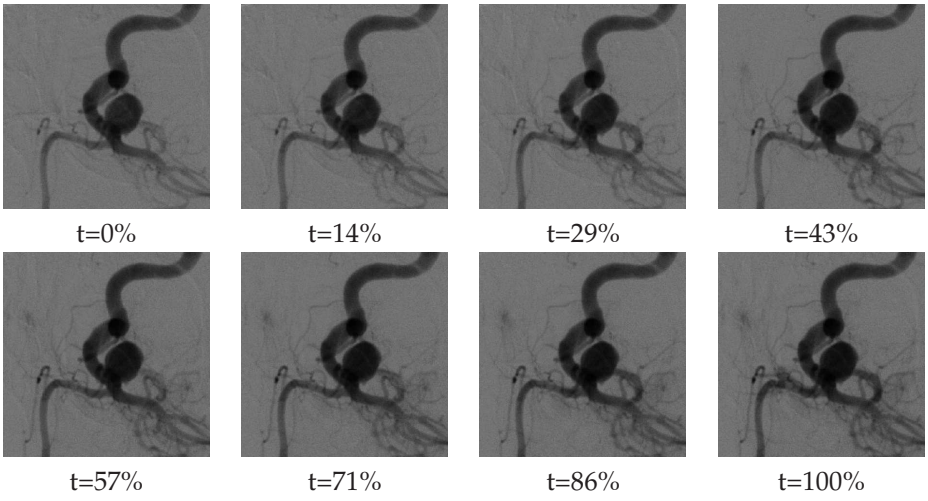

Figure 1: Example of a DSA sequence showing an aneurysm along the cardiac cycle. Time is expressed as a percent of the cardiac cycle.

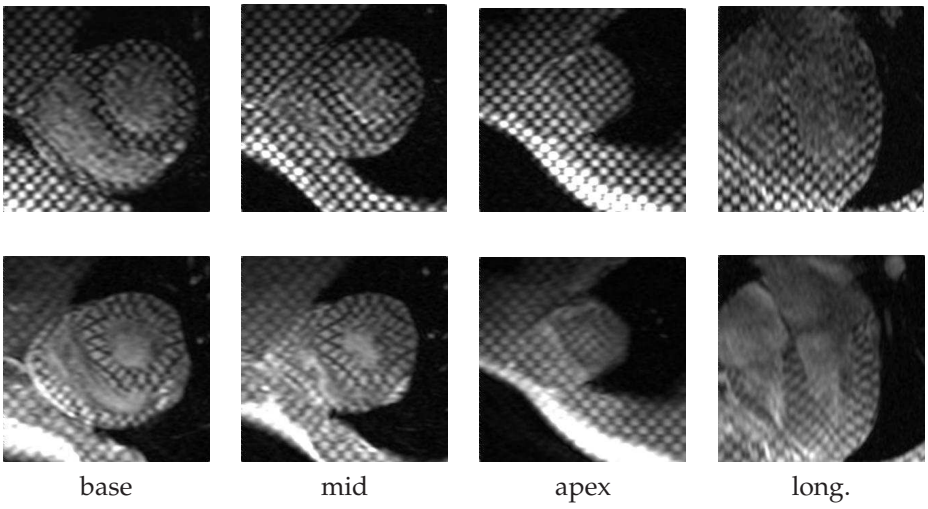

Figure 2: Example of T-MRI sequences of the heart. From left to right: basal, medial, apical, and longitudinal planes. Top row corresponds to End-of-Diastole (ED) and bottom row to End-of-Systole (ES).

Contents

List of Figures

List of Tables

Nomenclature

MI_α	Alpha mutual information
3D-RA	3D rotational angiography
4D-CTA	4D computed tomography angiography
kNNG	k -Nearest Neighbors Graph
ACA	Anterior cerebral artery
ACom	Anterior communicating artery
AMI	Acute myocardial infarction
AR	Aspect ratio
BA	Basilar artery
C-MRI	Cine magnetic resonance imaging
CC	Cardiac catheterization
CCA	Common carotid artery
CF	Concentration factor
CFD	Computational fluid dynamics
CoW	Circle of Willis
CSPAMM	Complimentary spatial modulation of magnetization

CWT	Complex wavelet transform
CX	Circumflex coronary artery
DE-MRI	Delay enhancement magnetic resonance imaging
DFT	Discrete Fourier transform
DSA	Digital subtraction angiography
DWT	Discrete wavelet transform
ED	End-of-diastole
EF	Ejection fraction
ES	End-of-systole
HARP	Harmonic phase
ICA	Internal carotid artery
IR	Image registration
JA	Joint alignment
LAD	Left anterior descending artery
LV	Left ventricle
MCA	Middle cerebral artery
MI	Mutual information
MSE	Mean squared error
MST	Minimum spanning tree
NMI	Normalized mutual information
NWSS	Normalized wall shear stress
OF	Optical flow
PA	Pairwise alignment
PC-MR	Phase-contrast magnetic resonance
PC-MRA	Phase-contrast magnetic resonance angiography
PCA	Principal component analysis

PCom	Posterior communicating artery
PD-US	Power Doppler ultrasound
PDF	Probability density function
RCA	Right coronary artery
RV	Right ventricle
SE-MRI	Strain-encoded magnetic resonance imaging
SNR	Signal-to-Noise ratio
SPAMM	Spatial modulation of magnetization
T-MRI	Tagged magnetic resonance imaging
WSS	Wall shear stress

CHAPTER 1

Compliant models for CFD simulations in intracranial aneurysms

Abstract - *Haemodynamics, and in particular wall shear stress, is thought to play a critical role in the progression and rupture of intracranial aneurysms. A novel method is presented that combines image-based wall motion estimation obtained through non-rigid registration with computational fluid dynamics (CFD) simulations in order to provide realistic intra-aneurysmal flow patterns and understand the effects of deforming walls on the haemodynamic patterns. In contrast to previous approaches, which assume rigid walls or ad hoc elastic parameters to perform the CFD simulations, wall compliance has been included in this study through the imposition of measured wall motions. This circumvents the difficulties in estimating personalized elasticity properties. Although variations in the aneurysmal haemodynamics were observed when incorporating the wall motion, the overall characteristics of the wall shear stress distribution do not seem to change considerably. Further experiments with more cases will be required to establish the clinical significance of the observed variations.*

Adapted from L. Dempere-Marco, E. Oubel, M. Castro, C. Putman, A. F. Frangi, and J. R. Cebral. CFD Analysis Incorporating the Influence of Wall Motion: Application to Intracranial Aneurysms. In R. Larsen, M. Nielsen, and J. Sporring, editors, *8th International Conference on Medical Image Computing and Computer-Assisted Intervention (MICCAI'06)*, Copenhagen, Denmark: Springer, October 2006, pp. 438-45.

1.1 Introduction

Intracranial aneurysms are pathological dilations of cerebral arteries, which tend to occur at or near arterial bifurcations, mostly in the circle of Willis. The optimal management of unruptured aneurysms is controversial and current decision-making is mainly based on considering their size and location, as derived from the International Study of Unruptured Intracranial Aneurysms (ISUIA) [14]. However, it is thought that the interaction between haemodynamics and wall mechanics plays a critical role in the formation, growth and rupture of aneurysms. Although there is little doubt that arterial and aneurysmal walls do move under the physiologic pulsatile flow conditions [4], there is no accurate information on the magnitude and other motion characteristics required for understanding the interaction between the haemodynamics and the wall biomechanics. Visualization of aneurysmal pulsation seems to have become possible with the advent of 4D-CTA imaging techniques [15,16]. Confounding these observations, a number of imaging artifacts were present related to motion of bony structures [4]. Since there are no reliable techniques for measuring flow patterns in vivo, various modeling approaches were considered in the past [17,18]. Hitherto, most computational fluid dynamics (CFD) methods assume rigid walls due to a lack of information regarding both wall elasticity and thickness. Moreover, in order to perform simulations that account for the fluid-structure interaction, it is also necessary to prescribe the intra-arterial pressure waveform, which is not normally acquired during routine clinical exams. In this paper, wall motion is quantified by applying image registration techniques to dynamic X-ray images. To study the effects of wall compliance on the aneurysmal haemodynamics, the obtained wall motion is directly imposed to the 3D model derived from the medical images.

1.2 Method

1.2.1 Dataset

Three case studies have been considered in this paper. Each patient underwent conventional transfemoral catheterization and cerebral angiography using a Philips Integris Biplane angiography unit. As part of this examination, a rotational acquisition was performed using a six seconds constant injection of contrast agent and a 180 degrees rotation at 15 frames per second over 8 seconds. These images were transferred to the Philips Integris Workstation and reconstructed into 3D voxel data using the standard proprietary software, which was used for generating a 3D anatomical model. Biplanar dynamic angiogram at 2 Hz was subsequently performed using a six second contrast injection for a period of at least 6 seconds. In addition, an expert neuroradiologist measured the diameters D1 and D2 (maxi-

mum height and width, respectively) on these projection views. This information was then used to establish the pixel size and to quantify the wall motion.

1.2.2 Wall motion estimation

In order to estimate the wall motion, image registration, which establishes correspondences between points in two different images, was applied to the series of 2D images. To this end, a 2D version of the non-rigid registration algorithm proposed by Rueckert *et al*. [19] was applied. This method is based on free-form deformations, which are modeled through the 2D tensor product of 1D cubic B-splines. By moving a set of control points originally distributed into a regular lattice, a smooth and continuous transformation is obtained that is subsequently used for deforming one image into the other. The control points are moved in order to maximize the similarity between the two images. The similarity metric used in this study to characterize the alignment between the two images is the Normalized Mutual Information (NMI) [20].

For each series of sequential X-ray projection images, a set of landmarks were manually delineated in the first frame, and subsequently propagated by using the transformations derived from the image registration procedure. The complete series was registered to the initial reference frame. Thus, wall motion was estimated from the propagated landmarks by calculating the distance between corresponding points. A distribution of displacement vectors was obtained for the complete set of landmarks. The wall motion was estimated by using two assumptions: differential motion (i.e. different amplitude for different regions), and uniform motion (i.e. same amplitude for all regions). Thus, the statistical characterization of the displacement field was performed on the whole aneurysm and also on several different anatomical regions. In order to characterize the behavior of each region, both the median and the 90^{th} percentile of the displacement vector modulus were calculated. By considering the 90^{th} percentile, an upper boundary to the wall motion amplitude in the simulations is obtained while excluding outliers.

1.2.3 Compliant model

In order to compute the intra-aneurysmal flow patterns, personalized models of blood vessels were constructed from 3D rotational angiography (3DRA) images. The segmentation procedure was based upon the use of deformable models by first smoothing the image through a combination of blurring and sharpening operations, followed by a region growing segmentation and isosurface extraction. This surface was then used to initialize a deformable model under the action of internal smoothing forces and external forces from the gradients of the original unprocessed images [17]. The anatomical model was subsequently used as a support surface to generate a finite element grid with an advancing front method that first

re-triangulates the surface and then marches into the domain generating tetrahedral elements [21]. The blood flow was mathematically modeled by the unsteady Navier-Stokes equations for an incompressible fluid:

$$\nabla \cdot \mathbf{v} = 0,\ \rho \left(\frac{\partial \mathbf{v}}{\partial t} + \mathbf{v} \cdot \nabla \mathbf{v} \right) = -\nabla p + \nabla \cdot \boldsymbol{\tau} \tag{1.1}$$

where ρ is the density, v is the velocity field, p is the pressure, and τ is the deviatoric stress tensor. The fluid was assumed Newtonian with a viscosity of $\mu = 4$ cPoise and a density of $\rho = 1.0$ g/cm3. The blood flow boundary conditions were derived from PC-MR images of the main branches of the circle of Willis obtained from a normal volunteer. Traction free boundary conditions were imposed at the model outflows. At the vessel walls, no-slip boundary conditions were applied. Since the velocity of the wall was estimated through imaging techniques, wall compliance is implicitly included in the simulation process. As it was not possible to determine the shape of the distension waveform at low sampling rates, it was assumed as a first order approximation, that it followed the flow waveform. Such waveform was scaled locally to achieve the measured displacement amplitude in each of the regions considered. The walls were assumed to move in the normal direction, and such motion was directly imposed to the 3D mesh derived from the volumetric medical images. The grid was updated at each time step by a non-linear smoothing of the wall velocity into the interior of the computational domain [22].

1.3 Results

In Figure 1.1, the results from the segmentation of the 3DRA medical images for the three cases considered in this study are displayed. To establish whether the detected motion could be discriminated from the intra-observer variability in delineating contours, a manual segmentation was performed by an expert observer in the first frame by selecting closely located points on the boundary of the aneurysm and subsequently fitting a spline to the series of points. By considering also the independently selected landmarks for this same frame, the distributions of distances derived from: a) original landmarks to the spline, and b) propagated landmarks and original landmarks, were compared. To this end, Student paired t-test and ranked sum Wilcoxon tests were performed. As established before, the landmarks were tracked in the complete series in order to quantify the wall motion. Figure 1.2 illustrates the landmarks propagation from which wall deformation estimates follow. The amplitude of the motion is characterized in Figure 1.3 by both the median and the 90^{th} percentile.

For patient #1, statistically significant differences were found between the two distributions for 8/11 frames ($p_{TTEST} < 0.04$, $p_{WIL} < 0.02$). In all of these cases, the average distance between propagated landmarks and original landmarks was

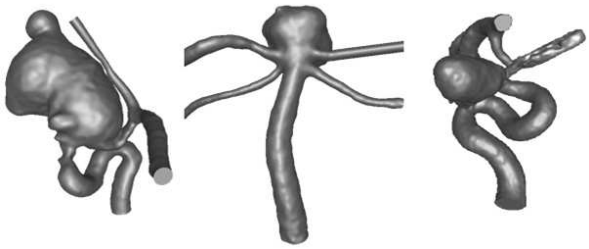

Figure 1.1: Segmented models corresponding to the 3DRA medical images considered in this study (from left to right: patient #1, patient #2, and patient #3).

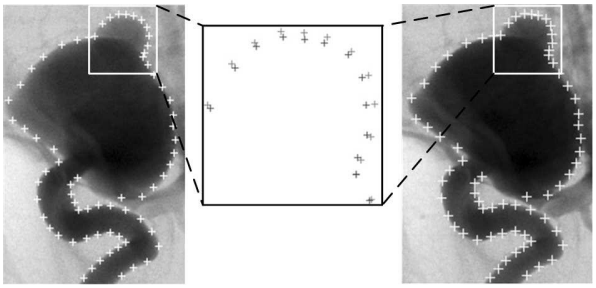

Figure 1.2: Illustration of the propagation of the landmarks between different frames. [left] patient #1-frame #1, [middle] zoom corresponding to region containing the lobule, [right] patient #1-frame #2.

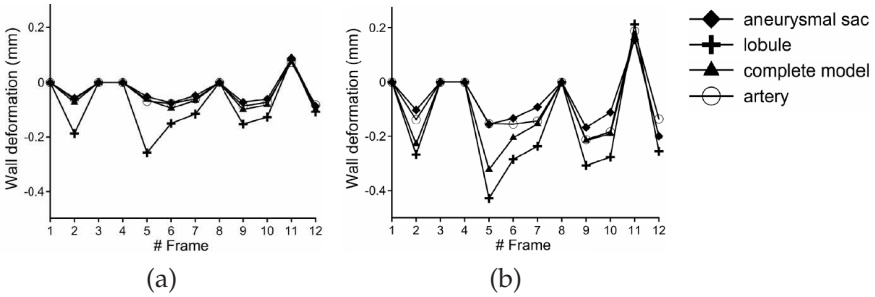

Figure 1.3: Estimation of wall deformation discriminated from intra-observer variability. (a) median of the modulus of the displacement vectors, and (b) 90^{th} percentile of the modulus of the displacement vectors for patient #1. The sign of the wall deformation indicates whether dilation (+) or contraction (-) is obtained, and a null deformation has been imposed to those frames for which wall deformation cannot be discriminated from intra-observer variability.

larger than that due to intra-observer variability. Thus, although small deformation fields are obtained for all the images within the temporal series (see Figure 1.2), these differ in a statistically meaningful way from the error made in the manual delineation of the contours. Pairwise one-way ANOVA analyses were also performed on the series defined by the median of the displacement of the landmarks for all the frames and statistically meaningful differences ($p < 0.004$) were found between the distribution corresponding to the lobule and the rest of distributions.

For patient #2, the deformations recovered by the registration algorithm required subpixel accuracy to be detected. In fact, statistically significant differences were found between the two distributions for $3/6$ frames ($p_{TTEST} < 0.02$, $p_{WIL} < 0.04$), however, the intra-observer variability was found to be larger than the average wall motion detected. Thus, it was concluded that the deformation field was so small that could not be reliably quantified given the available image resolution (i.e. maximum mean wall deformation of 0.07 mm in the temporal series).

For patient #3, the deformation fields obtained yielded statistically significant differences for $6/9$ ($p_{TTEST} < 0.04$, $p_{WIL} < 0.03$) frames, with the average wall deformation larger than the error due to intra-observer variation. The amplitude of the maximum displacement observed was 0.25 mm, i.e. about 3% of the aneurysm diameter, with no significant differences between regions.

A total of five simulations were carried out for patient #1, using different vessel wall velocity conditions: 1) maximum displacement (i.e. 90^{th} percentile), differential motion, 2) maximum displacement, uniform motion, 3) median displacement, differential motion, 4) median displacement, uniform motion, and 5) rigid walls. For patients #2 and #3, a compliant and a rigid simulation were carried out. Since for patient #2 it was not possible to detect a significant wall deformation, a uniform wall motion with amplitude just below the resolution of the technique was used for the compliant model. For patient #3, only the maximum uniform wall motion was imposed in the elastic model to assess the maximum effect that wall motion would have. In order to compare the results obtained with the different vessel wall movements, the following characterization of the wall shear stress (WSS) was used: the necks of the aneurysms were manually selected on the anatomical models, and a region of approximately 1 cm of the parent vessel (denoted proximal parent vessel) from the neck of the aneurysm was identified (see Figure 1.4). At each time instant, the average WSS magnitude was computed in the proximal parent vessel region and used to normalize the instantaneous WSS in the aneurysm and to identify regions of elevated WSS (NWSS>1). Table 1.1 shows the area of these regions, the percent of the total aneurysm shear force applied over these regions, and a "shear force concentration" factor (percentage of the shear force applied in these regions divided by the percent area of the regions), for each of the wall motion regimes considered and for each of the three patients.

Visualizations of the instantaneous WSS distribution at five selected instants during the cardiac cycle and for all the wall motion conditions of patient #1 are

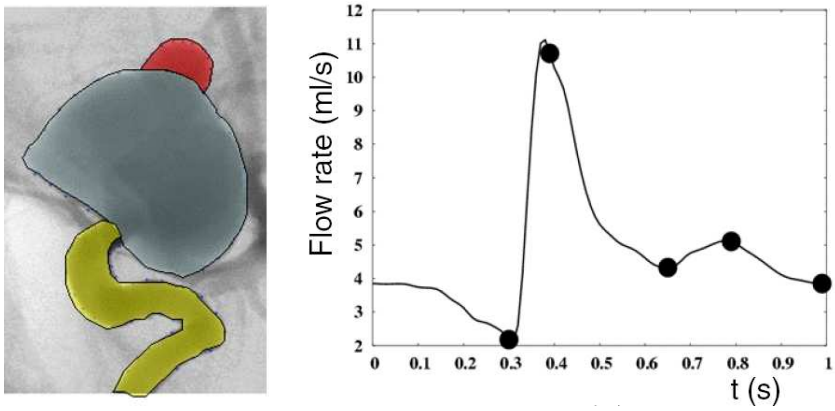

(a) (b)

Figure 1.4: (a) Aneurysm subdivision for differential wall motion estimation (vessel, sac and lobulation), and (b) flow waveform used to prescribe pulsatile velocity conditions at the inlet boundary of the models. The dots indicate the instants during the cardiac cycle at which flow visualizations are presented.

Table 1.1: Percent of the area of the aneurysm under elevated wall shear stress, percent of the shear force applied in this region, and concentration factor (CF) for each patient under different wall motion conditions. The values shown are time averages over the cardiac cycle.

Patient (#)	Conditions	Area (%)	Force (%)	CF
1	max diff	1.31	7.46	5.8
1	max unif	1.40	8.06	6.0
1	med diff	1.44	8.34	6.0
1	med unif	1.41	8.11	5.9
1	rigid	1.12	6.09	5.7
2	elastic	2.04	6.37	3.3
2	rigid	1.37	4.71	3.5
3	elastic	2.16	19.48	9.4
3	rigid	1.82	18.86	10.4

presented in Figure 1.5 . These visualizations and the data presented in Table 1.1 reveal a region of elevated WSS in the dome of the aneurysm. Although this region covers a small area of the aneurysm (1.4%), it contributes to a significant fraction of the total shear force (8%), i.e. it is subject to a "concentrated shear force". A graph of the WSS obtained with the rigid wall model and the compliant model with maximum differential wall motion is shown in Figure 1.7. This figure shows that rigid models tend to overestimate the WSS compared to the compliant models. However, the overall WSS distributions obtained with the different wall models have similar appearances and characteristics in spite of small local deviations. Visualizations of the instantaneous WSS distributions at the five selected instants during the cardiac cycle for patients #2 and #3 are presented in Figure 1.6. The results obtained with both compliant (maximum uniform wall deformation) and rigid models are shown. The visualizations reveal a stable region of elevated WSS in the dome of the aneurysm for patient #2. For patient #3, the region of elevated WSS expands from the neck to the dome of the aneurysm.

The regions of elevated WSS (i.e. WSS larger than the average WSS over the proximal parent vessel) cover approximately 2% of the area of the aneurysms for both patients #2 and #3. It is interesting to note that compliant models tend to yield slightly larger areas of elevated WSS. This may be due to lower WSS values in the proximal parent artery for distending vessels.

1.4 Discussion and conclusions

The purpose of this study was to introduce a novel way to combine image-based motion estimation with CFD analysis to better understand the effects of aneurysm wall compliance on intra-aneurysmal blood flow patterns. It has been proven that it is possible to determine wall motion from X-ray dynamic imaging through image registration. Furthermore, the reported global or regional estimates provide a basis for potentially more accurate compliant wall CFD simulations. This study adds further evidence to the results reported by [15,16] where wall motion was observed and found to be different in the bleb.

The methodology for wall motion estimation can be improved in a number of ways such as image acquisition at higher frame rates, use of larger catheters and higher contrast injection rates. Also, ideally the images could be gated to heart rate or temporally registered with arterial pressure waveforms. In this study, only low frame rate acquisitions were available. However, it is expected that with higher frame rates, the complete distension waveform will be reproduced, thus avoiding the need to assume any particular temporal function. Moreover, the structural differences between frames due to the passage of the bolus will be minimized. In fact, a potential limitation of this technique is that homogeneous mixing of the contrast cannot be assured at the current injection rates and catheter sizes. It is also

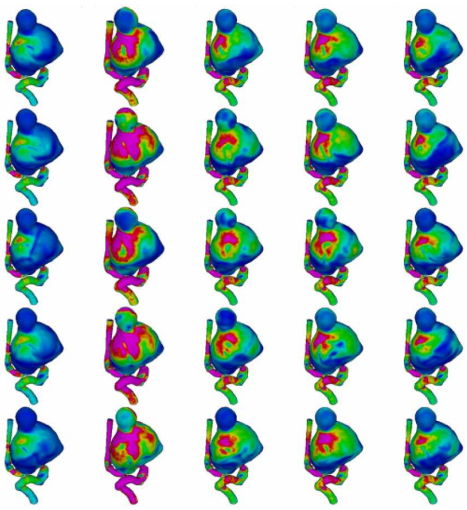

Figure 1.5: Instantaneous WSS distributions obtained with different wall motions. From top to bottom: 90^{th} percentile differential, 90^{th} percentile uniform, median differential, median uniform, and rigid walls. Each column corresponds to a time instant indicated in Figure 1.4 (b).

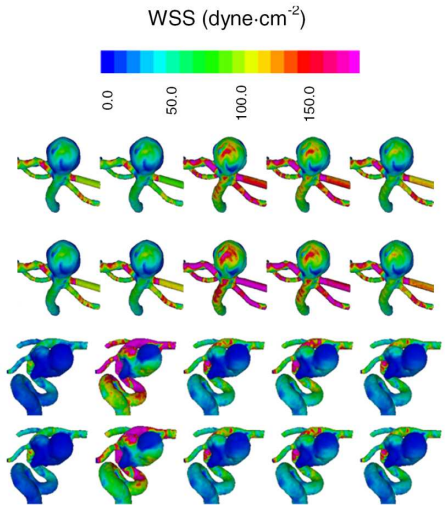

Figure 1.6: Instantaneous WSS distributions obtained for patient #2 (top panel) and #3 (bottom panel), using compliant walls (top row) and rigid walls (bottom row). Each column correspond to the time instants indicated in Figure 1.4 (b).

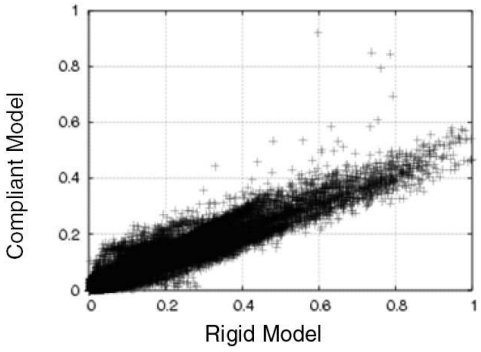

Figure 1.7: WSS obtained with different wall motions (rigid vs compliant walls) when 90^{th} percentile uniform motion is prescribed for patient #1.

expected that with the advent of new technological advances, an improvement in spatial resolution will follow and more subtle variations will therefore be detected.

When assessing the influence of wall motion on the haemodynamics, relatively small changes in the distribution of WSS were observed when imposing different wall motions. Point-wise comparisons of the WSS magnitudes obtained with the rigid and compliant models were carried out and it was observed that rigid models tended to over estimate the WSS magnitude. This effect was less pronounced when the wall motion was small. This result is in agreement with those reported by Shojima *et al.* [23]. In contrast, a number of haemodynamic characteristics did not exhibit substantial variations. For all patients, the compliant and rigid models provided consistent estimations of the location and size of the flow impaction zone. In particular, the area of the aneurysm that is under elevated wall shear stress with respect to the average WSS in the proximal parent vessel, the contribution to the total shear force of this region, and the shear force concentration factor were relatively unaffected by the wall motion. In addition, changing the amplitude of the wall motion or imposing differential rather than uniform deformations did not have a considerable effect on these variables either.

Although WSS is thought to play an important role on the mechanobiology of the arterial wall, further investigation is required to determine which haemodynamic variables are clinically relevant and the effect of wall motion on them. Finally, it is widely believed that aneurysmal wall is always compliant to some extent, however,the range of variability of wall motion among patients is still unknown. Studies with larger numbers of aneurysms are required to determine how common measurable wall motions are in the population at large and if differences in compliance can be related to clinical outcomes such as aneurysmal growth and rupture.

CHAPTER 2

Wall motion estimation in intracranial aneurysms

Abstract - *The quantification of wall motion in cerebral aneurysms is becoming important owing to its potential connection to rupture and its importance for computational fluid dynamics (CFD) simulations. Most of papers report values obtained with experimental phantoms, simulated images, or animal models, but the information for real patients is limited. In this chapter, we have combined non-rigid registration (IR) with signal processing techniques to measure pulsation in real patients from high frame rate digital subtraction angiography (DSA). We have obtained physiological meaningful waveforms with amplitudes in the range 0mm-0.3mm for a population of 18 patients including ruptured and unruptured aneurysms. Statistically significant differences in pulsation were found according to the rupture status, in agreement with differences in biomechanical properties reported in the literature. To our knowledge, this is the first time that wall motion is quantified in intracranial aneurysms, and that a potential connection with rupture status is established.*

Adapted from E. Oubel, J. R. Cebral, M. De Craene, R. Blanc, J. Blasco, J. Macho, C. M. Putman, and A. F. Frangi. Wall Motion Estimation of Intracranial Aneurysms From DSA Sequences. *Under review.*

2.1 Introduction

Intracranial aneurysms are pathological dilations of cerebral arteries, which tend to occur at or near arterial bifurcations, mostly in the Circle of Willis (CoW). The optimal management of unruptured aneurysms is controversial and current decision-making is mainly based on considering their size and location, as derived from the International Study of Unruptured Intracranial Aneurysms (ISUIA) [14]. It is thought that the interaction between haemodynamics and wall mechanics plays a critical role in the formation, growth and rupture of aneurysms. The quantification of wall motion in aneurysms is becoming important since its likely connection with rupture risk [4–6] and its importance for incorporating patient specific boundary conditions in CFD simulations [24].

Many of the reported values in the literature correspond to experiments with phantoms, simulated images, or experimental models [5,7–9]. Only a few attempts of in-vivo quantification have been reported. Wardlaw *et al.* [10] have measured pulsation *in vivo* by using Power Doppler Ultrasound (PD-US), and validated their method using phantoms [25]. However, many conclusions of the study with phantoms are valid for the large changes in size considered (42% of the cross section), but not necessary extendable for the small changes occurring in intracranial aneurysms. Meyer *et al.* [4] have measured aneurysmal volume changes by using Phase-Contrast Magnetic Resonance Angiography (PC-MRA). For ruptured aneurysms they obtained values of $51\% \pm 10\%$, which are quite large in comparison to the visual changes observed in our clinical experience. With the advent of ECG-gated 4D Computed Tomography Angiography (4D-CTA), the visualization of aneurysmal pulsation seems to have become feasible [6,15,16]. However, this technique presents helical motion artifacts resulting from the lack of cone beam correction during image reconstruction [26], which are visualized as a wavelike motion and produce the apparent movement of bony structures [15]. This observation and other inconsistencies about the presence of bleb pulsation have been pointed out by Matsumoto *et al.* [27]. These problems seem to be corrected with 64-slice CT scanners, but so far only studies of feasibility have been carried out with phantoms [7]. Recently, Zhang *et al.* [8] have presented a method to recover pulsation by deforming the 3D Rotational Angiography (3D-RA) rendered volume to match its projections to the 2D acquisitions used for the volumetric reconstruction. However, this technique has been tested only with phantom data and its application in human beings must still be proven. Table 2.1 summarizes the previous work.

Recently, we have presented preliminary results of the application of non rigid registration techniques to recover *in vivo* wall motion from Digital Subtraction Angiography (DSA) sequences [28]. In this chapter, we present an improved version of the method that solves some drawbacks of the initial approach. We have applied the technique to quantify wall motion in 15 patients and found a correlation between rupture and regional differences in pulsation. To our knowledge, this is the

Table 2.1: Previous work on wall motion quantification in cerebral aneurysms. R=Ruptured, U=Unruptured; WMO = Wall motion occurrence; WMQ = Wall motion quantification.

Authors	Modality	Data	Status	WMO[a]	WMQ
Hayakawa *et al.* [16]	4D-CTA	*in vivo*	All R	4/23	no
Kato *et al.* [6]	4D-CTA	*in vivo*	All U	2/15	no
Yaghmai *et al.* [7]	4D-CTA	phantom	-	-	yes
Boecher-Schwarz *et al.*[b] [9]	-	animal model	-	5/8	yes
Wardlaw *et al.* [10]	PD-US	*in vivo*	All R	15/16	yes
Ueno *et al.* [5]	PD-US	phantom	-	-	yes
Meyer *et al.* [4]	PC-MRI	*in vivo*	6 R / 10 U	15/16	yes
Zhang *et al.* [8]	3D-RA	phantom	-	-	yes

[a]Wall motion occurrence is the ratio between the number of cases that present pulsation and the total number of cases.

[b]The modality is not specified since the authors used an experimental system in which the aneurysmal pulsation is measured by a laser displacement sensor.

first time that the pulsation of intracranial aneurysms is quantified over time, and that a connection with rupture is established.

2.2 Method

2.2.1 Dataset

Figure 2.1 shows the DSA sequences used in this paper. These sequences were acquired in three clinical centers: 1) Department of Interventional Neuroradiology, Inova Fairfax Hospital, 2) Department of Vascular Radiology, Hospital Clinic i Provincial de Barcelona, and 3) Department of Interventional Neuroradiology, Rothschild Foundation. At each center, an expert clinician measured neck, depth, and width of the aneurysms in the first frame using standard measuring tools of angiography scanners. To know the image resolution, the same magnitudes were measured in the 3D-RA image to avoid errors due to geometric magnification. Table 2.2 provides detailed information about each sequence.

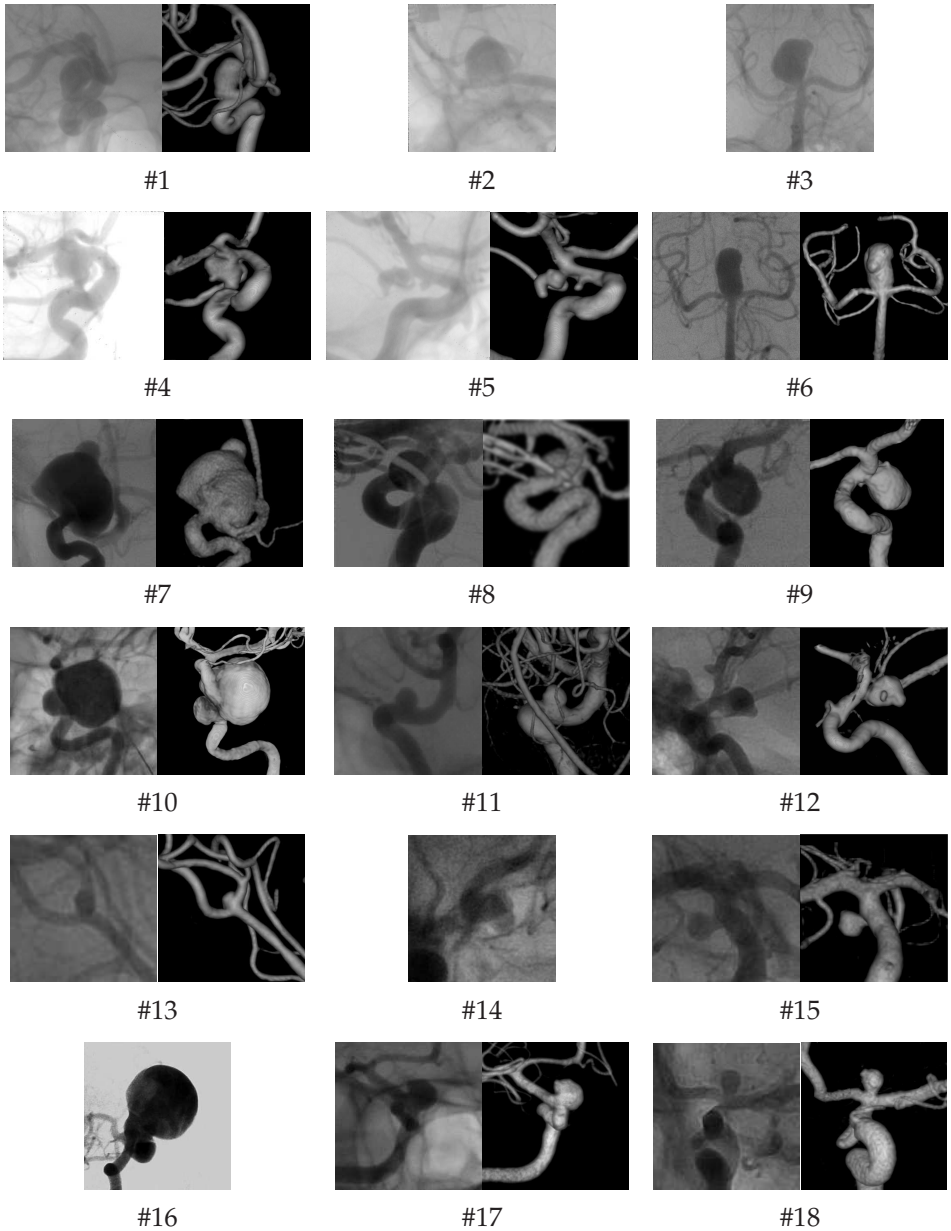

Figure 2.1: First frames of the DSA sequences used in this chapter. When available, the 3D-RA reconstruction is shown at right.

Table 2.2: Table summarizing relevant information about the sequences used in this chapter. M=Male, F=Female; FPS=Frames Per Second; ICA=Internal Carotid Artery, ACA=Anterior Cerebral Artery, BA=Basilar Artery, PCom=Posterior Communicating Artery, ACom=Anterior Communicating Artery, MCA=Middle Cerebral Artery; AR=Aspect Ratio; R=Ruptured, U=Unruptured; LAT=Lateral, TER=Terminal; Y=Yes, N=No, n/a = not available

Patient	**Gender**	**Age**	**Location**	**Size**	**AR**	**Status**	**Type**	**Injection**	**FR**	**Pulsation**	
										Dome	Bleb
#	*M/F*	*years*		*D* × *W* × *N (mm)*		R / U		*cc @ cc/s*	*FPS*	*Y / N*	
1	F	60	ICA	8.5 × 6.6 × 5.0	1.7	U	LAT	9 cc @ 3 cc/s	30	Y	n/a
2	M	50	ACA	7.2 × 7.8 × 7.8	0.9	U	LAT	9 cc @ 3 cc/s	30	Y	n/a
3	F	47	BA	11.3 × 9.7 × 3.8	3.0	R	TER	9 cc @ 3 cc/s	30	Y	Y
4	F	78	ACM	10.0 × 7.7 × 5.2	1.9	U	TER	9 cc @ 3 cc/s	10	N	N
5	F	56	ICA	4.0 × 4.0 × 2.0	2.0	R	LAT	9 cc @ 3 cc/s	30	N	N
6	F	47	BA	13.0 × 8.3 × 5.4	2.4	R	TER	24 cc @ 4 cc/s	7.5	N	N
7	F	46	ICA	19.8 × 18.9 × 3.5	5.7	R	LAT	24 cc @ 4 cc/s	3	Y	Y
8	M	28	ICA	9.0 × 8.8 × n/a	n/a	U	TER	24 cc @ 4 cc/s	2	Y	n/a
9	F	71	ICA	12.2 × 9.2 × 2.9	4.2	R	TER	24 cc @ 4 cc/s	7.5	Y	Y
10	F	41	ICA	17.1 × 19.8 × 9.9	1.7	U	LAT	15 cc @ 4 cc/s	30	Y	n/a
11	F	51	ICA	4.2 × 3.5 × 3.0	1.4	U	LAT	15 cc @ 4 cc/s	30	N	n/a
12	F	37	PCom	7.2 × 6.2 × 2.4	3.0	R	TER	15 cc @ 4 cc/s	60	Y	Y
13	F	37	MCA	2.0 × 2.9 × 2.8	0.7	U	TER	15 cc @ 4 cc/s	60	N	n/a
14	M	54	ACom	7.1 × × 3.3	2.2	R	LAT	15 cc @ 4 cc/s	30	Y	n/a
15	M	21	PCom	5.2 × 5.0 × 1.9	2.7	U	LAT	15 cc @ 4 cc/s	60	N	n/a
16	F	75	ICA	27.6 × 30.0 × 10.6	2.6	U	LAT	15 cc @ 4 cc/s	30	Y	n/a
17	F	44	ICA	8.2 × 10.2 × 6.6	1.2	U	LAT	15 cc @ 4 cc/s	30	N	n/a
18	M	46	ICA	4.2 × 4.0 × 2.5	1.7	U	TER	15 cc @ 4 cc/s	60	N	n/a

2.2.2 Wall motion estimation

The method applied for quantifying pulsation consists of three main steps described next (Figure 2.2).

Image registration

A DSA study consists of an image sequence $I(\mathbf{x}, t) = I_0(\mathbf{x}) \cdots I_{n-1}(\mathbf{x})$ of n phases that provides the voxel intensity at spatial position $\mathbf{x}$ and time t. To quantify temporal changes in the magnitude of interest, it is necessary to establish a dense point correspondence between images. This was performed by registering each frame $I_t(\mathbf{x})$ to the first one $I_0(\mathbf{x})$, yielding a set of transformations $\mathcal{T} = \{\mathbf{T}_i(\mathbf{x})\}_{i=1:n}$ that provide such correspondence. In a previous paper [28], we applied an Optical Flow (OF) method [29] for IR since this type of methods are preferred for recovering small magnitude changes [30]. However, OF methods are quite sensitive to variations in intensity due to quantum noise [31] and inhomogeneities in the contrast distribution, and non-smooth deformation fields are obtained. To obtain a smoother deformation field, in this chapter we have used Free-Form Deformations with B-Spline interpolation functions [32,33], and Mutual Information (MI) [34,35] as metric.

Point propagation and feature quantification

We have analyzed temporal changes in aneurysm depth $(d(t))$, aneurysm width $(w(t))$, and artery diameter $(a(t))$. These variables were measured by taking the euclidean distance between pair of points placed in the first frame, and propagated over time with the set of transformations $\mathcal{T}$. The points used to calculate the artery diameter were placed far away from the aneurysm to ensure the healthy state of the artery at the measurement point, and to avoid the influence of aneurysmal deformations. For the spacing between control points employed in this chapter, the spatial support of each B-Spline was in the order of the aneurysm size, and landmarks placed close to the aneurysm could be modified even in the absence of artery deformation. The points used to define the depth and with of the aneurysm were placed as shown in Figure 2.2.

Post-processing analysis

If changes in image intensity during the contrast filling were modeled linearly as $I_t(\mathbf{x}) = \alpha I_0(\mathbf{x}) + c$, with α and c constant values, the use of MI-based IR would account for these changes in intensity. This is because MI-based IR is robust to changes in intensity scale[1] as shown in Figure 2.3. However, intensity changes that

[1]Note that this does not mean invariance of MI, in fact $MI(A, \alpha A) = H(A) + log\|\alpha\|$ [36]

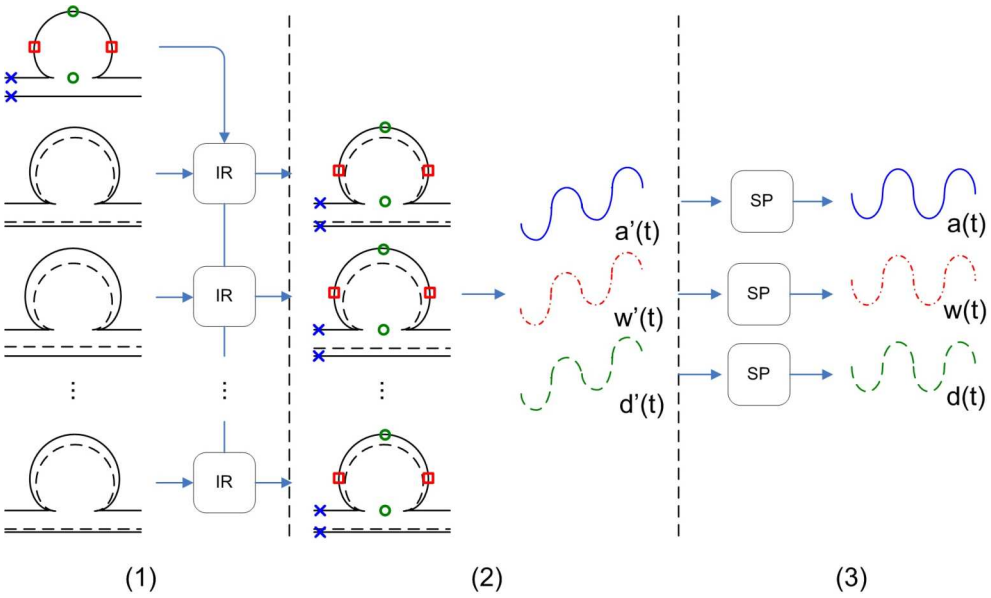

Figure 2.2: Wall motion estimation method. (1) image registration, (2) point propagation and feature quantification, and 3) post-processing. Crosses ($\times$), circles ($\circ$), and squares ($\square$), show the points used to measure changes in the artery ($a(t)$), depth ($d(t)$), and width ($w(t)$) of the aneurysm. IR = image registration; SP = signal processing.

occur during the contrast injection cannot be described accurately by this model, probably because of complex blood filling patterns. We have not found in the literature models of intensity changes due to contrast agent distribution to assess their influence on the IR, but a visual inspection of intensity profiles over time reveals that an exponential dependency of time is a reasonable approximation. Figure 2.4 shows that, even when the size of the aneurysm does not change, the optimizer will tries to match the intensity profiles by scaling the moving image. This overestimation of the aneurysmal size results in an increase in the mean value of the dilation curves over time. Fortunately, this change has low frequency with respect to pulsation, and can be removed by applying high-pass filters (Figure 2.5).

2.2.3 Differential pulsation index

As mentioned in the introduction, measuring pulsation is important to investigate the potential connection between regional differences in pulsation and rupture status. This is supported by the apparent concensus in the literature about a weakness of the vessel wall induced by a deficit in collagen and elastine [37–42]. What is more, collagenase and elastase activities seem to be increased in ruptured cerebral

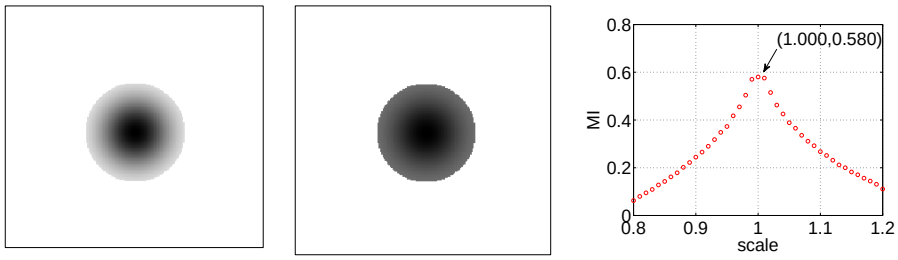

(a) (b) (c)

Figure 2.3: Robustness of MI to intensity scaling. In this example, the pixel intensity of the fixed image $I_f(\mathbf{x})$ (a) is half the intensity of moving image $I_m(\mathbf{x})$ (b) ($I_m(\mathbf{x})$ = 0.5*$I_f(\mathbf{x})$). (c) $MI(I_f, T_{is}(I_m))$ as a function of the scaling factor for an isotropic scaling transformation T_{is}. MI has a maximum at 1.

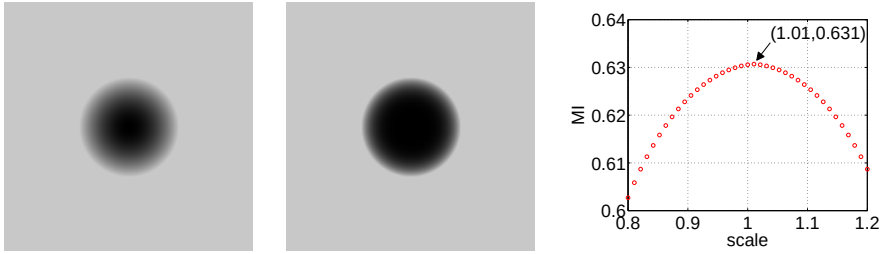

(a) (b) (c)

Figure 2.4: Overestimation of dilation when considering a non-linear relationship of intensities. In this example, the fixed image $I_f(\mathbf{x})$ (a) presents a quadratic intensity profile, whereas the moving Image $I_m(\mathbf{x})$ (b) presents a quartic profile. (c) $MI(I_f, T_{is}(I_m))$ as a function of the scaling factor for an isotropic scaling transformation T_{is}. MI has a maximum at a value higher than 1.

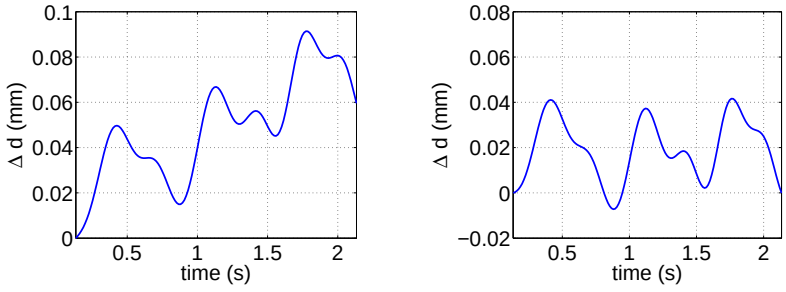

(a) (b)

Figure 2.5: Distension waveform before (a) and after (b) filtering.

aneurysms versus unruptured aneurysms [37]. Assuming that this deficit is higher in the aneurysm than in the parent artery, a difference in pulsation should be observed. To quantify the differential pulsation, we have defined the following index:

$$\mu = \frac{|max\left\{\hat{D}, \hat{W}\right\} - \hat{A}|}{\delta_{art}}$$

where $\hat{D}, \hat{W}, \hat{A}$ represent the peak-to-peak amplitude of $d(t), w(t), a(t)$ respectively, and δ_{art} is the artery diameter.

2.3 Results

Figure 2.6 shows $d(t)$, $w(t)$, and $a(t)$ for sequences exhibiting wall motion. To distinguish curves carrying information about wall motion from those containing just measurement noise, we have compared them to the model in Figure 2.9, and the presence/absence of wall motion was assessed based on the similarity. Since contrast injection times depend on the specific protocols of each clinical center, we show deformations for a single cardiac cycle for normalization purposes. As a consequence of the image acquisition issues mentioned Section 2.4, curves present distortions in some time intervals. This occurs in particular at the beginning and at the end of the contrast injection, where the largest changes in the image take place. Therefore, when information was available for several cardiac cycles, we selected the central part of the acquisition window to minimize distortions. Table 2.3 presents parameters extracted from $d(t)$, $w(t)$, and $a(t)$ for all sequences in Figure 2.6

Figure 2.7 (a) shows the distribution of the differential pulsation μ defined in Section 2.2.3 with respect to the rupture status. As shown in the Figure, the distribution of μ for ruptured aneurysms presents a higher mean value than the distribution for unruptured aneurysms ($\overline{\mu}_R = 6.1\%$ vs. $\overline{\mu}_U = 1.3\%$). As the standard deviations are not small, a statistical analysis was performed to assess the statistical significance of these differences. The result of a t-test showed that the null hypothesis of equal means is rejected for $p = 0.05$, i.e. the differences are significant at a level of 5 %.

We have also investigated variations in the pulsation magnitude according to type and size. Figure 2.7 (b) shows that terminal aneurysms present a higher pulsation amplitude than lateral aneurysms, but this difference is not significant according to a t-test. Figure 2.8 shows a linear correlation between μ, Δd_{max}, and the logarithm of the aneurysm volume $log(vol.)$. This is in agreement with the difference in mean volume between ruptured ($\overline{v}_R = 0.91cm^3$) and unruptured ($\overline{v}_U = 0.58cm^3$) aneurysms.

To study the consistency between *measured* and *observed* pulsation, the presence of visual pulsation was assessed by two observers in two sessions separated by one week. According to the Kappa statistics, the intra-observer accuracy is 0.76 for

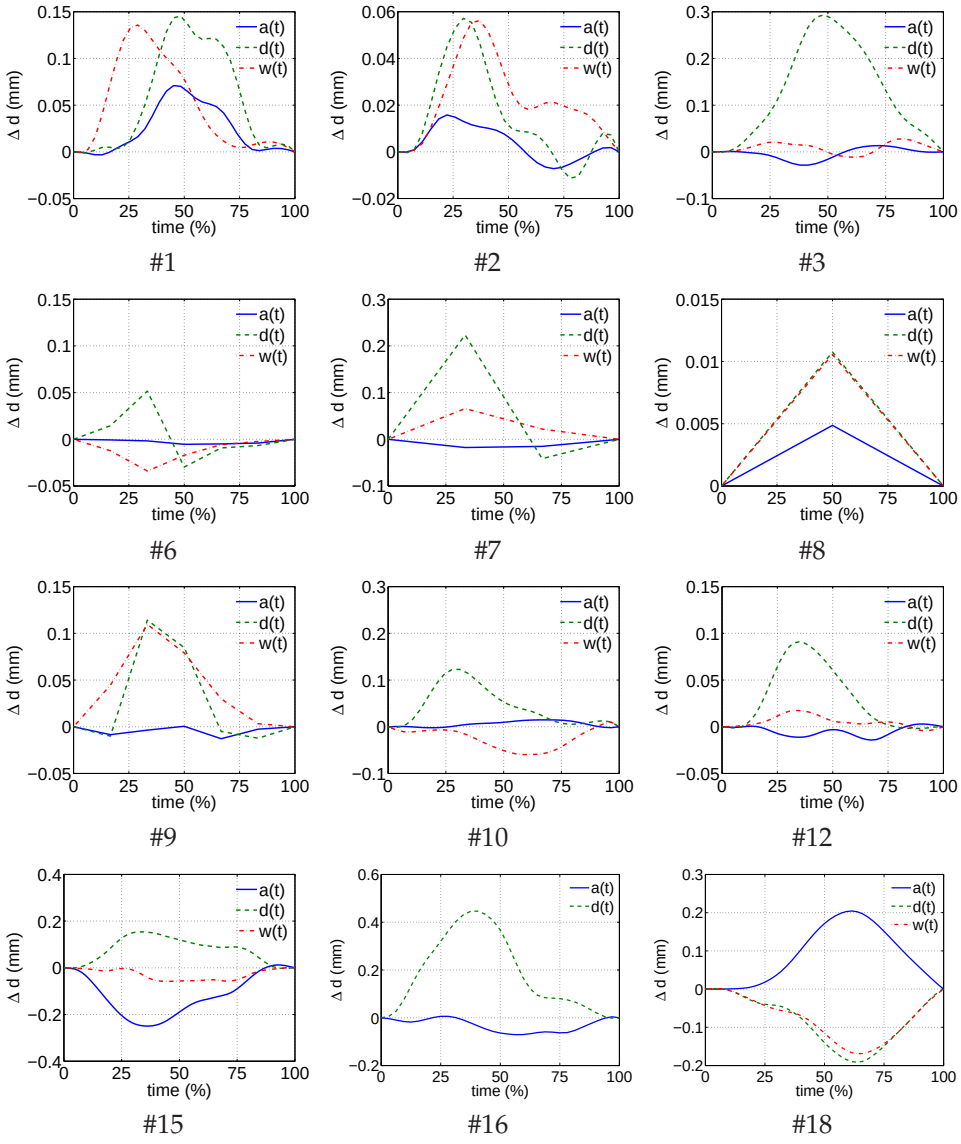

Figure 2.6: Distention curves $a(t)$, $d(t)$, and $w(t)$ over the cardiac cycle for sequences showing wall motion. Time is expressed as percent of the cardiac cycle. $w(t)$ is omitted for sequence #16, since it could not be estimated because of defects in contrast filling.

Table 2.3: Parameters extracted from curves $a(t)$, $d(t)$, and $w(t)$ for sequences showing wall motion. R=Ruptured, U=Unruptured; μ = differential pulsation; $\hat{D}$, $\hat{W}$, $\hat{A}$ = peak-to-peak amplitude of $d(t), w(t), a(t)$ respectively; ϕ_{da}, ϕ_{dw}, ϕ_{wa} = phase difference $d(t)$-$a(t)$, $d(t)$-$w(t)$, and $w(t)$-$a(t)$, expressed as percent of the cardiac cycle.

Patient	**Status**	μ	$\hat{\mathbf{D}}$	$\hat{\mathbf{W}}$	$\hat{\mathbf{A}}$	$\phi_{\mathbf{da}}$	$\phi_{\mathbf{wa}}$	$\phi_{\mathbf{dw}}$
#	R/U	%	*mm*	*mm*	*mm*	%	%	%
1	U	2.26	0.15	0.14	0.074	0	-16	20
2	U	2.40	0.07	0.06	0.023	7	13	-7
3	R	15.97	0.29	0.04	0.042	-25	6	-34
6	R	5.16	0.08	0.03	0.005	33	0	33
7	R	8.02	0.26	0.07	0.018	31	31	0
8	U	0.17	0.01	0.01	0.005	0	0	0
9	R	3.53	0.14	0.11	0.013	-16	-16	0
10	U	2.34	0.12	0.07	0.017	-47	13	28
12	R	3.71	0.09	0.02	0.017	46	46	0
15	U	2.84	0.16	0.06	0.262	40	9	31
16[a]	U	8.25	0.45	-	0.077	39	-	-
18	U	0.52	0.19	0.17	0.204	38	38	0

[a] It was not possible to estimate $w(t)$ for patient #16 because of defects in the contrast filling. Therefore, measurements involving this curve are omitted in this table.

both observers (substantial agreement according to Landis and Koch's paper [43]) and the interobserver accuracy of 0.41 (moderate agreement). The reason why a perfect agreement was not achieved is most likely due to the fact that the wall motion amplitudes are quite small, and in many cases close to the image resolution. Figure 2.7 (c) shows the distribution of pulsation amplitudes according to presence of visual motion as assessed by the observers mentioned in Section 2.4. As expected, aneurysms classified as "pulsating" presented a higher pulsation amplitude in mean than "non-pulsating" aneurysms.

2.4 Discussion

In previous work [24,28], we described temporal changes in aneurysms by measuring the displacements of points on the vessel wall. This approach requires a previous segmentation to assess the sign of the displacement, i.e. whether points move inwards or outwards the aneurysm at the reference point. Besides adding an extra step in the pipeline, (according to our experience) the segmentation of DSA images is extremely difficult since this modality does not provide a proper definition of the vessel lumen. As the wall displacement is in the order of the image resolution, even small segmentation errors can make the method fail to recover pulsation. In this chapter we have circumvented this drawback by measuring the euclidean distance between pairs of points, which avoids the need for a previous image segmentation.

In some cases, we have founded a rigid motion associated to the global pulsa-

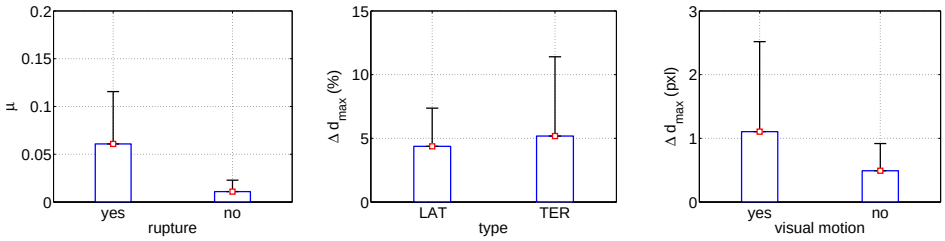

(a) (b) (c)

Figure 2.7: Pulsation of aneurysms according to (a) rupture status, (b) type, and (c) visual motion. Note that the y axes units are different for all figures: the μ index is plotted in (a), the maximal deformation (relative to the artery diameter) in (b), and image pixels in (c). Bars show the standard deviations of distributions. The μ value for sequence #16 was considered as an outlier, and excluded in (a).

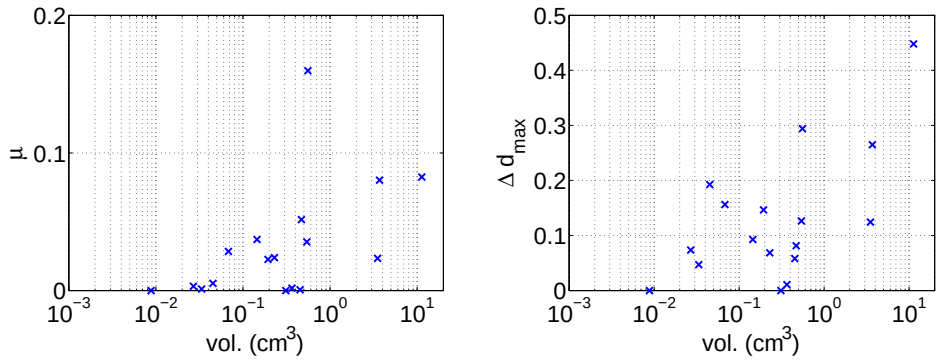

(a) (b)

Figure 2.8: Variations in the magnitude of pulsation with the size of the aneurysm. (a) μ vs volume, (b) Maximum displacement vs. volume. The size of the aneurysms was measured as the volume of the prolate ellipsoid with minor radii $a = b = with$ and major radius $c = depth$. The volume is represented by using a logarithmic scale, since this is more appropriate for the distribution of volumes in our database.

tion of the intracranial vasculature that should be corrected before estimating the deformation. Fortunately, this motion was very small [2] and was captured by the non-rigid transformation. Therefore, the rigid motion was corrected automatically without adding an extra step.

It is important to make some remarks with respect to image acquisition. The Nyquist theorem establishes that the minimum sampling frequency f_s^{min} that allows recovering the aneurysmal pulsation is twice the signal bandwidth (BW) [44]. To our knowledge, there are no measurements of temporal changes of intracranial aneurysms in the literature to estimate BW, and we have used simulated pressure data [45] for the Common Carotid Artery (CCA) (Figure 2.9) to estimate it. Two important assumptions are made here. 1) The wall displacement and pressure waveforms are the same (except for a scale factor): this is true if linear elasticity of the vessel wall is assumed, but both waveforms could differ slightly if a viscoelastic model and large mass-effects are considered. 2) The pressure waveform does not change from the CCA to the location of the aneurysm. Figure 2.9 shows that the most important frequency components are comprised in the range 0-4 Hz, and therefore we can establish a f_s^{min}=8 Hz as the minimum f_s to recover aneurysmal pulsation. Even when this estimation is based on simulated data, it allowed obtaining curves resembling the typical arterial pressure waveform [46] (see for example sequences #1, #2, #9, #10, #12, #15 in Figure 2.6). This similarity supports the assumption that the recovered deformations effectively quantify the wall displacements of the vessel, and do not come from sources of variations like image noise, intensity changes, or movement artifacts. As shown in Table 2.2, some sequences were acquired at lower sampling frequency than this inferior limit. Sometimes, low f_s values are preferred to obtain a higher image quality, and values as low as $2Hz$ can be found. Figure 2.6 shows the result when f_s does not meet the requirements imposed by the Nyquist's theorem (sequences #7 and #8). As the sampling frequency for these sequences ($f_s = 3Hz$ and $f_s = 2Hz$, respectively), distension waveforms cannot be completely recovered.

The dependency of the method on the contrast injection parameters (e.g. injection rate, total volume) is critical, since they must ensure a complete and homogeneous filling of the aneurysm for at least one cardiac cycle. It is very difficult to select a fixed set of parameters to satisfy these requirements in all aneurysms, since the filling depends strongly on factors like size, shape, and type of the aneurysm. The influence of type is well illustrated by terminal aneurysms of the basilar artery (Figure 2.1, patients #3 and #6). In these cases, the aneurysm receives the blood jet directly from the parent artery which produces a strong washout of contrast medium. A large size may be also problematic, since the filling is slower and sometimes the injected contrast is not sufficient to fill the aneurysm (Figure 2.1, patients #7 and #10). These problems are related to the upper limits imposed by the cel-

[2]Note that the aneurysmal pulsation is also very small, and therefore any rigid motion must be completely compensated to have an accurate estimation

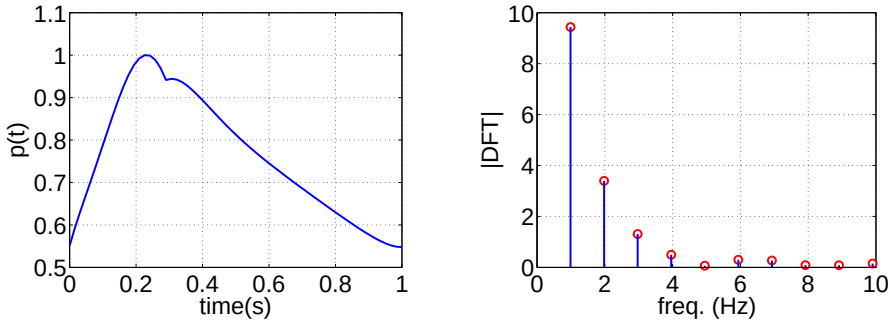

Figure 2.9: (a) Simulated pressure at the Common Carotid Artery (CCA) [45] (b) Magnitude of its DFT (spacing of samples in the Fourier domain $1/T = 1$, where T is the period of the signal). The continuous component ($f = 0$) was removed from the DFT for better visualization of high frequency components. Frequencies higher than 20 Hz were also omitted because of their small amplitude.

lular effects of contrast media [47], and their connection to nephropathies [48]. If there were no such limits, the amount of contrast could be made big enough to compensate the effects of size and type.

Figure 2.6 shows that in some cases the recovered curves are out-of-phase. This cannot be attributed to the filters used for postprocessing, since the phase difference persists when filters are not applied (see patient # 6 for example). A possible explanation to this phenomenon is the asymmetric deformation of the aneurysm owing to specific blood flow patterns. Consider for example the same patient (# 6). As can be seen from Figure 2.1 this is a basilar aneurysm that receives a direct impingement of the blood flow coming from the basilar artery. As the direction of the jet is parallel to the longitudinal axis of the aneurysm, it increases its depth at the expense of a decrease in width as shown in Figure 2.10. This explanation predicts a phase difference of 180 degrees, which in fact was the difference of phase found in the example. A similar analysis of other aneurysmal configurations should be performed to understand the regional differences in pulsation, and a CFD analysis could be necessary for complex cases. Another explanation for these phase differences is the pulsation of extravascular structures (like the brain), which could pulsate synchronously with the artery and modify influence the expected deformation pattern of the aneurysm.

Lateral and terminal aneurysms showed slight non significant differences in wall motion. However, terminal aneurysms receive a direct impact of the blood jet coming from the parent artery which should produce a larger deformations. A

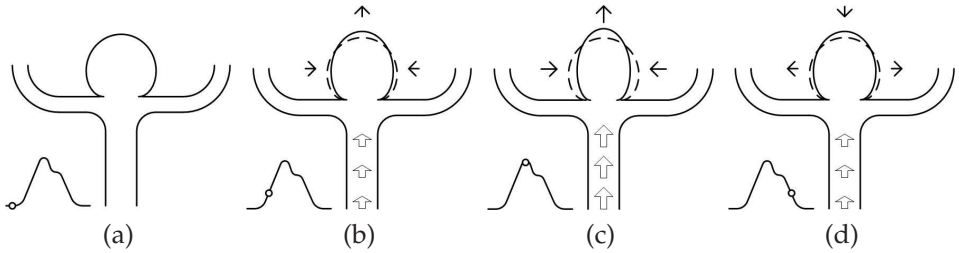

Figure 2.10: Relationship between blood flow and wall motion for a basilar aneurysm. Figures (a)-(d) show the deformation of the aneurysm for four temporal points of the cardiac cycle (shown as an empty circle at bottom left of each figure). Empty arrows in the parent artery represent the blood blow (their length is proportional to the flow magnitude). The small black arrows represent the wall displacement with respect to the previous time instant.

possible explanation are the differences in location of the considered aneurysms, which should be normalized to ensure similar haemodynamic conditions. Larger aneurysms exhibited a higher differential pulsation index, and wall motion amplitude. However, other papers have reported no relationship between aneurysm size and volume increases [4].

The method presented in this chapter allows obtaining deformations in the image plane. This information could be complemented by a second acquisition in an orthogonal projection. However, according to our experience, the neighboring vessels make extremely difficult to obtain two orthogonal views showing the aneurysm without an overlapping with other vessels. The presence of neighboring can also perturb the recovered displacement fields: at the beginning of the contrast filling, the aneurysm appears isolated from the rest of the vasculature and its boundary is well defined. As the contrast injection progresses, distal vessels start appearing in the image (Figure 2.11) and a local misregistration occurs due to the lack of correspondence [49].

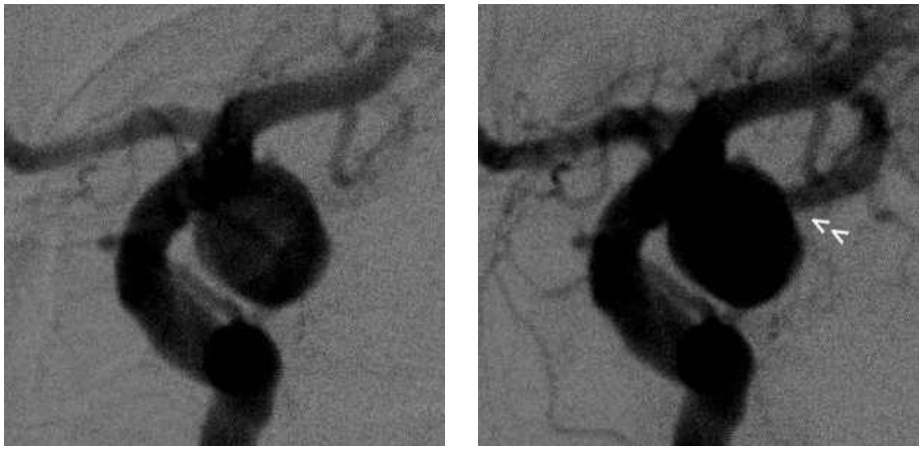

(a) (b)

Figure 2.11: Influence of neighboring vessels: at the beginning of the contrast filling the boundary of the aneurysm is free (a). As the contrast injection progresses, distal vessels start appearing in the image causing local misregistration occurs due to lack of point correspondence.

2.5 Conclusions

In this chapter we have combined non-rigid registration methods with signal processing techniques to quantify wall motion of intracranial aneurysms from dynamic DSA sequences. To our knowledge, this is the first time that pulsation of is quantified over the cardiac cycle. We applied the presented methodology to a series of intracranial aneurysms and found a higher index of differential pulsation for ruptured aneurysms. These measurements and observations may help us better stratify aneurysm rupture risk and understand the wall motion effects on aneurysm haemodynamics and their evolution.

CHAPTER 3

Cardiac motion estimation by using complex wavelets

Abstract - *Tagged Magnetic Resonance Imaging (T-MRI) is currently considered the reference modality for myocardial motion estimation and strain analysis. Non-rigid registration based on Mutual Information (MI) has been proposed as an automatic method for recovering cardiac displacement fields. However, the use of MI of voxel intensity ignores the spatial information provided by the tags, whose inclusion in the similarity metric could increase the accuracy and robustness. In this chapter, we have used the alpha-MI (MI_α) of features vectors derived from the Complex Wavelet Transform (CWT), which add high frequency information along six equally spaced directions in the frequency domain. To cope with the problem of estimating the MI of high-dimensional features, we have used estimators based on k-Nearest Neighbors Graphs (kNNG), which allow a direct estimation of the metric without estimating probability density functions. Experiments performed on a series of 2D T-MRI sequences showed an increase in accuracy with respect to metrics based on image intensity, but the computational cost of the investigated technique could limit its extension to deal with real 4D sequences.*

Adapted from E. Oubel, A. O. Hero, and A. F. Frangi Complex Wavelets for Registration of tagged MRI sequences. In J. Kovačević and E. Meijering, editors, *Third IEEE International Symposium on Biomedical Imaging: From Nano to Macro (ISBI'06)*, Arlington, VA, USA, April 2006.

3.1 Introduction

Tagged magnetic resonance imaging (T-MRI) is a well established technique for obtaining regional information on the left ventricle (LV) deformation [2], and therefore it is potentially valuable for the diagnosis of cardiovascular diseases [11]. Basically, this technique consists in perturbing the magnetization of the myocardium in a specific spatial pattern at end-of-diastole (ED). These perturbations appear as dark straight stripes (tags) when imaged immediately after application of the magnetic field. Since the myocardial tissue retains its magnetization properties, tags undergo the same deformation as the heart. This allows tracking material points along the cardiac cycle.

Several methods have been proposed to retrieve LV displacement fields: optical flow [50–53], Harmonic Phase (HARP) MRI [54–56], tag detection and tracking [57–60], and image registration [12,13]. Non-rigid registration based on Mutual Information (MI) has been proposed as an automatic method for recovering cardiac displacement fields. However, the use of MI of voxel intensity ignores the spatial information provided by the tags [61], whose inclusion in the similarity metric could increase the method accuracy and robustness according to results reported in the literature [61–63].

In this chapter, we have investigated the use of MI of feature vectors obtained from the Complex Wavelet Transform (CWT). In a previous paper [64], we have shown that cardiac motion estimation was feasible by using a similar framework based on the Discrete Wavelet Transform (DWT). The CWT is an attractive image representation since it is shift invariant, and it provides better discrimination of directionality with respect to the DWT [65, 66]. The CWT has already been applied to motion estimation since its phase depends almost linearly from displacements in the image [67]. As the features derived from the CWT are in a high dimensional space, we used an MI_α estimator based on k-Nearest Neighbors Graphs (kNNG) [68]. This estimator permits estimating the MI_α without computing a probability density function (pdf) of the feature vectors.

3.2 Method

3.2.1 Dataset

We have used four 2D T-MRI sequences in short-axis acquired in breath-hold by using a General Electric Signa CV/i, 1.5 T scanner (General Electric, Milwaukee, USA). The values of acquisition parameters were: slice thickness = 8mm, in-plane resolution = 1.56mm $\times$ 1.56mm, TR=7.99ms, TE=4.43ms, flip angle = 20 degrees, and FOV=40cm$\times$40cm. 16 phases per cardiac cycle were acquired. T-MRI images with a grid pattern of 8mm (tag spacing) were acquired by applying a Spatial Mod-

ulation of Magnetization (SPAMM) sequence. The method was applied only to images in systole, because of the tag fading effect of SPAMM sequences.

3.2.2 Motion estimation

Let $I(\mathbf{x}, t)$ be a 2D T-MRI sequence of n_p phases, which provides the voxel intensity at spatial position $\mathbf{x}$ and time t. Cardiac displacement fields can be represented by a set of $n_p - 1$ transformations $\mathcal{T}(\mathbf{x}) = \{T_i(\mathbf{x})\}_{i=1:n_p-1}$ [69]. The estimation of $\mathcal{T}(\mathbf{x})$ starts registering $I(\mathbf{x}, 1)$ to $I(\mathbf{x}, 0)$, which provides $T_1(\mathbf{x})$. Then, $I(\mathbf{x}, 2)$ is registered to $I_{SA}(\mathbf{x}, 0)$ using $T_1(\mathbf{x})$ as initialization, and $T_2(\mathbf{x})$ is obtained. This process is repeated for the remaining frames. The transformation model employed in [69] are Free-Form Deformations with B-Splines as interpolation functions. First proposed by Lee *et al.* [32,32] for computer graphics applications, this model was then applied by Rueckert *et al.* [19] for detection of cancerous lesions in contrast enhanced MR breast images.

3.2.3 Complex wavelet transform

The DWT of a discrete signal $x(n)$ is obtained by applying a low pass filter with impulse response $g(n)$, and a high pass filter with impulse response $h(n)$. The output of $g(n)$ is called the *approximation coefficients*, and the output of $h(n)$ are the *detail coefficients*. To remove redundancy in the signal representation, the filter outputs are subsampled by a factor 2 (Figure 3.1). The DWT of an image is obtained by applying the filters separately to rows and columns. This decomposes the image into four images called LL, HL, LH, and HH according to the order of application of filters.

The DWT presents two main drawbacks:

1. *Lack of shift invariance*: this means that the energy of the DWT coefficients changes with image shifts.

2. *Poor directional selectivity*: The LH and HL filtering provides high horizontal and vertical frequencies respectively, and there is no ambiguity in the information. However, the HH filtering provides information on diagonal features in both directions (it does not differentiate between an edge at 45^o and 135^o degrees, for example).

To overcome these problems, Kingsbury [65] introduced the CWT. This transform can be represented by the same block diagram in Figure 3.1, but in this case the filters have complex coefficients and generate a complex output. Despite being implemented separately, the complex filters provide true directional selectivity as they separate all parts of the frequency space. For 2D images the CWT produces an approximation image H, and six bandpass subimages $G_{k=0:5}$ oriented at $\pm 15^o$,

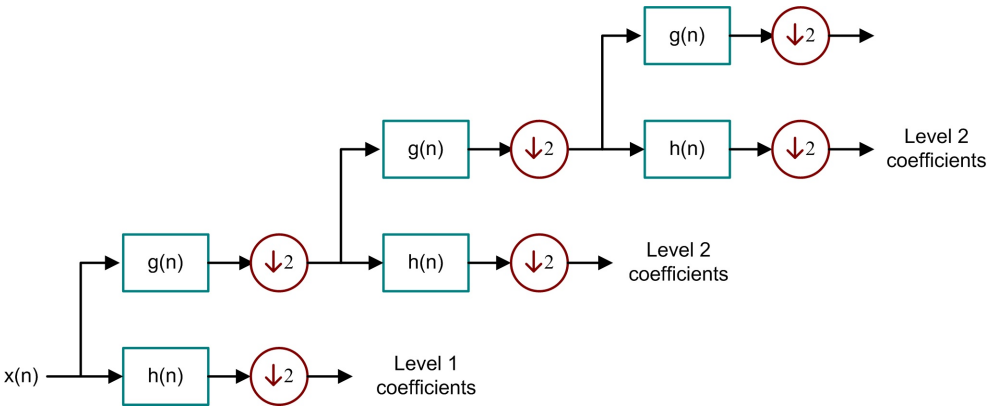

Figure 3.1: Filter bank to implement three levels of the unidimensional DWT. $x(n)$: input signal; $h(n)$: low pass filter; $g(n)$: high pass filter. A subsampling by a factor 2 is applied to the filter output.

$\pm 45^o$, $\pm 75^o$. A comprehensive explanation and more details on CWT can be found in the paper by Kingsbury [66]. Figure 3.2 shows an example of CWT.

3.2.4 MI_α estimation using kNNG

Given a set $\mathcal{Z} = \{\mathbf{z}_1, \ldots, \mathbf{z}_n\}$ of n vectors in $\mathbb{R}^d$, a kNNG is formed by all points $\mathbf{z}_{i=1:n}$ and the edges with their k nearest points $\mathcal{N}_{k,i}(\mathcal{Z}) = \{\hat{\mathbf{z}_{i1}}, \ldots, \hat{\mathbf{z}_{ik}}\}$. Figure 3.3 shows examples of kNNGs for two different point distributions.

Let $I_f(\mathbf{x})$ and $I_m(\mathbf{x})$ be the images to register, and $\mathcal{Z}_f = \{\mathbf{z}_{f1}, \ldots, \mathbf{z}_{fn}\}$, $\mathcal{Z}_m = \{\mathbf{z}_{m1}, \ldots, \mathbf{z}_{mn}\}$ n realizations of a random vector $\mathbf{Z}$ (the matching feature) in each image. The MI_α of the feature $\mathbf{Z}$ can be estimated as [70]:

$$\widehat{MI}_\alpha = \frac{1}{\alpha - 1} \log \frac{1}{n^\alpha} \sum_{i=1}^{n} \sum_{p=1}^{k} \left(\frac{e_{\mathcal{Z}_{fm},p}(\mathbf{z}_{fmi})}{\sqrt{e_{\mathcal{Z}_f,p}(\mathbf{z}_{fi}) e_{\mathcal{Z}_m,p}(\mathbf{z}_{mi})}} \right)^{2\gamma}, \tag{3.1}$$

where $e_{\mathcal{Z},p}(\mathbf{z}_i)$ is the distance from the point $\mathbf{z}_i$ to its p-nearest neighbor $\mathbf{z}_{j \neq i}$ in $\mathcal{Z}$, and $\mathcal{Z}_{fm} = \{\mathbf{z}_{fm1}, \ldots, \mathbf{z}_{fmn}\}$ is the set of joint features $\mathbf{z}_{fm} = [\mathbf{z}_f \mathbf{z}_m]$ in $\mathbb{R}^{2d}$, and $\gamma = d(1 - \alpha)$.

3.2.5 Feature vectors

The method proceeds by an initial registration by using the CWT approximation coefficients, followed by a second registration using the feature vectors defined below. If all the CWT coefficients were joined in the same feature vector, the registration

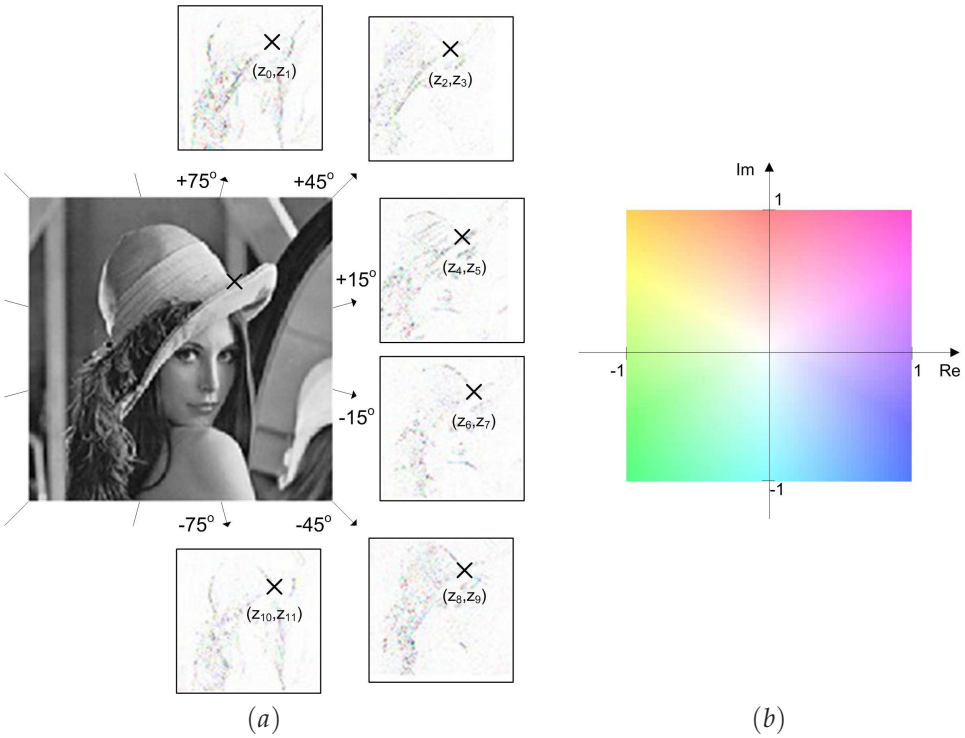

Figure 3.2: Definition of the feature vector **Z**. (a) First level of the CWT for Lena, whose subimages provide details of the original image oriented at $\pm 15°$, $\pm 45°$, and $\pm 75°$. Crosses show spatially corresponding coefficients, which are grouped to form the vector **Z**. As the coefficients are complex, each subimage provides two components to **Z**. (b) Colormap used for representing complex values.

process could be dominated by approximation coefficients, since their magnitude is much higher than the detail coefficients. The second step is where high frequency information in tags is introduced into the registration process.

The feature vector $\mathbf{Z} = [Z_1, ..., Z_d]$ was formed by the detail coefficients of the first level of CWT decomposition (Figure 3.2). Since there are six high-frequency images of complex coefficients at each level, **Z** is a vector in $\mathbb{R}^{12}$ whose components are defined as:

$$Z_i = \begin{cases} Re(G_k(\mathbf{x})), & \text{if } i \text{ is even} \\ Im(G_k(\mathbf{x})), & \text{if } i \text{ is odd} \end{cases} \tag{3.2}$$

where $k = \lfloor i \rfloor$, and G_k is the k^{th} image of details .

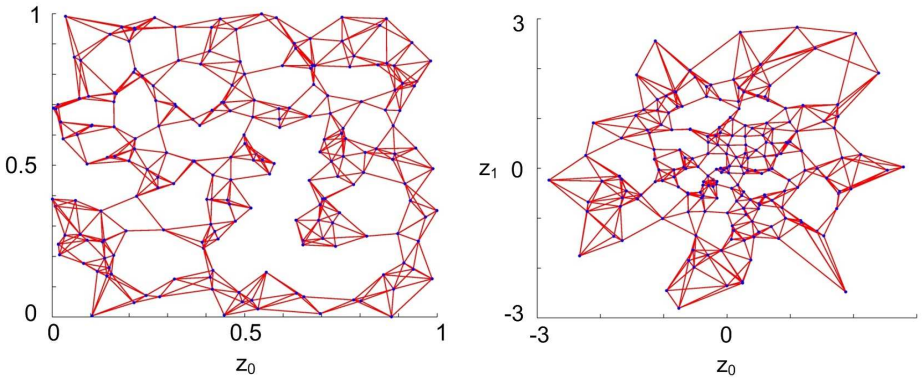

Figure 3.3: Examples of *k*NNGs (*k*=5) for a set of 200 points in the plane with (a) uniform and (b) Gaussian distributions.

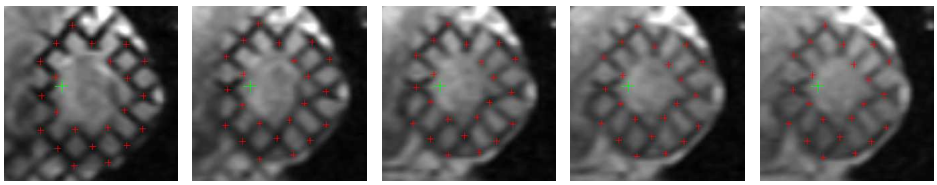

Figure 3.4: Gold standard points $\mathcal{L}_i$ for each frame i from ED to ES of sequence #1. Time is expressed relative to the systole duration.

3.2.6 Evaluation

Tag intersection points (18 in average) were marked manually in each frame by two observers in two independent sessions. The intraobserver errors were $0.01 \pm 0.35mm$ and $0.06 \pm 0.31mm$, and the interobserver error was $0.03 \pm 0.29mm$. A set of gold standard landmarks for the image i ($\mathcal{L}_i$) was obtained by averaging the measurements made by both observers. The set of transformations $\mathcal{T}$ was then used to propagate $\mathcal{L}_0$ to each phase, producing estimations $\widehat{\mathcal{L}}_i$ of $\mathcal{L}_i$. As the mean square error (MSE) between $\widehat{\mathcal{L}}_i$ and $\mathcal{L}_i$ increases from end-of-diastole (ED) to end-of-systole (ES), we computed the average over all phases. Figure 3.4 shows the gold standard landmarks for each frame in sequence #1.

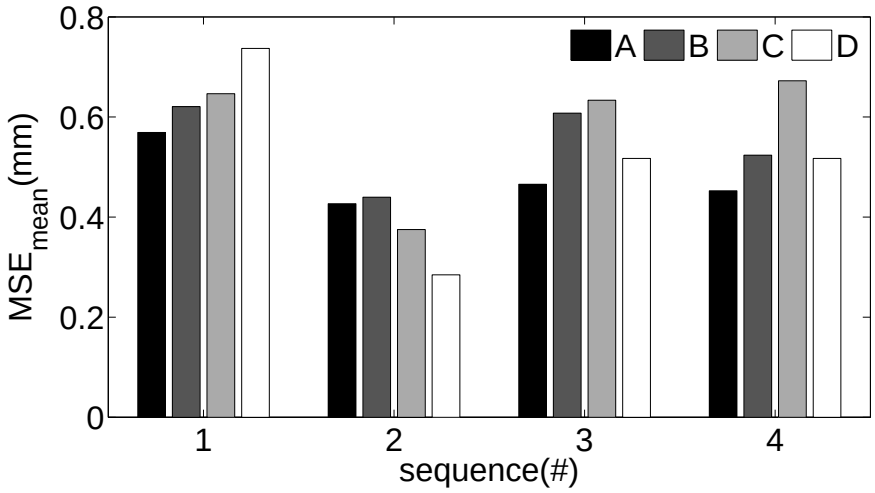

Figure 3.5: Mean MSE over systole for all sequences and metrics used in this chapter. A-MI_α of CWT-based features; B-MI_α of DWT-based features; C-MI_α of pixel intensity; D-Shannon MI of pixel intensity estimated by histograms.

3.3 Results and discussion

Four methods were applied to the dataset described in Section 3.2.1. They were identical except for the metric:

A- MI_α of CWT-based features (the method described in Section 3.2).

B- MI_α of DWT-based features (Haar wavelets [71] were used) [64]

C- MI_α of pixel intensity (an unidimensional feature).

D- Shannon MI of pixel intensity estimated by histograms.

Figure 3.5 shows that the method A provided the lowest errors for sequences #1, #3, and #4. An interesting result is the order of performance of methods A-C, which suggests an increase in accuracy with the amount of high frequency information employed. The use of the same MI_α estimator in these three cases, allowed to study the isolated effect of the feature type on the whole method. The effect of the estimator type is well illustrated also in Figure 3.5: when pixel intensity is used as feature, the use of histograms provides lower errors than kNNG. This could be a consequence of the higher smoothness and wider region of capture of histograms with respect to kNNGs [72].

The results for sequence #2 are also interesting. For this sequence, intensity-based methods provided lower errors than wavelet-based methods. An examination

of sequence #2 revealed the presence of high-frequency coil artifacts which could have misguided the registration step based on details coefficients.

One drawback of the presented method is its high computational cost. When using gradient-based optimizers, and the gradient is estimated by finite differences, it is necessary to resample the moving image and calculate its CWT twice for each degree of freedom of the transformation. This becomes critical for FFDs because of their high number of parameters: even a coarse bidimensional grid of 8×8 control points would require the computation of 256 CWTs to estimate the gradient. Another factor that makes the method computationally expensive is the use of kNNGs to estimate MI_α. This requires the construction of a kd-tree ($\mathcal{O}(nlog(n))$) and k queries for each feature.

One possible way of improving the obtained results is the use of CWT phase information, since it depends almost linearly on displacements in the image [67]. Other ideas are the selection of coefficients based on noise level estimation, and to take advantage of the multiresolution nature of wavelet transform to implement an intrinsically multiresolution method. The use of gradient-based optimizers may be not the best choice, since the smoothness of the MI_α cannot be guaranteed in our context. Experiments with other optimizers like the Nelder-Mead method should be carried out.

3.4 Conclusions

Spatial information present in tags has been introduced into a registration-based method for cardiac motion estimation. This has been accomplished by using feature vectors formed with CWT coefficients. CWT offers shift invariance, good directional selectivity, and intrinsically multiresolution image representation, properties that make the transform quite suitable for registration purposes. This has been demonstrated by obtaining lower errors with respect to the use of Haar wavelet transform and pixel intensity to form feature vectors. However, a drawback of the presented methodology is its high computational cost, which could limit its practical application (specially in 3D datasets).

CHAPTER 4

Cardiac motion estimation by using joint image registration

Abstract - *Tagged Magnetic Resonance Imaging (T-MRI) is one of the reference modalities for obtaining regional information on myocardial deformation, and it is considered a valuable tool for the diagnosis of cardiovascular diseases. Image registration techniques have been proposed as an automatic method for recovering cardiac displacement fields. Initially performed as a set of pairwise registrations, these techniques have evolved to the use of 3D+t deformation models, requiring metrics of joint image alignment. However, only linear combinations of cost functions defined with respect to the first frame have been used. In this chapter, we have applied k- Nearest Neighbors Graphs (kNNG) estimators of the α-entropy (H_α) to measure the joint similarity between frames. To cope with the high computational cost of these estimators, an analytical expression for computing the metric gradient was obtained. Experiments performed on six subjects showed a significantly higher accuracy ($p < 0.05$) with respect to a pairwise approach in terms of mean positional error and variance with respect to manually placed landmarks. The developed method was used to compare strains in patients with myocardial infarction with respect to healthy subjects, showing a consistency between strain, infarction location, and coronary occlusion.*

Adapted E. Oubel, M. De Craene, A. O. Hero, M. Huguet, G. Avegliano, B. H. Bijnens and A F. Frangi. Cardiac Motion Estimation by Joint Alignment of Tagged MRI Sequences. *Under review.*

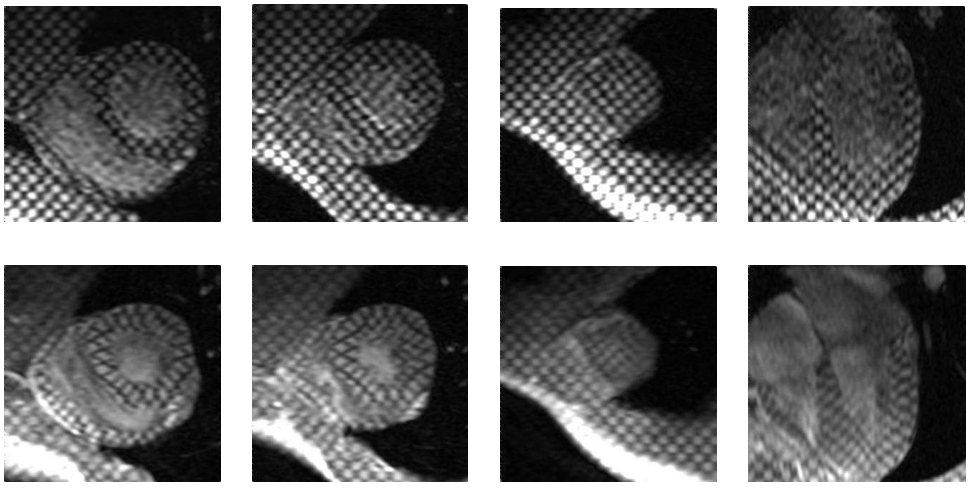

Figure 4.1: Example of the T-MRI images used in this chapter. From left to right: basal, medial, apical, and longitudinal planes of the LV are shown. Top row corresponds to End-of-Diastole (ED) and bottom row to End-of-Systole (ED).

4.1 Introduction

Tagged Magnetic Resonance Imaging (T-MRI) is currently the reference modality in clinical practice to obtain regional information on left ventricular (LV) myocardial deformation. Since its introduction by Zerhouni *et al.* [3] for cardiac function assessment, this technique has rapidly evolved due to advances in image acquisition, image processing, and clinical applications. The continuous efforts of researchers to obtain a completely automatic and reliable method for recovering cardiac motion and deformation, have generated interest in this modality. Recently, Axel *et al.* have presented a review of technical and clinical advances in this area [11,73]. Figure 4.1 shows an example of the images used in this chapter.

Non-rigid registration has been applied for recovering cardiac displacement fields from T-MRI sequences. Radeva *et al.* [74] have tracked the LV motion by minimizing the energy of a B-Solid. Other authors [12,75], building upon the initial approach of Rueckert *et al.* [19], applied pairwise registrations between the current phase and the first [12] (previous [75]) phase in the sequence. All of them proposed to maximize Mutual Information (MI) as similarity metric between both images [34,35]. Subsequently, 3D + t transformation models were applied for modeling cardiac motion [76,77], aiming at exploiting the temporal correlation between

phases. The use of these models immediately raised the issue of defining a metric of the joint alignment of all phases in order to optimize simultaneously all transformation parameters. This problem was first addressed by a linear combination of pairwise metrics between each phase and the first one [76, 77]. However, this approach still measures the image similarity with respect to the first phase and fails to exploit inter-phase correlation. Shen *et al.* [78] applied the HAMMER [79] algorithm for simultaneous registration of all phases in a cine MRI (C-MRI) sequence by matching attribute vectors at corresponding points. In order to exploit temporal correlation, they included an energy term comparing attribute vectors within a 4D neighborhood in the total energy functional.

Metrics based on information theory have been successfully applied for registration of T-MRI images [12, 75], owing to their capability to account for non-linear intensity changes introduced by the tag fading effect. Therefore, it is worthwhile to study extensions of such metrics for measuring the joint alignment of an image sequence. The main challenge is the accurate estimation of the probability density function (PDF) from a set of samples in a high-dimensional space. Neemuchwala *et al.* [72] have recently presented estimators of α- Mutual Information MI_α based on kNNG when high dimensional features are employed, and the use of histograms is not possible due to the curse of dimensionality [80]. Ma *et al.* [81] have applied these estimators for computing deformations in a synthetic sequence of tumor images, and introduced joint similarity extensions of MI_α. More recently, Leonenko *et al.* [82] have presented a class of estimators of H_α based on the k-th nearest-neighbor distances computed from a sample of N i.i.d. vectors with distribution f.

In this chapter, we have extended kNNG estimators of H_α to quantify the joint alignment of multiview sequences, and applied it to T-MRI sequences to recover cardiac displacement fields. For quantitative assessment of our method, a comparison was run against the method proposed by Chandrashekara *et al*. [12] for a population of 6 healthy subjects. Results show a significant decrease in positional error with respect to manually placed landmarks. For assessing the performances of our method in quantifying heart failure, we illustrate for 2 patients with myocardial infarction consistency between strain maps as recovered by our algorithm and DE-MRI and catheterization information. In the context of this chapter, *joint alignment* (JA) refers to the simultaneous alignment of all phases as proposed in [81], whereas *pairwise alignment* (PA)*joint alignment* (JA) refers to the technique proposed in [76]. Sometimes the term *sequence alignment* is also used in the sense of JA, and confusion with methods for intersubject sequence alignment like the one presented by Perperidis *et al.* [1] must be avoided.

4.2 Method

4.2.1 Dataset

The database used for the experiments consisted of 6 healthy subjects (3 females and 3 males between 24 and 33 years old) and 2 patients with transmural infarction of the myocardium. For all subjects, C-MRI, T-MRI, and Delayed-Enhancement MRI of Gadolinium (DE-MRI) images were acquired in breath-hold by using a General Electric Signa CV/i, 1.5 T scanner (General Electric, Milwaukee, USA). Healthy volunteers were also imaged with DE-MRI to have a proof of their clinical status. The values of acquisition parameters were: slice thickness = 8mm, in-plane resolution = 0.78mm $\times$ 0.78mm, gap between slices = 0mm, TR=7.99ms, TE=4.43ms, flip angle = 20 degrees, and FOV=40cm$\times$40cm. C-MRI and T-MRI sequences were acquired at 30 phases per cardiac cycle. T-MRI images with a grid pattern of 5mm (tag spacing) were acquired by applying a Spatial Modulation of Magnetization (SPAMM) sequence. An expert clinician assessed the presence of infarction from DE-MRI images, and classified the 17 standard segments [83] according to the transmurality of necrosis in the myocardial wall into four categories: i) 0% (healthy segment) ii) $<$50%, iii) 50-75% and iv) $>$ 75%. For patients with myocardial infarction, cardiac catheterization was also performed in order to assess coronary occlusion.

4.2.2 Deformation model

Figure 4.2 presents a block diagram of the method. Transformations are defined relative to the coordinate system of the first frame to simplify the computation of Lagrangian strains (referred to ED) and metric derivatives. The use of Lagrangian strains is more common than natural strains[1] in most current imaging techniques (US, MR, SPECT, angiography) [84]. Similarly to [81], the α-entropy H_α was used to measure the joint similarity of all phases.

Typically, a T-MRI study consists of two acquisitions performed in SA and LA. This results in two image sequences $I_{SA}(\mathbf{x}, t)$ and $I_{LA}(\mathbf{x}, t)$ of n_p phases which provide the voxel intensity at spatial position $\mathbf{x}$ and time t. Cardiac deformation was modeled as a set of $n_p - 1$ B-Splines $\mathcal{T}(\mathbf{x}) = \{T_i(\mathbf{x})\}_{i=1:n_p-1}$ transformations defined on $I_{SA}(\mathbf{x}, 0)$. The corresponding deformations in LA can be obtained from $\mathcal{T}(\mathbf{x})$ by composition of $\mathcal{T}(\mathbf{x})$ with the rigid transformations defining the relationship between both coordinate systems, as described in Section 4.2.5.

4.2.3 Joint vs pairwise alignment

We explain the advantage of the simultaneous multi-image registration and the pairwise registration by adopting the generative model representation of the image

[1] The natural strain ε_N is defined as the integral over time of the instantaneous strain, i.e. $\varepsilon_N = \int_{t1}^{t2} \frac{dL}{L}$

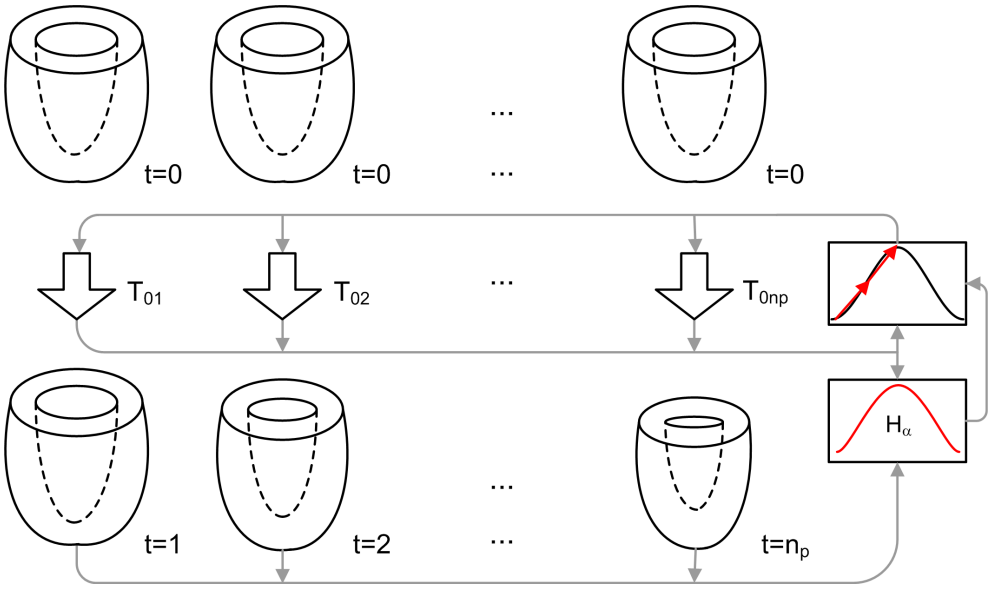

Figure 4.2: Cardiac motion estimation method. Transformations T_{0i} mapping points in ED (top) to phase i (bottom) are optimized simultaneously to minimize the H_α of all phases. The inputs to the optimizer are the set of transformations $\mathcal{T}$ and the metric of similarity. This metric takes in turn all images of the sequence as input.

registration problem. A generative model for the image registration problem is obtained by expressing the log posterior probability of the deformation (B-spline parameters $\mathbf{B}$) given the image sequence [85]:

$$\ln p(\mathbf{B}|\mathbf{Z}) = -H(\mathbf{Z}|\mathbf{B})N + \ln p(\mathbf{B}) \tag{4.1}$$

where N is the total number of pixels, $\mathbf{Z}$ is a random vector of dimension n_p, called a pixel stack, whose realizations are the time series of grey levels at a specified pixel location over successive image volumes in the time sequence. Each realization $\mathbf{z}$ ranges over the set $\{0, 2^{n^q}\}^{n_p}$ where n^q is the number of bits quantifying image intensities. In Equation 4.1, $p(\mathbf{B})$ is a prior on the deformation that influences how the estimated deformations interpolate between features in the images [86].

The conditional entropy on the right hand side of Equation 4.1 can be empirically estimated from Shannon entropy using [36]:

$$\begin{aligned} H(\mathbf{Z}|\mathbf{B}) &= \sum_i p(\mathbf{Z}(\mathbf{x}) = \mathbf{z}_i|\mathbf{B}) \ln p(\mathbf{Z}(\mathbf{x}) = \mathbf{z}_i|\mathbf{B}) \\ &\approxeq -N^{-1} \sum_i N_i \ln N_i + \ln N \end{aligned} \tag{4.2}$$

where $N_i = \sum_{j:\mathbf{Z}(\mathbf{x}_j)=\mathbf{z}_i}$ is the number of pixel locations where the associated vector $\mathbf{Z}(\mathbf{x}_j)$ equals grey level $\mathbf{z}_i$ and satisfies $\sum_i N_i = N$.

The problem of course is that the log posterior (4.1) is not computable due to the fact that required memory explodes as n_p increases (memory scales as $2^{n_p \cdot n_q}$). This is the justification of alternative direct methods of estimating the entropy. The MST/kNNG alpha-entropy estimators converge in probability to $H(\mathbf{Z}|\mathbf{B})$ for large N and n_p. This is because for large N the alpha-entropy estimator converges to the alpha-entropy, by the law of large numbers, and for large n_p, $\alpha = (n_p - 1)/n_p \approx 1$, and the alpha-entropy is approximately equal to the Shannon entropy.

Therefore, in light of the representation (4.1) of the log posterior density, the PA approach corresponds to making an approximation to the entropy function defining the log posterior $H(\mathbf{Z}|\mathbf{B}) \approx \sum_{j=0}^{n_p-1} H(I_j, I_{j+1}|\mathbf{B})$ where I_j denotes the j-th image volume in the sequence. Such approximation to the full joint entropy is expected to be poor when a frame of the image sequence is correlated to more than just its neighboring frames, or more generally when pairwise independence of the sequence does not imply joint independence. When the decomposition of the joint distribution into pairwise successive products gives a poor approximation to the true log posterior (4.1) the PA method will perform poorly. For example, using standard arguments of mathematical statistics it can be shown that in the limit as N becomes large, maximization of the pairwise entropy will give a biased estimator of the deformation parameters $\mathbf{B}$, equal to the *least false estimate* [87] of $\mathbf{B}$.

Classical estimators of entropy use plug-in estimation, i. e. estimate the PDF $p(\mathbf{Z}|\mathcal{Z})$ from observed data $\mathcal{Z}$. In this chapter, a kNNG estimator for H_α is proposed

based on the paper by Neemuchwala *et al.* [72]. For random vector $\mathbf{Z} = [Z_1 \cdots Z_{n_p}]^T$ the Rényi entropy H_α of order α of $\mathbf{Z}$ is defined as [88]:

$$H_\alpha(\mathbf{Z}) = \frac{1}{\alpha - 1} \log \int f(Z_1, ..., Z_n)^\alpha dZ_1 ... dZ_{n_p} \tag{4.3}$$

If $\hat{f}_\mathbf{Z}$ is a consistent estimator of the PDF, i.e. if it converges in probability to $f_\mathbf{Z}$ as the number of samples grows, then Equation 4.3 can be approximated by

$$\widehat{H}_\alpha(\mathbf{Z}) = \frac{1}{\alpha - 1} \log \frac{1}{n_s} \sum_{i=1}^{n_s} \left(\hat{f}_\mathbf{Z}(\mathbf{z}_i) \right)^{\alpha - 1} \tag{4.4}$$

where the $\mathbf{z}_i = (I(\mathbf{x}, 0 : n_p - 1)) \in \mathbb{R}^{n_p}$ denote realizations of the multivariate random variable $\mathbf{Z}$ and n_s is the number of realizations (number of samples).

Finally, the application of a *k*NNG-Voronoi partitioning heuristic [68] allows substituting $\hat{f}_\mathbf{Z}$ with $1/(n_s e_i(\mathcal{Z}))$, for obtaining the *k*NNG estimator of H_α:

$$\widehat{H}_\alpha(\mathbf{Z}) = \frac{1}{\alpha - 1} \log \frac{1}{n_s^\alpha} \sum_{i=1}^{n_s} \left(e_\mathcal{Z}^{n_p}(\mathbf{z}_i) \right)^{1 - \alpha} \tag{4.5}$$

where $e_\mathcal{Z}(\mathbf{z}_i) = \|\mathbf{z}_i - \tilde{\mathbf{z}}_i\|$ is the euclidean distance from the point $\mathbf{z}_i$ to its nearest neighbor $\tilde{\mathbf{z}}_i$ in $\mathcal{Z}$.

There is a difference between the entropy estimation approach taken by Learned-Miller [85] and the approach adopted in this chapter. Learned-Miller assumes that intensities are independently and identically distributed (i.i.d.) both over all pixel locations and over all images *inside* each pixel stack. Using these two assumptions, the problem is reduced to the computation of the entropy of a scalar random variable. While the assumption of independent images inside the pixel stack $\mathbf{Z}$ is reasonable in the case of independent subjects, it can not be maintained in our case since we focus on temporal sequences where consecutive images are expected to be highly dependent. As consequence, entropy must be estimated in a space of high dimensionality without any constraint about component independency in $\mathbf{Z}$. The estimator in Equation 4.5 only assumes i.i.d realizations of $\mathbf{Z}$, and therefore is suitable for our application .

In the Appendix 4.A we present an analytical expression for computing the gradient $\nabla \widehat{H}_\alpha(\mathbf{B})$ of the estimator in Equation 4.5.

4.2.4 Self matches

The estimator defined in Equation 4.5 is numerically unstable when any of the distances $e_\mathcal{Z}(\cdot)$ is equal to zero, i.e. in case of self matches in the nearest neighbors (NN) query. If $\mathbf{Z}$ was effectively continuous, it would produce realizations through the whole range of possible values, without any repetition. However, digital images are quantized and represented by a finite number of bits, and there exists the

possibility of finding multiple occurrences of a specific value $\mathbf{z}^*$ in $\mathcal{Z}$. In order to solve this problem, Neemuchwala *et al.* [72] added uniform noise to each realization, thus dispersing features inside a radius-limited n_p-hypersphere. Even when this approach effectively solves the problem, it might generate arbitrarily large values in the PDF estimation. A small change in a point $\mathbf{z}^*$ results in a small Voronoi cell and therefore, in an elevated probability value for $\mathbf{z}^*$. Another drawback of noise addition is the introduction of unnecessary stochastic component in the cost function, which in turn could interfere with the optimization process.

In this chapter, a different approach was adopted for the self-matching problem. In Equation 4.5 we multiplied the distance $e_{\mathcal{Z}}(\mathbf{z}_i)$ by the number of occurrences $o_{\mathcal{Z}}(\mathbf{z}_i)$ of $\mathbf{z}_i$ in $\mathcal{Z}$. Even when this requires a second NN search, the additional computational cost is negligible [89].

4.2.5 Combination of views

A T-MRI study typically contains SA and LA views of the heart. The information about radial and circumferential contraction is provided by the SA and LA[2] views, whereas the information about longitudinal deformation comes only from the LA view. Therefore, it is necessary to include the information provided by both views in the registration process. Chandrashekara *et al.* [12] circumvented this problem by linearly combining the similarity metrics measured independently for each view. In order to obtain a *unified metric* considering *multiple views* and *multiple time points*, each view was considered as realizations of the same random vector $\mathbf{Z}$. This means that pixel stacks $\mathbf{z}^{sa}$ and $\mathbf{z}^{la}$ taken from SA and LA are modeled as realizations of the same variable $\mathbf{Z}$, and can thus be mixed into a single set of samples $\mathcal{Z}$. Under this hypothesis, Equation 4.3 remains unchanged for registration of multiple view sequences, integrating in this way information from different time points and views into the same unified framework.

By convention, SA has been taken as the reference space for defining the transformation. Thus, the coordinates of samples in LA must be mapped to SA in order to be transformed. These transformed coordinates need then to be mapped back to LA for computing the pixel stack $\mathbf{z}^{la}$. Therefore, it is necessary to know the transformations from SA to LA (T_{sl}) and from LA to SA (T_{ls}). These transformations are provided by the DICOM format in the form of image origin $\mathbf{o}_w^{sa}$ and orientation $\mathbf{D}_w^{sa} = [\mathbf{i}^{sa}\ \mathbf{j}^{sa}\ \mathbf{k}^{sa}]$ ($\mathbf{o}_w^{la}$ and $\mathbf{D}_w^{la} = [\mathbf{i}^{la}\ \mathbf{j}^{la}\ \mathbf{k}^{la}]$) with respect to the coordinate system of the scanner. Two generic points $\mathbf{x}_i^{sa}$ and $\mathbf{x}_i^{la}$ in image coordinates can be expressed in world coordinates as :

$$\mathbf{x}_w^{sa} = \mathbf{o}_w^{sa} + \mathbf{D}_w^{sa}\mathbf{x}_i^{sa} \tag{4.6}$$

[2]In this chapter, a grid tag pattern was employed instead of unidirectional tags. Therefore, the longitudinal images also contain information about the radial contraction

$$\mathbf{x}_w^{la} = \mathbf{o}_w^{la} + \mathbf{D}_w^{la}\mathbf{x}_i^{la} \tag{4.7}$$

When Equations 4.6 and 4.7 refer to the same physical point, we can equate the right sides and obtain the following transformations between views:

$$T_{sl} : \mathbf{x}_i^{sa} \rightarrow \mathbf{x}_i^{la} = \left(\mathbf{D}_w^{la}\right)^T \mathbf{D}_w^{sa}\mathbf{x}_i^{sa} + \left(\mathbf{D}_w^{la}\right)^T \left(\mathbf{o}_w^{sa} - \mathbf{o}_w^{la}\right) \tag{4.8}$$

$$T_{ls} : \mathbf{x}_i^{la} \rightarrow \mathbf{x}_i^{sa} = \left(\mathbf{D}_w^{sa}\right)^T \mathbf{D}_w^{la}\mathbf{x}_i^{la} + \left(\mathbf{D}_w^{sa}\right)^T \left(\mathbf{o}_w^{la} - \mathbf{o}_w^{sa}\right) \tag{4.9}$$

4.2.6 Strain estimation

The mechanical effects and evolution over time of myocardial infarction are an important issue to study with T-MRI [11]. The infarcted region of diseased myocardium permanently loses its ability to contract, and this is manifested in altered motion during the cardiac cycle. Therefore, there should be a correlation between infarction location and local strains. To study this correspondence, strain was computed from the recovered displacements fields to discriminate between active healthy myocardium and passively moving infarcted tissue.

The set of transformations $\mathcal{T}$ allows to compute the displacement field $\mathbf{u}(\mathbf{x})$ as function of position $\mathbf{x}$ at ED and time t. Since the assumption of small deformations is too strong for cardiac deformations, the Green strain tensor cannot be applied, and the Green-Lagrange strain tensor must be used instead. The Green-Lagrange strain tensor is defined as [90]

$$\mathbf{E} = \frac{1}{2}\left(\nabla\mathbf{u} + \nabla\mathbf{u}^T + \nabla\mathbf{u}^T\nabla\mathbf{u}\right) \tag{4.10}$$

Diagonal elements ε_{ii} of $\mathbf{E}$ are normal strains, i.e. strains along each direction in the rectangular coordinate system. Given the geometry of the heart, this coordinate system is not appropriate for analysis. Instead, it is preferable the use of a local coordinate system composed by radial, circumferential, and longitudinal directions (rcl system) on the basis of the epicardial surface orientation at the reference (undeformed) geometry. This coordinate system is illustrated in Figure 4.3. In order to estimate the epicardial surface, a manual segmentation of the SA image at ED was performed and, after resampling and smoothing, a variant [91] of the original marching cubes algorithm [92] was applied to extract the epicardial and endocardial surfaces.

The normal strain along an arbitrary direction $\mathbf{d}$ can be then obtained from Equation 5.1 as [93]:

$$\varepsilon_{dd} = \mathbf{d}^T\mathbf{E}\mathbf{d} \tag{4.11}$$

Radial (ε_{rr}), circumferential (ε_{cc}), and longitudinal (ε_{ll}) normal strains can be obtained by replacing $\mathbf{d}$ with directions $\mathbf{r}$, $\mathbf{c}$, and $\mathbf{l}$, respectively.

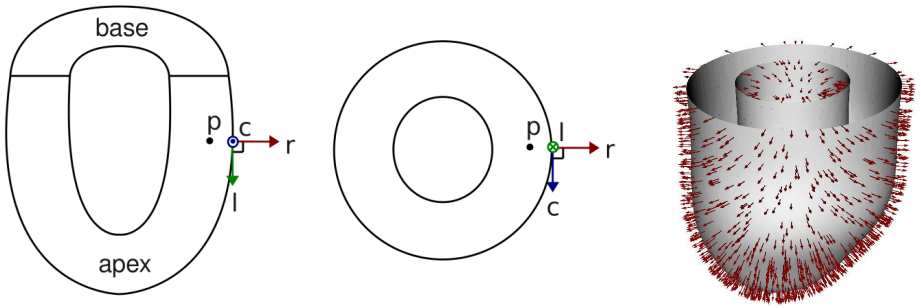

Figure 4.3: Local coordinate system used for strain analysis. Radial (**r**), circumferential (**c**), and longitudinal (**l**) directions for the point **p** are shown in the longitudinal (a) and transverse (b) views of the LV. (c) Radial directions obtained from the extracted epicardial and endocardial surfaces of the LV.

The radial direction is outward and perpendicular to the epicardial surface. The circumferential direction is in the short-axis plane (perpendicular to the long axis), parallel to the epicardial surface, and counterclock wise, as viewed from the base. The longitudinal direction is obtained as the cross product of radial and circumferential directions, tangent to the epicardial surface. In this way, directions were defined to create a right-handed system.

4.3 Results

4.3.1 Entropy

After registration, H_α should be minimum, and the pixel stack distribution ($\mathcal{Z}$) should be more compact. Since the pixel stacks $\mathbf{z}_i$ are n_p-dimensional points, a reduction of dimensionality is necessary for visual representation of changes in distribution. A Principal Components Analysis (PCA) [94] was performed to accomplish a projection of $\mathcal{Z}$ in the subspace spanned by the first three principal components $\lambda_{i=1:3}$ was used to visualize point distributions in this space. Figure 4.4 shows that the point distribution before registration presents a larger variance than after registration, equivalent to a state of higher entropy, as expected.

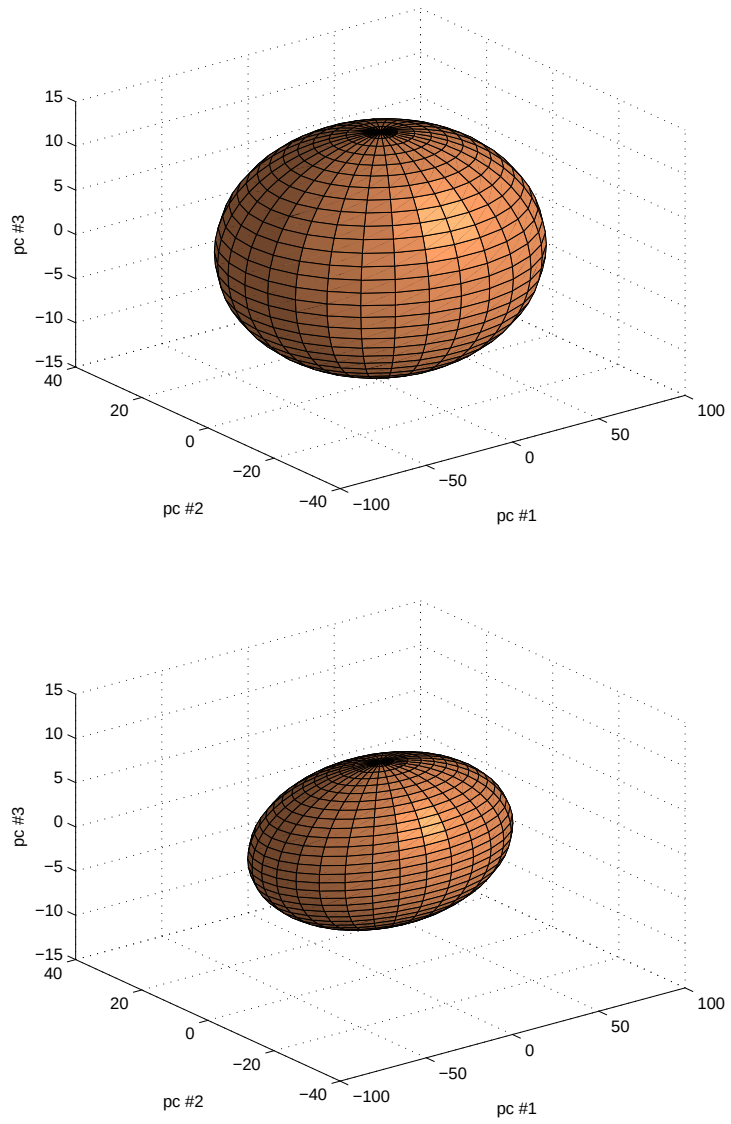

Figure 4.4: Distributions of the pixel stack $\mathbf{Z}$ in the subspace spanned by the first three principal component directions $\mathbf{q}_{i=1:3}$. (a) Before registration. (b) After registration. Ellipsoids have semi-axis lengths equal to the standard deviation along the corresponding principal vectors $\mathbf{q}$.

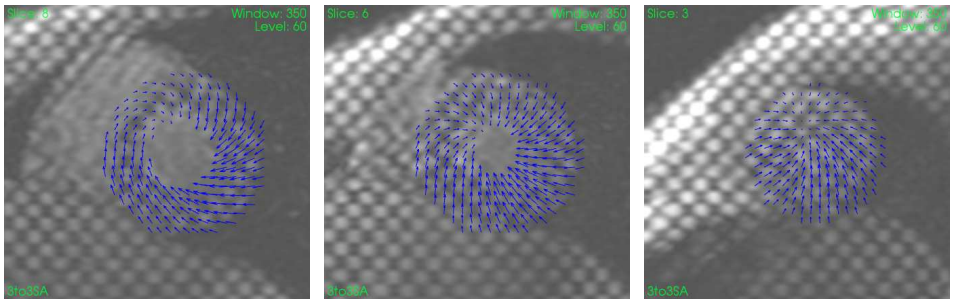

(a) (b) (c)

Figure 4.5: Example of displacement field at ES (relative to ED) for a healthy volunteer at (a) base, (b) mid, and (c) apex. The displacement field is plotted on the SA images at ED.

4.3.2 Error analysis

Figure 4.5 shows the displacement field for a healthy volunteer. In order to compute accuracy, tag intersections were marked in the systolic phases of 6 sequences. Only systolic phases were marked since the images were acquired by using SPAMM, and the strong fading effect of this sequence makes the tags difficult to identify beyond ES. The resulting transformations $\mathcal{T}^*$ were used to propagate the points in ED to the remaining phases, which were compared to manual measurements extracted by an expert clinician. Tag intersections were marked in SA at base, mid, and apex, whereas only the central plane was used in LA. On average, 24 tag intersections were tracked along the systole.

Figure 4.6 displays the Mean Square Error (MSE) error along the systole of the JA method as compared to the PA method [3]. Figure 4.6 shows a lower MSE error for JA for 37 out of the 39 phases. The MSE error is higher only for phase #5 of sequence #5, and phase #2 of sequence #4. It is important to assess the statistical significances of these errors and a Mann-Whitney test [96] was implemented to extract p-values for each of the deformations. Normality was verified at level 0.05 by using a Lilliefors test [97], and the Independence of population was ensured by applying each method to a different set of sequences. Table 4.1 shows rejection of the null hypothesis at 5% significance level for almost all phases, showing an improvement in favor of the JA method.

Differences in error variance were also studied in order to assess uniformity of the registration error across regions. It is desirable that registration accuracy be independent of the displacement magnitude, which varies across the myocardium during the cardiac cycle. The error uniformity can be measured by computing its

[3] An own implementation of the method by Chandrashekara *et al.* (using the Insight Toolkit [95]) was employed, instead of their original software.

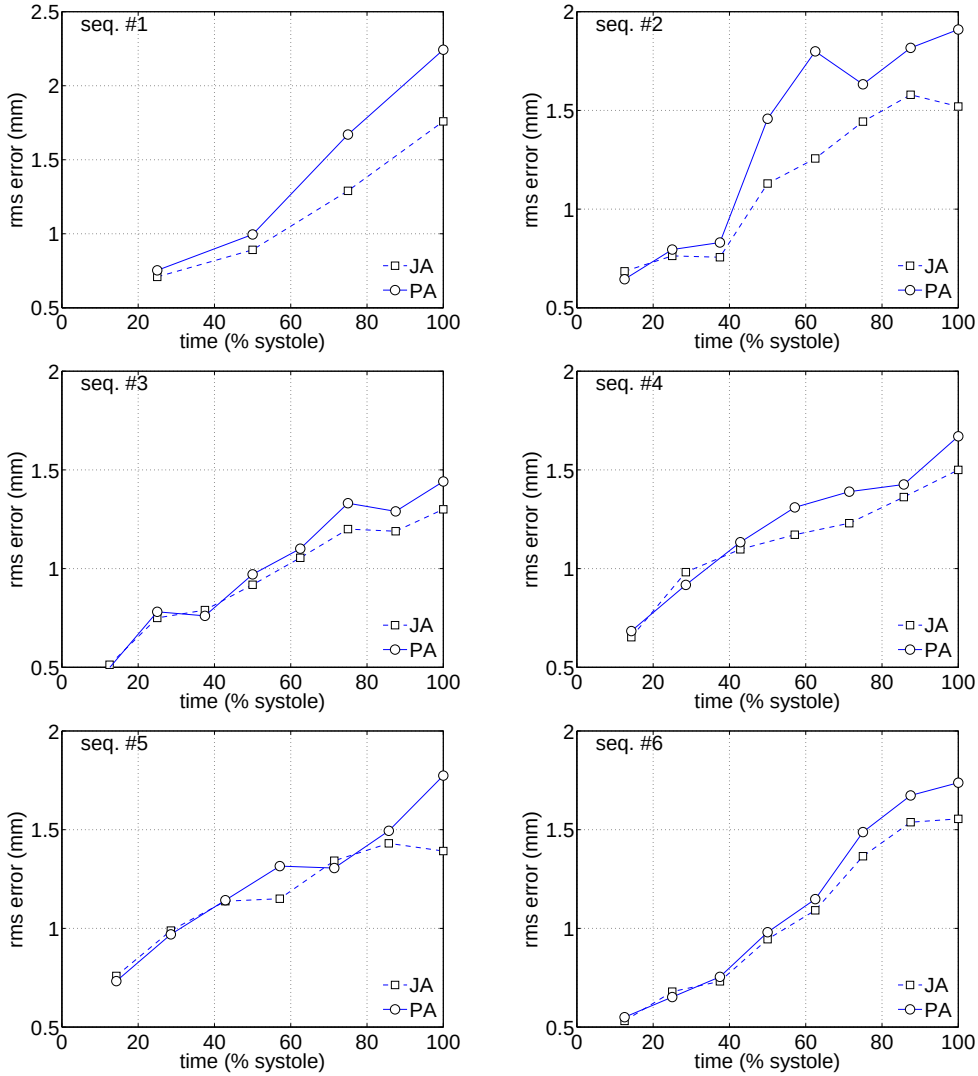

Figure 4.6: MSE errors between manually placed landmarks at tag intersections, and propagated landmarks for six healthy volunteers. JA = joint alignment; PA = pairwise alignment.

Table 4.1: p-values obtained from the Mann-Whitney test performed on the MSE errors for JA and PA methods. Results are provided for equally spaced time instants along systole. Bold values mean rejection of the null hypothesis at 5% significance level. Note that the null hypothesis is rejected for all phases at 10% significance level.

t (relative to systole)	14%	28%	43%	57%	71%	86%	100%
p-value	**0.02%**	**1.3%**	**0.2%**	**1.3%**	9.6%	**0.8%**	**0.03%**

Table 4.2: p-values obtained with a F-test performed on error variances for JA and PA methods. Bold values mean rejection of the null hypothesis of equal variances (p=0.05).

t (relative to systole)	14%	28%	43%	57%	71%	86%	100%
p-value	29%	**4.2%**	**0.0006%**	**0.1%**	**0.0043%**	**4.3%**	**0.8%**

variance. Table 4.2 shows the p-values obtained from a F-test [96] performed on the variances for each phase. As in the previous Mann-Whitney test for mean error values, each method was applied on different sequences to ensure independence. The same values are represented in form of box plots in Figure 4.7.

Finally, the JA method was compared to manual measurements in order to assess dependencies of the registration error on the displacement magnitude. The Bland-Altman plots [96] presented in Figure 4.9 show a negligible bias, and a symmetric error distribution around it.

4.3.3 Computational complexity and speed

Registration using plug-in estimators of probability density functions suffers from increasingly high computation as the number of features increases. On the other hand, registration based on graphs suffers from high computational cost that increases in the number of feature realizations. Analytical computation of the gradient of the cost function can reduce this complexity. This reduction in complexity is especially advantageous when using transformations with high number of parameters. For example, if B-Splines are employed, even a coarse grid with control points every 20 mm over the LV contains $8\times8\times8\times3$ = 1,536 parameters, and the gradient estimation requires 3,072 function evaluations, i.e. building 3,072 graphs. The use of analytical expressions resulted in an average computation time of 45 min for a PC with a 64 bits processor Intel Itanium at 1.5 GHz running Linux Suse 9.2. Figure 4.8 shows a linear increase in computation time with the number of points used to estimate H_α (the size of $\mathcal{Z}$).

4.3.4 Strain in healthy subjects

Strain analysis along systole was performed by dividing the LV into the standard 16 segments of the American Heart Association (AHA) [83] (the 17^{th} segment is

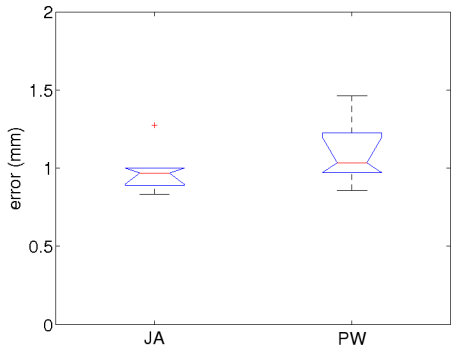

Figure 4.7: Box plots of the MSE errors showing the difference in variance between joint alignment (JA) and pairwise alignment (PW).

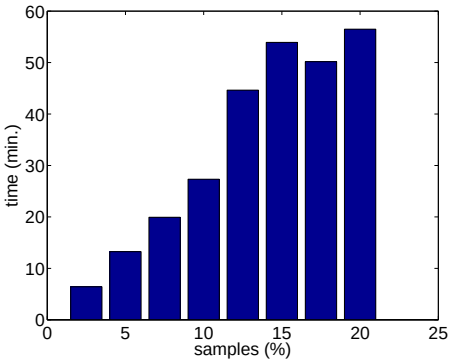

Figure 4.8: Average registration time as a function of the number of samples used for estimating H_α (expressed as percent of the number of voxels of the ROI containing the LV)

optional). The average and standard deviation of radial, circumferential, and longitudinal strain were computed for the 6 healthy subjects. The strain analysis was constrained to systole because of the same data acquisition issues mentioned in Section 4.3.2. Figures 4.10, 4.11, and 4.12 show these values along systole. Radial strain presented the highest variability in agreement with previous reports [98, 99]. The strain sign is consistent with the heart physiology: during systole there is radial thickening (positive strain), and circumferential and longitudinal shortening (negative strain). Tables 4.3, 4.4, and 4.5 show average radial and circumferential peak strains and standard deviations compared to values reported in the literature.

4.3.5 Strain in myocardial infarction

In order to test the method in pathological cases, a strain analysis was performed on two patients with myocardial infarction. Figure 4.13 shows the infarction location, regions at risk, and circumferential strains for these patients. This analysis consisted in a segment-to-segment comparison of circumferential strain with respect to the normal subjects. The choice of circumferential strain for comparison is due to the small intersubject variability of healthy subjects as compared to radial and longitudinal strain. This makes the detection of any deviation in strain easier with respect to normal values. Figure 4.13 shows that for patient #1 the largest deviations with respect to normality are found in segments BI, MI, and AI. These lower strains fully correlate with the infarction location at the inferior area of the LV. Segments BA, MA, and BAS showed an increased strain on the opposite side of the infarction, which could be explained as a compensatory mechanism of healthy seg-

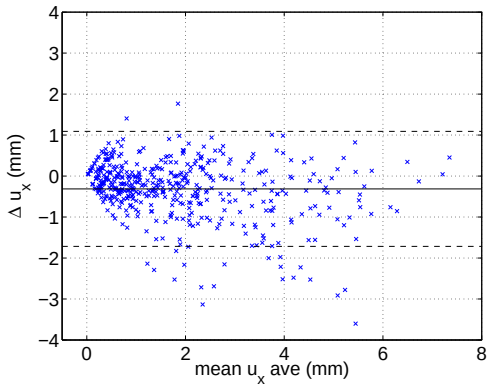

(a)

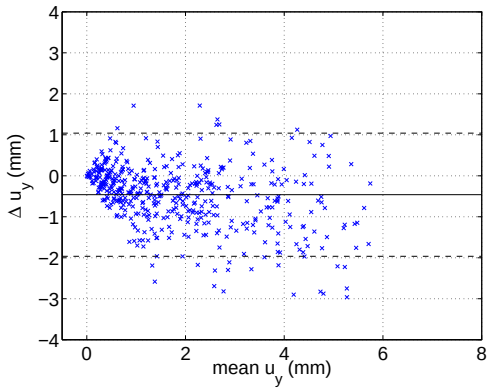

(b)

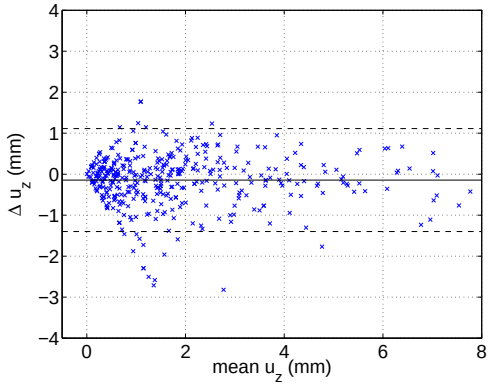

(c)

Figure 4.9: Bland-Altman plots of displacements along x (a), y (b), and z (c) axes (Δu_x,Δu_y, and Δu_z). Solid and dashed lines show respectively the mean value and the 95% confidence interval of point displacements.

Table 4.3: Comparison of average peak radial strains $\overline{E}_{rr}$ and standard deviations σ_{rr} with values reported in the literature. Non-available values are marked as n/a.

Region		**Moore *et al.* [98]**	**Bistoquet *et al.* [100]**	**Our method**
septum	basal	0.45 ± 0.12	$0.20 \pm n/a$	0.21 ± 0.10
	mid	0.42 ± 0.19	$0.21 \pm n/a$	0.26 ± 0.08
	apical	0.36 ± 0.22	n/a	0.10 ± 0.07
anterior	basal	0.42 ± 0.21	$0.21 \pm n/a$	0.27 ± 0.08
	mid	0.52 ± 0.25	$0.25 \pm n/a$	0.26 ± 0.08
	apical	0.67 ± 0.31	n/a	0.13 ± 0.05
lateral	basal	0.52 ± 0.19	$0.22 \pm n/a$	0.26 ± 0.09
	mid	0.38 ± 0.18	$0.21 \pm n/a$	0.23 ± 0.07
	apical	0.49 ± 0.29	n/a	0.15 ± 0.09
inferior	basal	0.41 ± 0.17	$0.23 \pm n/a$	0.26 ± 0.06
	mid	0.35 ± 0.22	$0.23 \pm n/a$	0.19 ± 0.05
	apical	0.39 ± 0.38	n/a	0.10 ± 0.05

Table 4.4: Comparison of average peak circumferential strains $\overline{E}_{cc}$ and standard deviations σ_{cc} with values reported in the literature. Non-available values are marked as n/a.

Region		**Moore *et al.* [98]**	**Korosoglou *et al.* [101]**	**Petitjean *et al.* [99]**	**Bistoquet *et al.* [100]**	**Our method**
septum	basal	-0.17 ± 0.03	$-0.18 \pm n/a$	-0.18 ± 0.09	$-0.10 \pm n/a$	-0.13 ± 0.03
	mid	-0.16 ± 0.03	$-0.19 \pm n/a$	-0.27 ± 0.18	$-0.12 \pm n/a$	-0.14 ± 0.03
	apical	-0.18 ± 0.03	$-0.19 \pm n/a$	-0.27 ± 0.27	n/a	-0.08 ± 0.02
anterior	basal	-0.20 ± 0.03	n/a	-0.36 ± 0.27	$-0.12 \pm n/a$	-0.07 ± 0.01
	mid	-0.23 ± 0.04	n/a	-0.45 ± 0.13	$-0.10 \pm n/a$	-0.08 ± 0.03
	apical	-0.24 ± 0.06	n/a	-0.49 ± 0.27	n/a	-0.06 ± 0.03
lateral	basal	-0.21 ± 0.03	$-0.19 \pm n/a$	-0.45 ± 0.13	$-0.12 \pm n/a$	-0.10 ± 0.03
	mid	-0.22 ± 0.03	$-0.19 \pm n/a$	-0.45 ± 0.13	$-0.11 \pm n/a$	-0.14 ± 0.02
	apical	-0.24 ± 0.04	$-0.19 \pm n/a$	-0.27 ± 0.27	n/a	-0.12 ± 0.04
inferior	basal	-0.16 ± 0.03	n/a	-0.36 ± 0.13	$-0.10 \pm n/a$	-0.12 ± 0.03
	mid	-0.16 ± 0.05	n/a	-0.49 ± 0.18	$-0.11 \pm n/a$	-0.14 ± 0.01
	apical	-0.23 ± 0.04	n/a	-0.45 ± 0.27	n/a	-0.14 ± 0.02

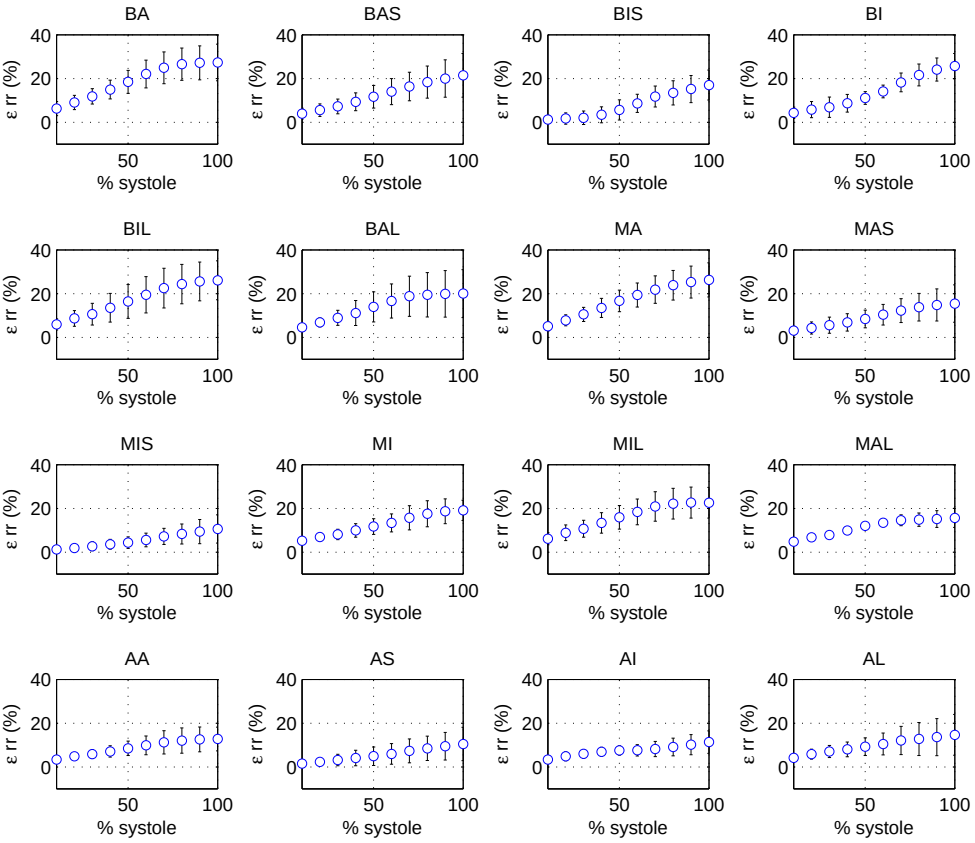

Figure 4.10: Radial strain along systole for healthy subjects. BA=basal anterior; BAS=basal anteroseptal; BIS=basal inferoseptal; BI=basal inferior; BIL=basal inferolateral; BAL=basal anterolateral; MA=mid anterior; MAS=mid anteroseptal; MIS=mid inferoseptal; MI=mid inferior; MIL=mid inferolateral; MAL=mid anterolateral; AA=apical anterior; AS=apical septal; AI=apical inferior; AL=apical lateral.

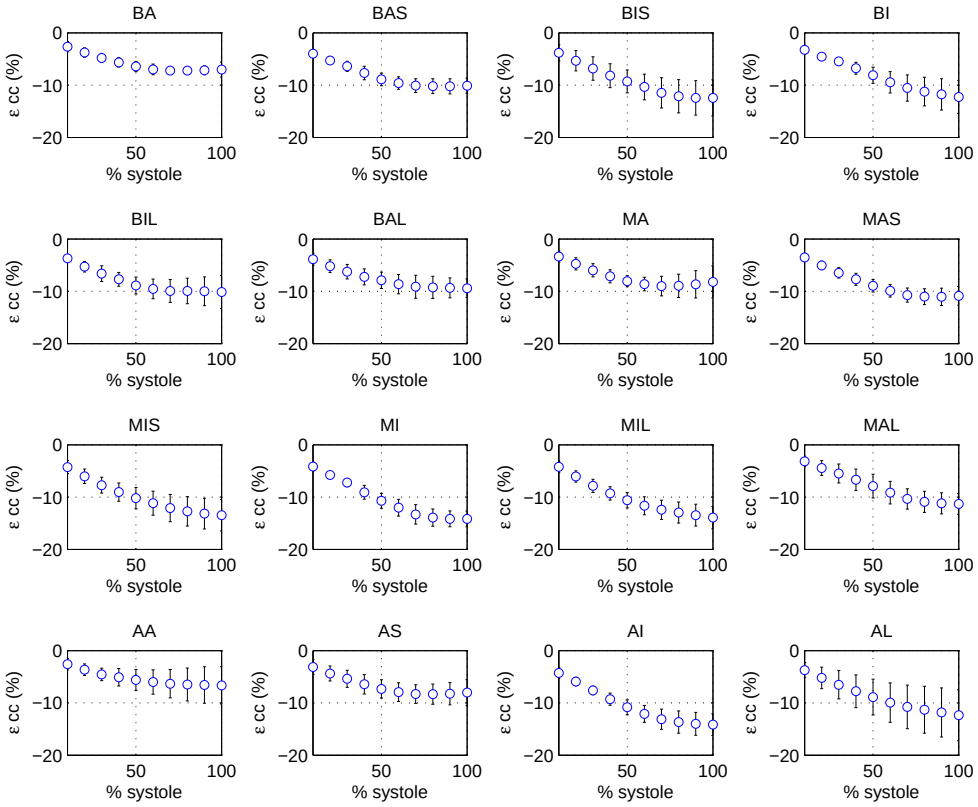

Figure 4.11: Circumferential strain along systole for healthy subjects. BA=basal anterior; BAS=basal anteroseptal; BIS=basal inferoseptal; BI=basal inferior; BIL=basal inferolateral; BAL=basal anterolateral; MA=mid anterior; MAS=mid anteroseptal; MIS=mid inferoseptal; MI=mid inferior; MIL=mid inferolateral; MAL=mid anterolateral; AA=apical anterior; AS=apical septal; AI=apical inferior; AL=apical lateral.

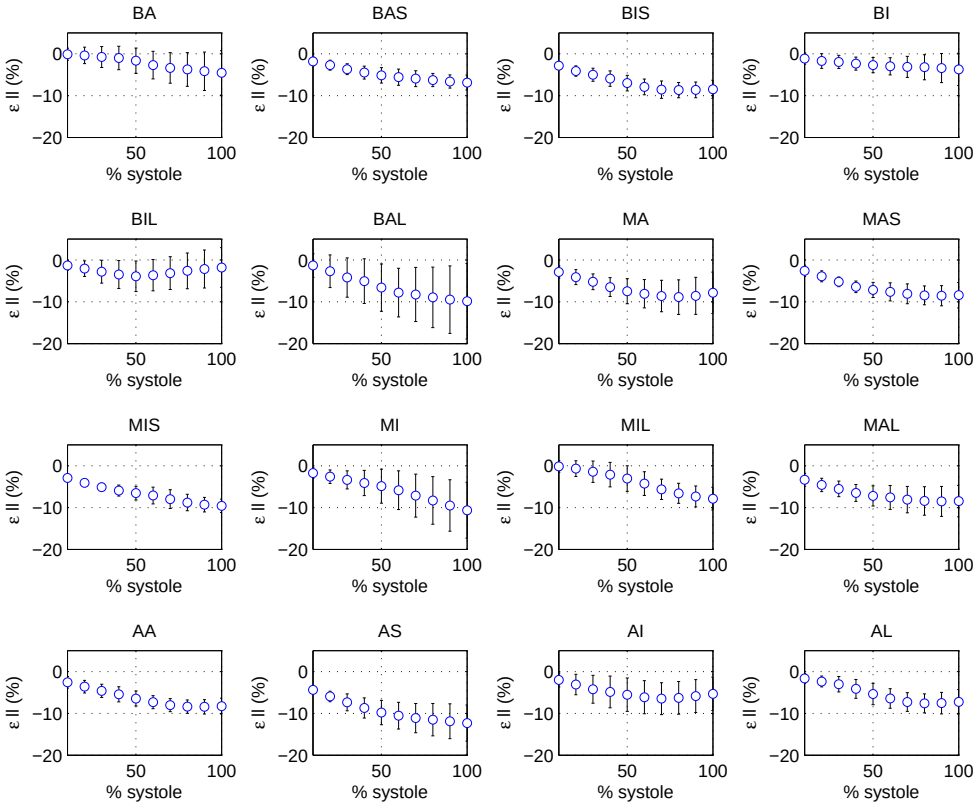

Figure 4.12: Longitudinal strain along systole for healthy subjects. BA=basal anterior; BAS=basal anteroseptal; BIS=basal inferoseptal; BI=basal inferior; BIL=basal inferolateral; BAL=basal anterolateral; MA=mid anterior; MAS=mid anteroseptal; MIS=mid inferoseptal; MI=mid inferior; MIL=mid inferolateral; MAL=mid anterolateral; AA=apical anterior; AS=apical septal; AI=apical inferior; AL=apical lateral.

Table 4.5: Comparison of average peak longitudinal strains $\overline{E}_{ll}$ and standard deviations σ_{ll} with values reported in the literature.

Region		Moore *et al.* [98]	Our method
septum	basal	-0.14 ± 0.03	-0.09 ± 0.02
	mid	-0.15 ± 0.03	-0.10 ± 0.02
	apical	-0.18 ± 0.04	-0.12 ± 0.04
anterior	basal	-0.15 ± 0.03	-0.05 ± 0.05
	mid	-0.15 ± 0.03	-0.09 ± 0.04
	apical	-0.19 ± 0.03	-0.08 ± 0.02
lateral	basal	-0.15 ± 0.03	-0.10 ± 0.09
	mid	-0.14 ± 0.04	-0.09 ± 0.04
	apical	-0.19 ± 0.03	-0.08 ± 0.03
inferior	basal	-0.15 ± 0.03	-0.04 ± 0.04
	mid	-0.15 ± 0.03	-0.11 ± 0.07
	apical	-0.18 ± 0.04	-0.07 ± 0.04

ments to maintain the systolic function close to normal level. In patient #2, again, all infarcted segments presented a lower strain with respect to the control group. Even when the lateral wall had no evidence of infarction according to DE-MRI, the circumflex artery presented a 75% of occlusion, which could explain the low strains obtained for this region.

4.4 Discussion

The MSE error with respect to manual measurements obtained by JA was shown to be significantly lower than for the PA approach at ES. The p-values obtained from the Mann-Whitney test (Table 4.1) show significant differences at 5% level between the errors obtained with PA and JA for most of the analyzed time points. If a 10 % level were considered, this difference would become significant for all time points.

The errors with respect to the manual landmarks are computed inside the same image plane, since the acquisition slice by slice does not allow to track tag intersections in the space. This is a limitation imposed by the way of acquiring volumes, and can be solved only with the design of new MRI sequences to produce 3D tag patterns [102].

Figure 4.6 shows an increase in the MSE error over time. However, an uniform error distribution along time was expected, because of the simultaneous parameter optimization and the use of a joint metric. In order to find an explanation to these results, manual measurements were repeated by the same observer, and the intraobserver error was evaluated over time. Figure 4.14, shows an increase in this error over time, meaning that intersections are more difficult to define for phases close to ES. These tag distortions (Figure 4.15) can be caused by the non-linear

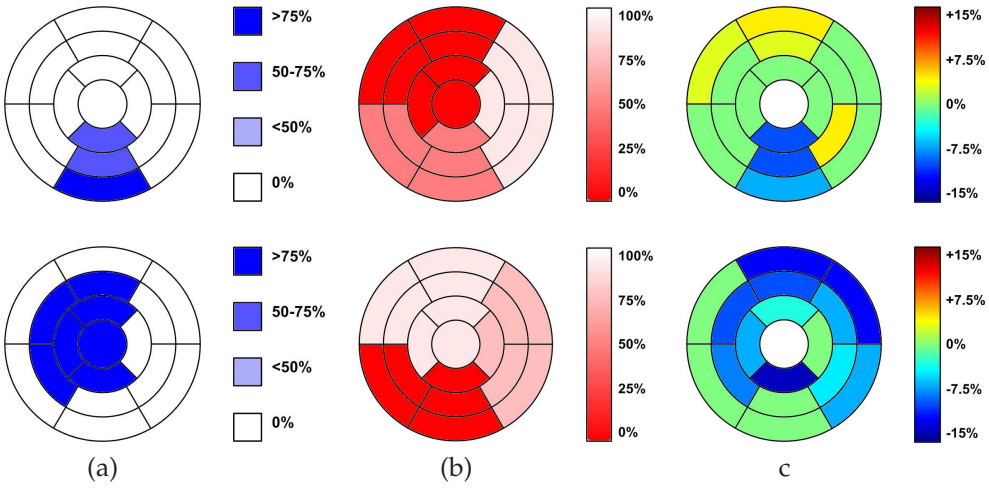

Figure 4.13: Relationship between infarction location, coronary occlusion *at risk*, and circumferential strains for the patients with MIA. (a) Transmurality of necrosis classified into four categories: i) 0% (healthy segment) ii) <50%, iii) 50-75% and iv) > 75%. (b) Percent of occlusion of the corresponding coronary artery. (c) Highest difference in circumferential strain with respect to the mean of the control group along systole. Differences lower than the standard deviations were arbitrarily set to zero.

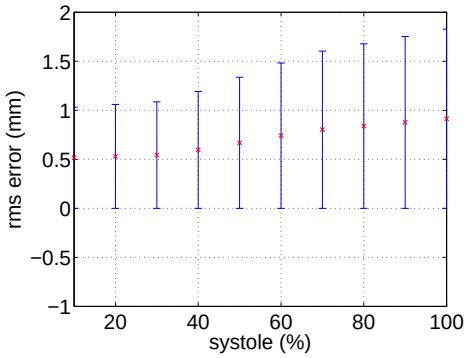

Figure 4.14: Intraobserver MSE error of manually placed landmarks at tag intersections.

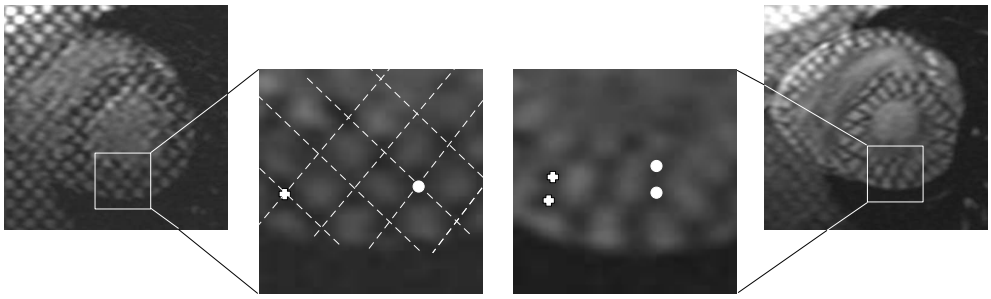

Figure 4.15: Tag distortion and its influence on the intraobserver error. A magnification of tags shows an ambiguity in point correspondence between ED (left) and ES (right) images. For the cross and circle at ED, there are two possible corresponding points at ES.

deformations undergone by the myocardium during contraction. Another source of registration error is out-of-plane motion, causing some tag intersections to vanish or dissapear. Therefore, there are some points in the myocardium for which a correspondence cannot be found for all time points. This is a well known registration problem [49, 103] that can hamper an accurate deformation recovery. Again, the availability of real 3D acquisitions could contribute to flatten out the error over time, since out-of-plane motion would not affect the tag pattern in this case.

In this chapter, the strain analysis was constrained to systole only because the tag fading precludes an accurately strain estimation beyond ES. The tag fading effect is quite strong in images acquired by using SPAMM, and other sequences like CSPAMM have been developed to reduce this problem [104]. *A priori*, there are no apparent problems preventing the application of the presented to the whole cardiac

cycle. Similar data acquisition issues explain the exclusion of the right ventricle (RV) of the analysis. The minimum tag spacing provided by the scanner used in this chapter was not sufficient to calculate strains accurately in the RV, but it could be included in the analysis in case of suitable image data.

There is an underestimation of the strain values reported in this chapter. The first frame of the sequence is usually discarded since the blood is still magnetized in ED, and because of the presence of artifacts similar to those produced by off-resonance and velocity-induced phase discontinuities [105]. In some cases even the second frame had to be discarded. As a consequence, the estimated strain values are lower than the real ones, and this could partially explain the differences found with the reported values in the literature. In our data, there are 10 frames during systole (in average), and therefore the descanted frames represent a loss of 10% to 20%.

A comparison of strain values to reported results in the literature revealed a large variability. This variability has several sources besides (of course) the employed method. The use of different datasets, segmentation algorithms, radial direction definitions, and ways of dividing the myocardium (the AHA standard division [83] has contributed a lot to normalize results), are some causes of these differences. Despite these problems, some common points were found. Radial strain presents always the highest values, and also the largest variability. Probably, this high variability is a consequence of its high dependence on the segmentation method and respiration artifacts. Even when sequences with severe artifacts were not used, this problem is present to some degree in all sequences, producing random local changes in the surface curvature (and therefore in the radial direction). On the contrary, circumferential direction is always in the plane of image acquisition, and does not change among subjects, which could explain the low variability of strain in this direction. Some methods to remove respiration artifacts in C-MRI have been proposed [106, 107], but they need to be modified for T-MRI images. A possibility is to apply tag removal methods [108], before using the mentioned techniques.

Preliminary tests on patients with myocardial infarction showed an agreement between the recovered and expected strain. Full correspondence between infarcted regions and low strain values was found, in agreement with previous results from studies with 2D US [109–114] and MRI [101, 115–117]. Of course, these experiments are only illustrative, and show consistent low strain values in infarction compared to other imaging and diagnostic modalities.

4.5 Conclusions

In this chapter, JA of T-MRI sequences was used for cardiac motion estimation. Since the success of similarity metrics based on information theory, H_α was em-

ployed to measure joint similarity. The use of this metric was justified from a probabilistic point of view in Section 4.2.3. In order to cope with the high computational cost of the kNNG estimators of H_α, an analytical expression for metric derivatives was obtained, resulting in a $O(n_s \, log \, n_s)$ complexity, which drastically reduces the registration time. The strategy to combine different views performed correctly, resulting in a simple way of integrating their information into a unified metric that measures multiphase and multiview similarity in image sequences. Results showed significantly lower mean errors and variances when compared to PA. Even when an uniform error distribution was expected, mean errors and variances increased over time. These observations can be attributed to image acquisition issues, which can be overcome with the advent of higher resolution scanners, and the possibility of performing 3D T-MRI [102]. Strain values corresponding to healthy subjects were in the order of magnitude reported in the literature. However, the lack of standardization, and the high number of sources of variability, make a direct comparison difficult. Strain values for patients with myocardial infarction showed an excellent visual correlation with infarction location and territories at risk. Even when these results are encouraging, experiments need to be extended to a larger population to confirm and generalize clinical conclusions.

4.A Appendix: analytical derivatives

Many optimizers need to estimate the gradient of the cost function. To this purpose, the use of finite difference approximation to the gradient is impractical for transformations with high number of parameters, since it requires computing a kd-tree for each perturbation of the set of parameters. This is especially problematic for high-dimensional feature spaces as the number of perturbations requires for the finite difference estimator is D. This problem of graph-based estimators has been addressed by Sabuncu *et al.* [118] for Minimum Spanning Tree (MST) estimators of H_α. Here we develop a similar analytical approximation.

Using Equation 4.5, the derivative with respect to the parameter m of the transformation is

$$\frac{\partial}{\partial p_m} \widehat{H}_\alpha = \frac{\sum_{i=1}^{n_s} \frac{\partial}{\partial p_m} \left\{ \left[e^2_{\mathcal{Z}}(\mathbf{z}_i) \right]^{\frac{\gamma}{2}} \right\}}{(\alpha - 1) \sum_{i=1}^{n_s} \left[e^2_{\mathcal{Z}}(\mathbf{z}_i) \right]^{\frac{\gamma}{2}}} \tag{4.12}$$

$$\frac{\partial}{\partial p_m} \widehat{H}_\alpha = \frac{-n_p \sum_{i=1}^{n_s} \left[e^2_{\mathcal{Z}}(\mathbf{z}_i) \right]^{(\frac{\gamma}{2}-1)} \frac{\partial}{\partial p_m} \left[e^2_{\mathcal{Z}}(\mathbf{z}_i) \right]}{2 \sum_{i=1}^{n_s} \left[e^2_{\mathcal{Z}}(\mathbf{z}_i) \right]^{\frac{\gamma}{2}}} \tag{4.13}$$

where $\gamma = n_p(1 - \alpha)$, as defined in [119].

The problem has been reduced to computation of derivatives $e^2_{\mathcal{Z}}(\mathbf{z}^*_i)$. By assuming no changes in correspondence between a point $\mathbf{z}_i$ and its nearest neighbor $\tilde{\mathbf{z}}_i$ for infinitesimal changes in the transformation parameters, these derivatives can be computed as:

$$\frac{\partial}{\partial p_m} e^2_{\mathcal{Z}}(\mathbf{z}_i) = \sum_{j=1}^{n_p} 2(z_{ij} - \tilde{z}_{ij})(\mathbf{J}^m_T(\mathbf{x}_j))^T \nabla z_{ij} \tag{4.14}$$

where ∇z_{ij} is the intensity gradient at the point $\mathbf{x}_j = T(\mathbf{x}_i)$, and $\mathbf{J}^m_T$ is the m^{th} column of the parametric jacobian of the transformation [95]:

$$\mathbf{J}_T = \begin{bmatrix} \frac{\partial x_1}{\partial p_1} & \frac{\partial x_1}{\partial p_2} & \cdots & \frac{\partial x_1}{\partial p_m} \\ \frac{\partial x_2}{\partial p_1} & \frac{\partial x_2}{\partial p_2} & \cdots & \frac{\partial x_2}{\partial p_m} \\ \vdots & \vdots & \ddots & \vdots \\ \frac{\partial x_n}{\partial p_1} & \frac{\partial x_n}{\partial p_2} & \cdots & \frac{\partial x_n}{\partial p_m} \end{bmatrix}. \tag{4.15}$$

Finally, by including Equations 4.14 into Equation 4.13, the following expression is obtained for the derivative of the H_α:

$$\frac{\partial}{\partial \mathbf{p}} \widehat{H}_\alpha = \frac{-n_p \sum_{i=1}^{n_s} \left[e^2_{\mathcal{Z}}(\mathbf{z}_i)\right]^{(\frac{\gamma}{2}-1)} \sum_{j=1}^{n_p} 2(z_{ij} - \tilde{z}_{ij})(\mathbf{J}_T(\mathbf{x}_j))^T \nabla z_{ij}}{2 \sum_{i=1}^{n_s} \left[e^2_{\mathcal{Z}}(\mathbf{z}_i)\right]^{\frac{\gamma}{2}}} \tag{4.16}$$

It is important to highlight at this point, that Equation 4.13 is a completely general expression and can be used for any type of matching features. If $\mathbf{z}_i$ are concatenations of features in $\mathbb{R}^d$ for each time point j, Equation 4.14 turns into

$$\frac{\partial}{\partial p_m} e^2_{\mathcal{Z}}(\mathbf{z}_i) = \sum_{j=1}^{n_p} \sum_{k=1}^{d} 2(z_{ijk} - \tilde{z}_{ijk}) \nabla z_{ijk} \mathbf{J}^m_T(\mathbf{x}_j) \tag{4.17}$$

where ∇z_{ijk} represents the spatial gradient of the k^{th} feature coefficient at time j, and its computation depends on the feature definition.

By applying Equation 4.16 for computing derivatives, the time complexity is reduced to $O(n_s \, log \, n_s)$ as compared to the $O(n_s^2 \, log \, n_s)$ time complexity required for finite differences.

CHAPTER 5

Strain analysis in the acute myocardial infarction

Abstract - *In this chapter we have studied the relationship between strains, infarction location, and coronary occlusion in patients with acute myocardial infarction (AMI). Even when the strain in AMI has been extensively studied with bidimensional ultrasonography, its study with MRI is of great interest due to the relative advantages of this modality. In this chapter, we have estimated strains by applying the registration method described in Chapter 4 to tagged magnetic resonance (T-MRI) sequences. Strain values were subsequently correlated to the infarction location assessed from Delay Enhancement MRI (DE-MRI), and to regions at risk (low perfused) obtained from Cardiac Catheterization (CC). The strain in 7 patients with myocardial infarction was regionally compared with respect to a control group of 10 healthy subjects, and the observed differences were explained based on the information provided by DE-MRI and CC. As expected, infarcted regions presented lower strain values with respect to healthy subjects, but an interesting finding was the lower strain in regions at risk which suggests a potential use of strain as a predictor of myocardial infarction.*

Adapted from E. Oubel, G. Avegliano, M. Huguet, B. H. Bijnens, M. De Craene, A. O. Hero, and A. F. Frangi. Automatic strain analysis in myocardial infarction: comparison with delayed enhancement and cardiac catheterization. To be submitted.

5.1 Introduction

Magnetic Resonance Imaging (MRI) allows studying different aspects of the heart anatomy and function depending on the specific sequence applied. Thus, Cine (C-MRI), tagged (T-MRI), and delay-enhancement of Gadolinium (DE-MRI) MR provide the necessary and complementary information required to perform cardiac function analysis. In this context, T-MRI provides tagged images of the myocardium that allow estimating cardiac displacement fields and strains. A promising area of study with T-MRI are the mechanical effects and evolution over time of the acute myocardial infarction (AMI) [11], since an infarcted region permanently loses its ability to contract. From a mathematical point of view, the cardiac contraction can be modeled as a transformation that establishes a dense point correspondence over time. The strain values derived from this transformation should be low in infarcted regions since the displacement field is expected to be almost constant inside. Similarly, regions at risk should present an altered motion as a consequence of a reduced blood supply.

The strain in AMI has been extensively studied with bidimensional ultrasonography (2D-US) [109–114]. Even when the drawbacks of 2D modalities seemed to be solved with the availability of 3D-US scanners, the application of strain estimation methods developed for 3D-US [120] has been limited to global cardiac function assessment [121–125]. MRI is an alternative modality to 3D-US since it provides images with higher signal to noise ratio (SNR), there is no missing information due to acoustic window issues, and the strain estimation is more accurate as material points can be tracked over the cardiac cycle. Therefore, the study of strain in AMI by using MRI is of great interest despite the extensive research already performed with US modalities. However, the information found in the literature is limited. Geskin *et al.* [115] have applied T-MRI for quantifying the response to dobutamine in patients after AMI. This was measured by using the percent of radial shortening obtained by a 1-dimensional strain analysis. Korosoglou *et al.* [101] have used Strain-Encoded MRI (SE-MRI) to study the correlation between strain and infarction in patients with heart failure, but only the circumferential strain was analyzed. Garot *et al.* [116] have shown a correlation between SE-MRI and DE-MRI. Finally, Spottiswoode *et al.* [117] have proposed a method to recover cardiac motion from 2D DENSE images, and shown its consistency in two patients with AMI.

In this chapter we have applied the method described in Chapter 4 to study differences in strain between a group of patients with AMI, and a group of healthy subjects. We have applied a regional approach, by comparing the strain values over the affected regions as assessed by DE-MRI. Differently from other articles in the literature [101, 115–117], we have also analyzed strain values according to the occlusion of coronary arteries quantified by cardiac catheterization (CC). This analysis was motivated by findings of low strain values in healthy regions according to DE-MRI.

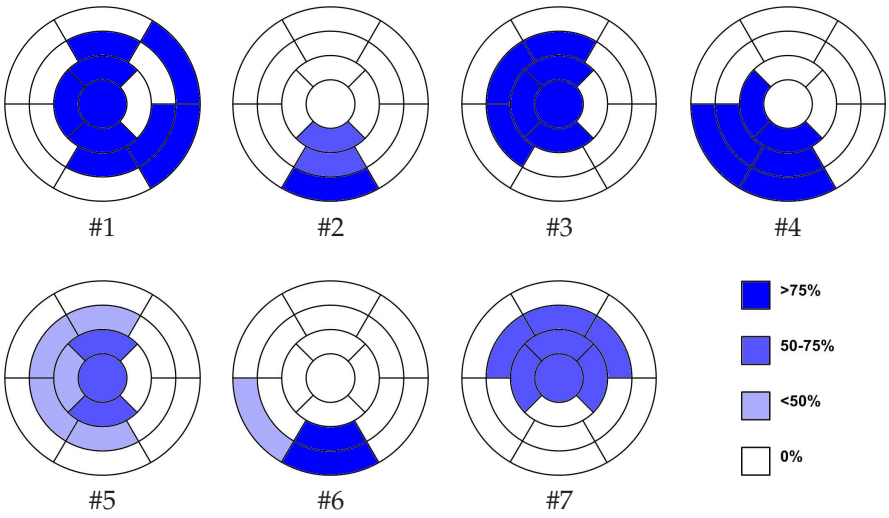

Figure 5.1: Transmurality of necrosis for then patient group classified into four categories: i) 0% (healthy segment) ii) <50%, iii) 50-75% and iv) > 75%.

5.2 Method

5.2.1 Study group

The database used for the experiments consisted of 10 healthy subjects (between 24 and 33 years old) and 7 patients with transmural infarction of the myocardium. For all subjects, C-MRI, T-MRI, and DE-MRI images were acquired in breath-hold by using a General Electric Signa CV/i, 1.5 T scanner (General Electric, Milwaukee, USA). Healthy volunteers were also imaged with DE-MRI to have a proof of their clinical status. The values of acquisition parameters were: slice thickness = 8mm, in-plane resolution = 0.78mm $\times$ 0.78mm, gap between slices = 0mm, TR=7.99ms, TE=4.43ms, flip angle = 20 degrees, and FOV=40cm$\times$40cm. C-MRI and T-MRI sequences were acquired at 30 phases per cardiac cycle. T-MRI images with a grid pattern of 5mm (tag spacing) were acquired by applying a Spatial Modulation of Magnetization (SPAMM) sequence. For each patient, an expert clinician assessed the presence of infarction from DE-MRI images, and classified the 16 standard segments [83] according to the transmurality of necrosis in the myocardium wall into 3 categories: a) < 50 %, b) 50-75 % and c) > 75 %. These measurements are presented as Bull's-eye plots in Figure 5.1. For infarcted patients, CC was also performed to assess the degree of coronary occlusion. Figure 5.2 presents the percent of coronary occlusion and the affected territories. Table 5.1 summarizes relevant clinical information for the patient group.

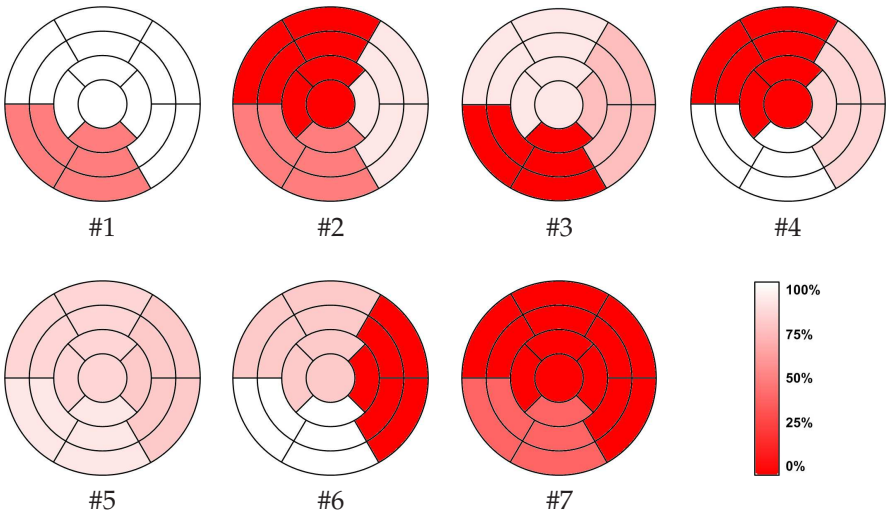

Figure 5.2: Maps of coronary occlusion assessed by cardiac catheterism according to the affected territories. Segments in red present a normal irrigation, and segments in white have a deficiency in irrigation due to complete occlusion of the associated coronary artery.

5.2.2 Strain estimation

The set of transformations $\mathcal{T}$ allows computing the displacement field $\mathbf{u}(\mathbf{x}, t)$ for a position $\mathbf{x}$ at ED and time t. Since the assumption of small deformations is too strong for cardiac deformations, the Green-Lagrange strain tensor must be used instead of the Green strain tensor. The Green-Lagrange strain tensor is defined as [90]

$$\mathbf{E} = \frac{1}{2}\left(\nabla\mathbf{u} + \nabla\mathbf{u}^T + \nabla\mathbf{u}^T\nabla\mathbf{u}\right) \tag{5.1}$$

Diagonal elements E_{ii} of $\mathbf{E}$ are normal strains, i.e. strains along each direction in a rectangular coordinate system. Given the geometry of the heart, this coordinate system is not appropriate for analysis. Instead, it is preferable the use of a local coordinate system composed by radial, circumferential, and longitudinal directions (rcl system) on the basis of the epicardial surface orientation at the reference (undeformed) geometry. In order to estimate the epicardial surface, we performed a manual segmentation of the SA image at ED and applied a variant [91] of the original marching cubes algorithm [92] to extract the epicardial and endocardial contours. The normal strain along a gin arbitrary direction $\mathbf{d}$ can be then obtained from the $\mathbf{E}$ as [93]:

Table 5.1: Relevant clinical information about each patient. EF = Ejection fraction from C-MRI studies; Dilated = Dilated LV evaluated by C-MRI studies; Y = Yes; N = No; LAD= Left anterior descending artery; CX = Circumflex coronary artery; RCA = Right coronary artery; Obst = Obstruction percentage of vessel.

Patient	**Gender**	**Age**	**EF**	**Dilated**	**Catheterism**		
					LAD	CX	RCA
#	*M/F*	*years*	*(%)*	*Y / N*		*(%) obst*	
1	M	59	23	Y	100	100	50
2	M	54	55	Y	0	90	50
3	M	70	40	N	90	75	0
4	M	71	52	N	0	85	100
5	M	53	34	Y	85	80	90
6	M	77	54	N	80	0	100
7	M	55	52	N	0	0	40

$$E_{dd} = \mathbf{d}^T \mathbf{E} \mathbf{d} \tag{5.2}$$

5.2.3 Strain analysis

Strain analysis along systole was performed by dividing the Left Ventricle (LV) into the 16 standard segments [83]. For a patient p, each segment was classified as "infarcted", "at risk", or "normal", depending on the information provided by DE-MRI and cardiac catheterization. We defined the *infarcted region* Ω^p_{inf} as the volume of myocardium composed by all segments marked as "infarcted". Similarly, the region at risk Ω^p_{risk} was defined as the volume of myocardium composed by all non-infarcted segments marked as "at risk". More exactly:

$$\Omega^p_{inf} = \bigcup_{i=1}^{16} S_i^p|_{L(S_i^p)=inf} \tag{5.3}$$

$$\Omega^p_{risk} = \bigcup_{i=1}^{16} S_i^p|_{L(S_i^p)=risk\,AND\,L(S_i^p)=inf} \tag{5.4}$$

where S_i^p is the i^{th} segment of patient p, and $L(S_i^p)$ is a function that assigns labels to each segment.

For each patient, we computed peak systolic strain values over regions Ω^p_{inf} and Ω^p_{risk} along radial (E_{rr}^{inf}, E_{rr}^{risk}), circumferential (E_{cc}^{inf}, E_{cc}^{risk}), and longitudinal directions (E_{ll}^{inf}, E_{ll}^{risk}). These values were subsequently compared to the peak systolic strain values of healthy subjects *for the same regions*, represented by their average value ($\overline{E}_{rr}^{norm}$, $\overline{E}_{cc}^{norm}$, $\overline{E}_{ll}^{norm}$).

Table 5.2: Means ($\overline{E}_{rr}$, $\overline{E}_{cc}$, $\overline{E}_{ll}$) and standard deviations (σ_{rr}, σ_{cc}, σ_{ll}) of peak systolic strains for each standard segment in the control group.

Segment (#)	$\overline{E}_{rr}$ (σ_{rr}) (%)	$\overline{E}_{cc}$ (σ_{cc}) (%)	$\overline{E}_{ll}$ (σ_{ll}) (%)
1	27.3 ± 8.3	-7.2 ± 0.7	-4.6 ± 5.3
2	21.5 ± 9.9	-10.2 ± 1.4	$-6,9 \pm 1.7$
3	17.0 ± 6.8	-12.5 ± 3.4	-8.7 ± 1.8
4	25.7 ± 5.7	-12.3 ± 3.1	-3.7 ± 3.8
5	26.1 ± 8.9	-10.1 ± 3.1	-3.9 ± 3.6
6	20.0 ± 10.9	-9.4 ± 1.7	-9.9 ± 9.0
7	26.3 ± 7.8	-9.0 ± 1.8	-8.9 ± 4.1
8	15.4 ± 8.5	-11.1 ± 1.6	-8.6 ± 2.4
9	10.6 ± 6.4	-13.5 ± 3.0	-9.6 ± 1.5
10	19.2 ± 4.5	-14.2 ± 1.5	-10.7 ± 6.7
11	22.7 ± 7.1	-13.9 ± 2.1	-7.9 ± 2.7
12	15.7 ± 4.4	-11.3 ± 1.9	-8.5 ± 3.6
13	12.8 ± 5.4	-6.6 ± 3.5	-8.4 ± 1.7
14	10.5 ± 7.6	-8.3 ± 1.9	-12.3 ± 4.3
15	11.4 ± 5.1	-14.1 ± 2.1	-6.5 ± 3.8
16	14.7 ± 9.3	-12.4 ± 4.8	-7.6 ± 2.7

5.3 Results and discussion

Table 5.2 presents the peak systolic strain values for the healthy subjects. As can be observed, the strain sign is consistent with the current knowledge of heart physiology: during systole there is a thickening of the myocardium ($\varepsilon_{rr} > 0$), a circumferential shortening ($\varepsilon_{cc} < 0$), and a longitudinal shortening ($\varepsilon_{ll} < 0$) characterized by a displacement of the heart base towards the apex. Table 5.2 shows a remarkably lower variance of circumferential strain with respect to radial and longitudinal strains, in agreement with other results reported in the literature [98]. A plausible explanation can be found in the estimation of radial direction, which depends strongly on a good estimation of the local curvature of the heart wall along the z-axis. An accurate curvature estimation is quite difficult to achieve because of the low image resolution in the long axis. On the contrary, the circumferential direction is tangent to the segmentation of epicardium in the xy plane, where the image resolution is much higher (10 times in our case).

It is important to comment on the strain underestimation effects induced by blood magnetization. At the beginning of image acquisition, the blood is magnetized and presents a tag pattern as all tissues in the image. This tag pattern disappears 60 ms later approximately as a consequence of blood mixing. The missing information creates a problem for image registration methods, since a point correspondence cannot be established between images. To solve this problem, we removed the first phase of the sequence to improve the registration accuracy. However, the suppression of the first phase produces an underestimation of strain, since

Table 5.3: Means of peak systolic strains ($\overline{E}_{rr}$, $\overline{E}_{cc}$, $\overline{E}_{ll}$) over infarcted (Ω_{inf}) and *at risk* (Ω_{risk}) regions for each patient. Values between brackets are the mean of peak systolic strains for the same region in the control group.

	Ω_{inf}			Ω_{risk}		
Patient	$\overline{E}_{rr}$ (σ_{rr}) (%)	$\overline{E}_{cc}$ (σ_{cc}) (%)	$\overline{E}_{ll}$ (σ_{ll}) (%)	$\overline{E}_{rr}$ (σ_{rr}) (%)	$\overline{E}_{cc}$ (σ_{cc}) (%)	$\overline{E}_{ll}$ (σ_{ll}) (%)
1	5.1 (14.5)	-0.8 (-9.7)	-0.2 (-4.4)	-	-	-
2	7.5 (13.1)	-5.3 (-9.8)	**-7.2 (-4.3)**	11.2 (-19.7)	**-10.8 (-10.1)**	**-8.3 (-4.2)**
3	11.5 (12.0)	-6.4 (-10.1)	-1.0 (-5.4)	17.6 (-19.7)	-2.8 (-10.1)	-2.7 (-4.2)
4	3.1 (9.4)	-7.7 (-10.4)	-2.2 (-5.4)	9.9 (-19.7)	-0.9 (-10.1)	0.4 (-4.2)
5	7.0 (11.2)	-2.0 (-10.8)	-2.3 (-5.8)	-	-	-
6	13.2 (13.3)	-4.4 (-9.6)	0.9 (-3.9)	12.4 (-16.4)	-5.1 (-8.4)	-5.7 (-3.5)
7	7.4 (10.2)	-5.7 (-10.2)	4.4 (-5.7)	-	-	-

the first considered phase corresponds to the heart in an already deformed state.

Table 5.3 shows the peak systolic values for the patient group compared to the control values. Except for an increased longitudinal strain for patient #2, the strain in infarcted regions was below the controls. The same trend was found for regions at risk. The same table also shows that the longitudinal strain presents the lowest correlation with presence on infarction and coronary occlusion. This can be explained from an image acquisition point of view. Standard cardiac MRI acquisition protocols use the same interslice spacing in the base-apex direction for the SA acquisition, than in the lateral direction for LA. Given the LV shape, this results in a lower number of LA images (and therefore less information) with respect to SA. The differential information provided by both views is in fact higher, since there is a difference (in favor of SA) in the cross sectional area of the myocardium and the out-of-plane motion is larger for LA.

In this chapter we have classified categorically each segment as infarcted if an infarction was present in at least one slice, and regardless its degree of transmurality. However, if the extention of the infarction is small, the segment could remain functional and there could be a disagreement between between strain values and the segment classification. The strain analysis could be improved by segmenting the scar to restrict the region of interest to the volume of myocardium affected by the infarction.

It is important to comment on the age mismatch between patient and control groups, since the found differences could be attributed to normal age-related changes of strain values. Unfortunately, we have not found in the literature a full description of such changes in the LV. Only partial aspects of aging have been reported like changes in torsion [126–129], and relaxation patterns [130]. However, the large deviations from normality shown in Table 5.3 are difficult to explain based on possible age-related effects. Another argument against this hypothesis is provided

by Oxenham *et al.* [129], who reported an increase in the circumferential strain with age, whereas we have observed a lower circumferential strain with respect to controls (the younger group).

5.4 Conclusions

In this paper we have applied a novel cardiac motion estimation method to study the interrelationships between strain, infarction, and coronary occlusion. The method provided consistent results with respect to the current knowledge about physio, and physiopathology of the heart. The recovered strains for healthy subjects were in agreement with the basic modes of contraction of the LV during systole, i. e. radial contraction (traduced in a wall thickening), and circumferential and longitudinal shortening. The estimated strains inside infarcted regions were lower than the average for healthy subjects in corresponding regions. The low intersubject variability of circumferential strain with respect to radial and longitudinal strains makes it the more appropriate to perform comparisons between healthy and pathological subjects. Another interesting finding was the reduced strains in regions at risk, which suggests a potential use of strain as a marker of regions with high risk of infarction and as follow up method after coronary stenting. Even when the applied methodology of strain analysis provided satisfactory results, it could benefit from improvements in each step. Examples are artifact correction in T-MRI, improvements in the estimation of the rcl coordinate system, and the addition of scar segmentation methods to constrain the region of analysis.

Bibliography

[1] D. Perperidis, R. H. Mohiaddin, and D. Rueckert, "Spatio-temporal free-form registration of cardiac MR image sequences," *Medical Image Analysis*, vol. 9, no. 5, pp. 441–56, October 2005.

[2] L. Axel and L. Dougherty, "MR imaging of motion with spatial modulation of magnetization," *Radiology*, vol. 171, no. 3, pp. 841–5, 1989.

[3] E. Zerhouni, D. Parish, and W. Rogers, "Human heart: tagging with MR imaging - A method for non invasive assessment of myocardial motion," *Radiology*, vol. 169, no. 1, pp. 59–63, 1988.

[4] F. B. Meyer, J. Huston III, and S. S. Riederer, "Pulsatile increases in aneurysm size determined by cine phase-contrast MR angiography," *Journal of Neurosurgery*, vol. 78, no. 6, pp. 879–83, June 1993.

[5] J. Ueno, T. Matsuo, K. Sugiyama, and R. Okeda, "Mechanism underlying the prevention of aneurismal rupture by coil embolization," *Journal of Medical and Dental Sciences*, vol. 49, no. 4, pp. 135–41, December 2002.

[6] Y. Kato, M. Hayakawa, H. Sano, M. V. Sunil, S. Imizu, M. Yoneda, S. Watanabe, M. Abe, and T. Kanno, "Prediction of impending rupture in aneurysms using 4D-CTA: histopathological verification of a real-time minimally invasive tool in unruptured aneurysms," *Minimally Invasive Neurosurgery*, vol. 47, no. 3, pp. 131–5, June 2004.

[7] V. Yaghmai, M. Rohany, A. Shaibani, M. Huber, H. Soud, E. J. Russell, and M. T. Walker, "Pulsatility imaging of saccular aneurysm model by 64-slice CT with dynamic multiscan technique," *Journal of Vascular and Interventional Radiology*, vol. 18, no. 6, pp. 785–8, June 2007.

[8] C. Zhang, M. C. Villa-Uriol, M. De Craene, J. M. Pozo, and A. F. Frangi, "Time-resolved 3D rotational angiography reconstruction: towards cerebral aneurysm pulsatile analysis," in *International Journal of Computer Assisted Radiology and Surgery*, H. U. Lemke, K. Inamura, K. Doi, M. W. Vannier, and A. G. Farman, Eds., vol. 3. Barcelona, Spain: Springer, June 2008, pp. S44–S46.

[9] H. G. Boecher-Schwarz, K. Ringel, L. Kopacz, A. Heimann, and O. Kempski, "Ex vivo study of the physical effect of coils on pressure and flow dynamics in experimental aneurysms," *American Journal of Neuroradiology*, vol. 21, no. 8, pp. 1532–6, September 2000.

[10] J. M. Wardlaw, J. Cannon, P. F. Statham, and R. Price, "Does the size of intracranial aneurysms change with intracranial pressure? Observations based on color power transcranial Doppler ultrasound," *Journal of Neurosurgery*, vol. 88, no. 5, pp. 846–50, May 1998.

[11] L. Axel, A. Montillo, and D. Kim, "Tagged magnetic resonance imaging of the heart: A survey," *Medical Image Analysis*, vol. 9, no. 4, pp. 376–93, August 2005.

[12] R. Chandrashekara, R. H. Mohiaddin, and D. Rueckert, "Analysis of 3D myocardial motion in tagged MR images using non rigid image registration," *IEEE Transactions on Medical Imaging*, vol. 23, no. 10, pp. 1245–50, October 2004.

[13] N. Rougon, C. Petitjean, F. Prêteux, P. Cluzel, and P. Grenier, "A non-rigid registration approach for quantifying myocardial contraction in tagged MRI using generalized information measures," *Medical Image Analysis*, vol. 9, no. 4, pp. 353–75, August 2005.

[14] D. O. Wiebers, J. P. Whisnant, J. Huston III, I. Meissner, R. D. Brown Jr., D. G. Piepgras, G. S. Forbes, K. Thielen, D. Nichols, W. M. O'Fallon, J. Peacock, L. Jaeger, N. F. Kassell, G. L. Kongable-Beckman, and J. C. Torner, "International study of unruptured intracranial aneurysms investigators. unruptured intracranial aneurysms: Natural history, clinical outcome, and risks of surgical and endovascular treatment," *Lancet*, vol. 362, no. 9378, pp. 103–10, July 2003.

[15] F. Ishida, H. Ogawa, T. Simizu, T. Kojima, and W. Taki, "Visualizing the dynamics of cerebral aneurysms with four-dimensional computed tomographic angiography," *Neurosurgery*, vol. 57, no. 3, pp. 460–71, 2005.

[16] M. Hayakawa, K. Katada, H. Anno, S. Imizu, J. Hayashi, K. Irie, M. Negoro, Y. Kato, T. Kanno, and H. Sano, "CT angiography with electrocardiographically gated reconstruction for visualizing pulsation of intracranial aneurysms: Identification of aneurysmal protuberance presumably associated with wall thinning," *American Journal of Neuroradiology*, vol. 26, no. 6, pp. 1366–9, 2005.

[17] J. R. Cebral, M. A. Castro, S. Appanaboyina, C. Putman, D. Millan, and A. F. Frangi, "Efficient pipeline for image-based patient-specific analysis of cerebral aneurysm haemodynamics: Technique and sensitivity," *IEEE Transactions on Medical Imaging*, vol. 24, no. 4, pp. 457–67, 2005.

[18] T. M. Liou and S. N. Liou, "A review of in vitro studies of hemodynamic characteristics in terminal and lateral aneurysm models," *Proceedings of the National Science Council*, vol. 23, no. 4, pp. 133–48, October 1999.

[19] D. Rueckert, L. I. Sonoda, C. Hayes, D. L. G. Hill, M. O. Leach, and D. J. Hawkes, "Nonrigid registration using free-form deformations: Application to breast MR images," *IEEE Transactions on Medical Imaging*, vol. 18, no. 8, pp. 712–21, August 1999.

[20] C. Studholme, D. L. G. Hill, and D. J. Hawkes, "An overlap invariant entropy measure of 3D medical image alignment," *Pattern Recognition*, vol. 32, no. 1, pp. 71–86, January 1999.

[21] R. Löhner, "Automatic unstructured grid generators," *Finite Elements in Analysis and Design*, vol. 25, no. 1-2, pp. 111–34, March 1997.

[22] R. Löhner and C. Yang, "Improved ALE mesh velocities for moving bodies," *Communications in Numerical Methods in Engineering*, vol. 12, no. 10, pp. 599–608, 1996.

[23] M. Shojima, M. Oshima, K. Takagi, R. Torii, M. Hayakawa, K. Katada, A. Morita, and T. Kirino, "Magnitude and role of wall shear stress on cerebral aneurysm. Computational fluid dynamic study of 20 middle cerebral artery aneurysms," *Stroke*, vol. 35, no. 11, pp. 2500–5, November 2004.

[24] L. Dempere, E. Oubel, M. A. Castro, C. M. Putman, A. F. Frangi, and J. R. Cebral, "CFD analysis incorporating the influence of wall motion: Application to intracranial aneurysms," in *8th International Conference on Medical Image Computing and Computer-Assisted Intervention, MICCAI 2006*, ser. Lecture Notes in Computer Science, R. Larsen, M. Nielsen, and J. Sporring, Eds., vol. 4190. Copenhagen, Denmark: Springer, October 2006, pp. 438–45.

[25] P. R. Hoskins, J. Prattis, and J. Wardlaw, "A flow model of cerebral aneurysms for use with power Doppler studies," *British Journal of Radiology*, vol. 71, no. 841, pp. 76–80, January 1998.

[26] R. Manzke, M. Grass, T. Nielsen, G. Shechter, and D. Hawkes, "Adaptive temporal resolution optimization in helical cardiac cone beam CT reconstruction," *Medical Physics*, vol. 30, no. 12, pp. 3072–80, December 2003.

[27] M. Matsumoto, T. Sasaki, K. Suzuki, J. Sakuma, Y. Endo, and K. Kodama, "Visualizing the dynamics of cerebral aneurysms with four-dimensional computed tomographic angiography," *Neurosurgery*, vol. 58, no. 5, p. E1003, May 2006.

[28] E. Oubel, M. De Craene, C. M. Putman, J. R. Cebral, and A. F. Frangi, "Analysis of intracranial aneurysm wall motion and its effects on hemodynamic patterns," in *SPIE Medical Imaging 2007: Physiology, Function, and Structure from Medical Images*, A. Manduca and X. Hu, Eds., vol. 6511. San Diego, CA, USA: SPIE press, February 2007, pp. 10–11.

[29] J. P. Thirion, "Image matching as a diffusion process: an analogy with Maxwell's demons," *Medical Image Analysis*, vol. 2, no. 3, pp. 243–60, September 1998.

[30] J. Weickert, A. Bruhn, T. Brox, and N. Papenberg, *Mathematical Models for Registration and Applications to Medical Imaging*, ser. Mathematics in Industry. Springer, 2006, vol. 10, ch. A Survey on Variational Optic Flow Methods for Small Displacements, pp. 103–36.

[31] S. Balter, D. Ergun, E. Tscholl, F. Buchmann, and L. Verhoeven, "Digital substraction angiography: Fundamental characteristics," *Radiology*, vol. 152, no. 1, pp. 195–8, July 1984.

[32] S. Lee, G. Wolberg, K.-W. Chwa, and S. Y. Shin, "Image metamorphosis with scattered feature constraints," *IEEE Transactions on Visualization and Computer Graphics*, vol. 2, no. 4, pp. 337–54, December 1996.

[33] S. Lee, G. Wolberg, and S. Y. Shin, "Scattered data interpolation with multilevel B-splines," *IEEE Transactions on Visualization and Computer Graphics*, vol. 3, no. 3, pp. 228–44, July-September 1997.

[34] A. Collignon, F. Maes, D. Delaere, D. Vandermeulen, P. Suetens, and G. Marchal, "Automated multi-modality image registration based on information theory," ser. Lecture Notes in Computer Science, Y. Bizais, C. Barillot, and R. Di Paola, Eds. Ile de Berder, France: Kluwer Academic, June 1995, pp. 263–74.

[35] P. Viola and W. M. Wells, "Alignment by maximization of mutual information," in *Fifth International Conference on Computer Vision*, E. Grimson, S. Shafer, A. Blake, and K. Sugihara, Eds., Los Alamitos, CA, USA, June 1995, pp. 16–23.

[36] T. M. Cover and J. A. Thomas, *Elements of information theory*. Wiley-Interscience, 1991.

[37] P. Gaetani, F. Tartara, V. Grazioli, F. Tancioni, L. Infuso, and R. Rodriguez y Baena, "Collagen cross-linkage, elastolytic and collagenolytic activities in cerebral aneurysms: a preliminary investigation," *Life Sciences*, vol. 63, no. 4, pp. 285–92, June 1998.

[38] L. de Figueiredo Borges, R. G. Jaldin, R. R. Dias, N. A. Stolf, J. B. Michel, and P. S. Gutierrez, "Collagen is reduced and disrupted in human aneurysms and dissections of ascending aorta," *Human pathology*, vol. 39, no. 3, pp. 437–43, March 2008.

[39] S. Goodall, M. Crowther, P. R. Bell, and M. M. Thompson, "The association between venous structural alterations and biomechanical weakness in patients with abdominal aortic aneurysms." *Journal of vascular surgery*, vol. 35, no. 5, pp. 937–42, May 2002.

[40] B. J. Rajesh, S. Sandhyamani, and R. N. Bhattacharya, "Clinico-pathological study of cerebral aneurysms," *Neurology India*, vol. 52, no. 1, pp. 82–6, March 2004.

[41] A. I. Holodny, M. Deck, and C. K. Petito, "Induction and subsequent rupture of aneurysms of the circle of willis after radiation therapy in Ehlers-Danlos syndrome: a plausible hypothesis," *American Journal of Neuroradiology*, vol. 17, no. 2, pp. 226–32, February 1996.

[42] T. Mizutani and H. Kojima, "Clinicopathological features of non-atherosclerotic cerebral arterial trunk aneurysms," *Neuropathology*, vol. 20, no. 1, pp. 91–7, March 2000.

[43] J. R. Landis and G. G. Koch, "The measurement of observer agreement for cathegorical data," *Biometrics*, vol. 33, no. 1, pp. 159–74, March 1977.

[44] A. V. Oppenheim and R. W. Schafer, *Digital Signal Processing*. Prentice Hall, 1999.

[45] J. Alastruey, K. Parker, J. Peiró, S. Byrd, and S. Sherwin, "Modelling the circle of Willis to assess the effects of anatomical variations and occlusions on cerebral flows," *Journal of Biomechanics*, vol. 40, no. 8, pp. 1794–805, October 2007.

[46] A. C. Guyton and J. E. Hall, *Textbook of Medical Physiology*. Elsevier, 2006.

[47] R. P. Franke, R. Fuhrmann, B. Hiebl, and F. Jung, "Influence of various radiographic contrast media on the buckling of endothelial cells," *Microvascular research*, vol. 76, no. 2, pp. 110–3, August 2008.

[48] S. K. Sharma, "Iodinated contrast media and contrast-induced nephropathy: Is there a preferred cost-effective agent?" *The journal of invasive cardiology*, vol. 20, no. 5, pp. 245–8, May 2008.

[49] S. Periaswamy and H. Faridb, "Medical image registration with partial data," *Medical Image Analysis*, vol. 10, no. 3, pp. 452–64, June 2006.

[50] J. Prince and E. McVeigh, "Motion estimation from tagged MR image sequences," *IEEE Transactions on Medical Imaging*, vol. 11, no. 2, pp. 238–49, June 1992.

[51] S. N. Gupta and J. L. Prince, "On variable brightness optical flow for tagged MRI," ser. Lecture Notes in Computer Science, Y. Bizais, C. Barillot, and R. Di Paola, Eds. Ile de Berder, France: Kluwer Academic, June 1995, pp. 323–34.

[52] L. Dougherty, J. C. Asmuth, A. S. Blom, L. Axel, and R. Kumar, "Validation of an optical flow method for tag displacement estimation," *IEEE Transactions on Medical Imaging*, vol. 18, no. 4, pp. 359–63, April 1999.

[53] J. L. Prince, S. N. Gupta, and N. F. Osman, "Bandpass optical flow for tagged MRI," *Medical physics*, vol. 27, no. 1, pp. 108–18, January 2000.

[54] N. F. Osman, W. S. Kerwin, E. R. McVeigh, and J. L. Prince, "Cardiac motion tracking using cine harmonic phase (HARP) magnetic resonance imaging," *Magnetic Resonance in Medicine*, vol. 42, no. 6, pp. 1048–60, 1999.

[55] N. F. Osman, E. R. McVeigh, and J. L. Prince, "Imaging heart motion using harmonic phase MRI," *IEEE Transactions on Medical Imaging*, vol. 19, no. 3, pp. 186–202, March 2000.

[56] L. Pan, J. L. Prince, J. A. Lima, and N. F. Osman, "Fast tracking of cardiac motion using 3D-HARP," *IEEE Transactions on Biomedical Engineering*, vol. 5, no. 8, pp. 1425–35, August 2005.

[57] W. G. O'Dell, C. C. Moore, W. C. Hunter, E. A. Zerhouni, and E. R. McVeigh, "Three-dimensional myocardial deformations: calculation with displacement field fitting to tagged MR images," *Radiology*, vol. 195, no. 3, pp. 829–35, June 1995.

[58] T. R. Denney and J. L. Prince, "Reconstruction of 3-D left ventricular motion from planar tagged cardiac MR images: an estimation theoretic approach," *IEEE Transactions on Medical Imaging*, vol. 14, no. 4, pp. 625–35, 1995.

[59] J. Declerck, J. Feldmar, and N. Ayache, "Definition of a four-dimensional continuous planispheric transformation for the tracking and the analysis of left-ventricle motion," *Medical Image Analysis*, vol. 2, no. 2, pp. 197–213, June 1998.

[60] C. Ozturk and E. R. McVeigh, "Four-dimensional B-spline based motion analysis of tagged MR images: introduction and in vivo validation." *Physics in medicine and biology*, vol. 45, no. 6, pp. 1683–702, June 2000.

[61] D. Rueckert, M. J. Clarkson, D. L. G. Hill, and D. J. Hawkes, "Non-rigid registration using higher-order mutual information," in *SPIE Medical Imaging 2000: Image Processing*, vol. 3979, no. 2. San Diego, CA, USA: SPIE press, February 2000, pp. 438–47.

[62] J. P. W. Pluim, J. B. A. Maintz, and M. A. Viergever, "Image registration by maximization of combined mutual information and gradient information," *IEEE Transactions on Medical Imaging*, vol. 19, no. 8, pp. 809–14, 2000.

[63] D. B. Russakoff, C. Tomasi, T. Rohlfing, and C. R. Maurer, "Image similarity using mutual information of regions," in *Computer Vision - ECCV 2004*, ser. Lecture Notes in Computer Science, T. Pajdla and J. Matas, Eds., vol. 3023. Prague, Czech Republic: Springer, May 2004, pp. 596–607.

[64] E. Oubel, C. Tobon-Gomez, A. Hero, and A. Frangi, "Myocardial motion estimation in tagged MR sequences by using aMI-based non rigid registration," in *Proc. of 8th International Conference on Medical Image Computing and Computer-Assisted Intervention (MICCAI'05), Part I*, ser. LNCS, J. S. Duncan and G. Gerig, Eds., vol. 3750. Palm Springs, CA: Springer, October 2005, pp. 271–8.

[65] N. Kingsbury, "The dual-tree complex wavelet transform: a new technique for shift invariance and directional filters," in *Proc. 8th IEEE DSP Workshop*, August 1998.

[66] ——, "Image processing with complex wavelets," *Philosophical transactions of the royal society*, vol. 357, pp. 2543–2560, 1999.

[67] J. Magarey and K. N., "Motion estimation using a complex-valued wavelet transform," *IEEE Transactions on Signal Processing*, vol. 46, no. 4, pp. 1069–84, April 1998.

[68] H. F. Neemuchwala and A. O. Hero, *Multi-sensor image fusion and its applications*. Marcel-Dekker, 2005, ch. Entropic graphs for registration, pp. 185–235.

[69] J. A. Schnabel, D. Rueckert, M. Quist, J. M. Blackall, A. D. Castellano-Smith, T. Hartkens, G. P. Penney, W. A. Hall, H. Liu, C. L. Truwit, F. A. Gerritsen, D. L. G. Hill, and D. J. Hawkes, "A generic framework for nonrigid registration based on non uniform multi-level free-form deformations," in *Medical Image Computing and Computer-Assisted Intervention*, ser. Lecture Notes in Computer Science, W. J. Niessen and M. A. Viergever, Eds. Utrecht, The Netherlands: Springer, October 2001, pp. 573–581.

[70] H. Neemuchwala, A. O. Hero, P. L. Carson, and C. Meyer, "Local feature matching using entropic graphs," in *Proc. IEEE Internat. Symposium on Biomedical Imaging: From Nano to Macro 2004 (ISBI'04)*. Arlington, VA: IEEE, April 2004, pp. 704–7.

[71] S. G. Mallat, "A theory for multiresolution signal decomposition: the wavelet representation," *IEEE Transactions on Pattern Analysis and Machine Intelligence*, vol. 11, no. 7, pp. 674–93, 1989.

[72] H. Neemuchwala, A. O. Hero, S. Zabuawala, and P. Carson, "Image registration methods in high-dimensional space," *International Journal of Imaging Systems and Technology*, vol. 16, no. 5, pp. 130–45, 2007.

[73] V. M. Pai and L. Axel, "Advances in MRI tagging techniques for determining regional myocardial strain," *Current Cardiology Reports*, vol. 8, no. 1, pp. 53–8, February 2006.

[74] P. Radeva, A. Amini, and J. Huang, "Deformable B-solids and implicit snakes for 3D localization and tracking of SPAMM MRI data," *Compututer Vision and Image Understanding*, vol. 66, no. 2, pp. 163–78, May 1997.

[75] C. Petitjean, N. Rougon, F. Prêteux, P. Cluzel, and P. Grenier, "Measuring myocardial deformations from MR data using information-theoretic non rigid registration," in *Functional Imaging and Modeling of the Heart, Second International Workshop*, ser. Lecture Notes in Computer Science, I. E. Magnin, J. Montagnat, P. Clarysse, J. Nenonen, and T. Katila, Eds., vol. 2674. Lyon, France: Springer, June 2003, pp. 162–72.

[76] R. Chandrashekara, R. H. Mohiaddin, and D. Rueckert, "Cardiac motion tracking in tagged MR images using a 4D B-spline motion model and nonrigid image registration," in *IEEE International Symposium on Biomedical Imaging: From Nano to Macro, ISBI 2004*. Arlington, VA, USA: IEEE, April 2004, pp. 468–71.

[77] M. J. Ledesma-Carbayo, J. Kybic, M. Desco, A. Santos, M. Suhling, P. Hunziker, and M. Unser, "Spatio-temporal nonrigid registration for ultrasound cardiac motion estimation," *IEEE Transactions on Medical Imaging*, vol. 24, no. 9, pp. 1113–26, September 2005.

[78] D. Shen, H. Sundar, Z. Xue, Y. Fan, and H. Litt, "Consistent estimation of cardiac motion by 4D image registration," in *Medical Image Computing and Computer-Assisted Intervention – MICCAI 2005, 8th International Conference, Part II*, ser. Lecture Notes in Computer Science, J. S. Duncan and G. Gerig, Eds., vol. 3750. Palm Springs, CA, USA: Springer, October 2005, pp. 902–10.

[79] D. Shen and C. Davatzikos, "HAMMER: Hierarchical attribute matching mechanism for elastic registration," *IEEE Transactions on Medical Imaging*, vol. 21, no. 11, pp. 1421–39, November 2002.

[80] R. E. Bellman, *Dynamic programming*. Mineola, N.Y.: Dover Publications, 2003.

[81] B. Ma, R. Narayanan, H. Park, A. O. Hero, P. H. Bland, and C. R. Meyer, "Comparing pairwise and simultaneous joint registrations of decorrelating interval exams using entropic graphs," in *Information Processing in Medical Imaging, 20th International Conference, IPMI 2007*, ser. Lecture Notes in Computer Science, N. Karssemeijer and B. P. F. Lelieveldt, Eds., vol. 4584. Kerkrade, The Netherlands: Springer, July 2007, pp. 270–82.

[82] N. Leonenko, L. Pronzato, and V. Savani, "A class of Rényi information estimators for multidimensional densities," *Annals of Statistics*, vol. 36, no. 5, pp. 2153–82, October 2008.

[83] M. D. Cerqueira, N. J. Weissman, V. Dilsizian, A. K. Jacobs, S. Kaul, W. K. Laskey, D. J. Pennell, J. A. Rumberger, T. Ryan, and M. S. Verani, "Standardized myocardial segmentation and nomenclature for tomographic imaging of the heart: a statement for healthcare professionals from the cardiac imaging committee of the council on clinical cardiology of the American Heart Association," *Circulation*, vol. 105, no. 4, pp. 539–42, January 2002.

[84] G. R. Sutherland, L. Hatle, P. Claus, J. D'hooge, and B. H. Bijnens, Eds., *Doppler Myocardial Imaging*, 1st ed. BSWK, 2006.

[85] E. G. Learned-Miller, "Data driven image models through continuous joint alignment," *IEEE Trans. Pattern Anal. Machine Intell.*, vol. 28, no. 2, pp. 236–50, February 2006.

[86] J. Ashburner, "A fast diffeomorphic image registration algorithm," *NeuroImage*, vol. 38, no. 1, pp. 95–113, 2007.

[87] B. D. Ripley, *Pattern Recognition and Neural Networks*. Cambridge University Press, January 1996.

[88] A. Rényi, "On measures of entropy and information," in *Proceedings of the Fourth Berkeley Symposium on Mathematical Statistics and Probability*, J. Neyman, Ed., vol. 1. Berkeley, CA, USA: University of California Press, June-July 1961, pp. 547 – 61.

[89] D. M. Mount, *ANN programming manual*, Department of Computer Science and Institute for Advanced Computer Studies, University of Maryland, College Park, Maryland, August 2006.

[90] T. Belytschko, W. Liu, and B. Moran, *Nonlinear Finite Elements for Continua and Structures*. England: John Wiley & Sons, 2001.

[91] W. Schroeder, K. Martin, and B. Lorensen, *The Visualization Toolkit, An Object Oriented Approach to 3D Graphics*. Kitware Inc, 1998.

[92] W. Lorensen and H. Cline, "Marching cubes A high resolution 3D surface construction algorithm," *Computer Graphics*, vol. 4, no. 21, pp. 163–9, July 1987.

[93] Y. P. Wang, Y. Chen, and A. A. Amini, "Fast LV motion estimation using subspace approximation techniques," *IEEE Transactions on Medical Imaging*, vol. 20, no. 6, pp. 499–513, June 2001.

[94] C. Rao, *Linear Statistical Inference and Its Applications, 2nd Edition*. Wiley, 2002.

[95] L. Ibanez, W. Schroeder, L. Ng, and J. Cates, "The ITK software guide," 2008, available at http://www.itk.org.

[96] D. Altman, *Practical Statistics for Medical Research*. Chapman & Hall, 1997.

[97] H. Lilliefors, "On the Komogorov-Smirnov test for normality with mean and variance unknown," *J Am Stat Assoc*, vol. 62, pp. 399–402, 1967.

[98] C. C. Moore, C. H. Lugo-Olivieri, E. R. McVeigh, and E. A. Zerhouni, "Three-dimensional systolic strain patterns in the normal human left ventricle: characterization with tagged MR imaging." *Radiology*, vol. 214, no. 2, pp. 453–66, February 2000.

[99] C. Petitjean, N. Rougon, F. Prêteux, P. Cluzel, and P. Grenier, "Quantification of myocardial function using tagged MR and cine MR images," *International Journal of Cardiovascular Imaging*, vol. 20, no. 6, pp. 497–507, December 2004.

[100] A. Bistoquet, J. Oshinski, and O. Škrinjar, "Myocardial deformation recovery from cine MRI using a nearly incompressible biventricular model," *Medical Image Analysis*, vol. 12, no. 1, pp. 69–85, February 2008.

[101] G. Korosoglou, A. A. Youssef, K. C. Bilchick, E. Ibrahim, A. C. Lardo, S. Lai, and N. F. Osman, "Real-time fast strain-encoded magnetic resonance imaging to evaluate regional myocardial function at 3.0 Tesla: Comparison to conventional tagging." *Journal of Magnetic Resonance Imaging*, vol. 27, no. 5, pp. 1012–8, May 2008.

[102] A. K. Rutz, S. Ryf, S. Plein, P. Boesiger, and S. Kozerke, "Accelerated whole-heart 3D CSPAMM for myocardial motion quantification," *Magnetic Resonance in Medicine*, vol. 59, no. 4, pp. 755–63, April 2008.

[103] G. Sharp, S. W. Lee, and D. K. Wehe, "Maximum-likelihood registration of range images with missing data," *IEEE Trans. Pattern Anal. Machine Intell.*, vol. 30, no. 1, pp. 120–30, January 2008.

[104] S. E. Fischer, G. C. McKinnon, S. E. Maier, and P. Boesiger, "Improved myocardial tagging contrast," *Magnetic Resonance in Medicine*, vol. 30, no. 2, pp. 191–200, August 1993.

[105] D. Kim, C. M. Bove, C. M. Kramer, and F. H. Epstein, "Importance of k-space trajectory in echo-planar myocardial tagging at rest and during dobutamine stress," *Magnetic Resonance in Medicine*, vol. 50, no. 4, pp. 813–20, October 2003.

[106] J. Lötjönen, M. Pollari, S. Kivistö, and K. Lauerma, "Correction of movement artifacts from 4D cardiac short and long-axis MR data," in *Medical Image Computing and Computer-Assisted Intervention – MICCAI 2004, 7th International Conference, Part II*, ser. Lecture Notes in Computer Science, C. Barillot, D. R. Haynor, and P. Hellier, Eds., vol. 3217. Saint-Malo, France: Springer, September 2004, pp. 405–12.

[107] A. G. Chandler, R. J. Pinder, T. Netsch, J. A. Schnabel, D. J. Hawkes, D. L. G. Hill, and R. Razavi, "Correction of misaligned slices in multi-slice MR cardiac examinations by using slice-to-volume registration," in *Third IEEE International Symposium on Biomedical Imaging: From Nano to Macro, ISBI 2006*. Arlington, VA: IEEE, April 2006, pp. 474–7.

[108] Z. Quian, R. Huang, D. Metaxas, and L. Axel, "A novel tag removal technique for tagged cardiac MRI and its applications," in *Fouth IEEE International Symposium on Biomedical Imaging: From Nano to Macro, ISBI 2007*. Washington, USA: IEEE, April 2007, pp. 364–7.

[109] R. Jurcut, C. J. Pappas, P. G. Masci, L. Herbots, M. Szulik, J. Bogaert, F. Van de Werf, W. Desmet, F. Rademakers, J. U. Voigt, and J. D'hooge, "Detection of regional myocardial dysfunction in patients with acute myocardial infarction using velocity vector imaging," *Journal of the American Society of Echocardiography*, vol. 21, no. 8, pp. 879–86, August 2008.

[110] V. Sachdev, A. H. Aletras, S. Padmanabhan, S. Sidenko, Y. N. Rao, C. L. Brenneman, Y. Shizukuda, G. R. Lie, P. S. Vincent, M. A. Waclawiw, and A. E. Arai, "Myocardial strain decreases with increasing transmurality of infarction: a Doppler echocardiographic and magnetic resonance correlation study," *Journal of the American Society of Echocardiography*, vol. 19, no. 1, pp. 34–9, January 2006.

[111] T. Vartdal, H. Brunvand, E. Pettersen, H. J. Smith, E. Lyseggen, T. Helle-Valle, H. Skulstad, H. Ihlen, and T. Edvardsen, "Early prediction of infarct size by strain Doppler echocardiography after coronary reperfusion," *Journal of the American College of Cardiology*, vol. 49, no. 16, pp. 1715–21, April 2007.

[112] J. Chan, L. Hanekom, C. Wong, R. Leano, G. Cho, and T. Marwick, "Differentiation of subendocardial and transmural infarction using two-dimensional strain rate imaging to assess short-axis and long-axis myocardial function," *Journal of the American College of Cardiology*, vol. 48, no. 10, pp. 2026–33, November 2006.

[113] Y. Zhang, A. K. Chan, C. M. Yu, G. W. Yip, J. W. Fung, W. W. Lam, N. M. So, M. Wang, E. B. Wu, J. T. Wong, and J. E. Sanderson, "Strain rate imaging differentiates transmural from non-transmural myocardial infarction: a validation study using delayed-enhancement magnetic resonance imaging," *Journal of the American College of Cardiology*, vol. 46, no. 5, pp. 864–71, September 2005.

[114] M. Becker, E. Bilke, H. Kühl, M. Katoh, R. Kramann, A. Franke, A. Bücker, P. Hanrath, and H. R., "Analysis of myocardial deformation based on pixel tracking in two dimensional echocardiographic images enables quantitative assessment of regional left ventricular function," *Heart*, vol. 92, no. 8, pp. 1102–8, August 2006.

[115] G. Geskin, C. M. Kramer, W. J. Rogers, T. M. Theobald, D. Pakstis, Y. L. Hu, and N. Reichek, "Quantitative assessment of myocardial viability after infarction by dobutamine magnetic resonance tagging," *Circulation*, vol. 98, no. 3, pp. 217–23, July 1998.

[116] J. Garot, J. A. Lima, B. L. Gerber, S. Sampath, K. C. Wu, D. A. Bluemke, J. L. Prince, and N. F. Osman, "Spatially resolved imaging of myocardial function with strain-encoded MR: comparison with delayed contrast-enhanced MR imaging after myocardial infarction." *Radiology*, vol. 233, no. 2, pp. 596–602, November 2004.

[117] B. S. Spottiswoode, X. Zhong, A. T. Hess, C. M. Kramer, E. M. Meintjes, B. M. Mayosi, and F. H. Epstein, "Tracking myocardial motion from cine DENSE images using spatiotemporal phase unwrapping and temporal fitting," *IEEE Transactions on Medical Imaging*, vol. 26, no. 1, pp. 15–30, January 2007.

[118] M. R. Sabuncu and P. J. Ramadge, "Gradient based optimization of an EMST image registration function," in *IEEE International Conference on Acoustics, Speech, and Signal Processing*, vol. 2, Philadelphia, PA, USA, March 2005, pp. 253–6.

[119] A. O. Hero, B. Ma, O. Michael, and J. Gorman, "Applications of entropic spanning graphs," *IEEE Signal Processing Mag.*, vol. 19, no. 5, pp. 85–95, September 2002.

[120] X. Papademetris, A. J. Sinusas, D. P. Dione, and J. S. Duncan, "Estimation of 3D left ventricular deformation from echocardiography," *Medical Image Analysis*, vol. 5, no. 1, pp. 17–28, March 2001.

[121] J. L. Hare, C. Jenkins, S. Nakatani, A. Ogawa, C. M. Yu, and T. H. Marwick, "Feasibility and clinical decision-making with 3D echocardiography in routine practice," *Heart*, vol. 94, no. 4, pp. 440–5, April 2008.

[122] J. Kjaergaard, C. L. Petersen, A. Kjaer, B. K. Schaadt, J. K. Oh, and C. Hassager, "Evaluation of right ventricular volume and function by 2D and 3D echocardiography compared to MRI," *European Journal of Echocardiography*, vol. 7, no. 6, pp. 430–8, December 2006.

[123] V. Mor-Avi, L. Sugeng, L. Weinert, P. MacEneaney, E. G. Caiani, R. Koch, I. S. Salgo, and R. M. Lang, "Fast measurement of left ventricular mass with real-time three-dimensional echocardiography: comparison with magnetic resonance imaging," *Circulation*, vol. 110, no. 13, pp. 1814–8, September 2004.

[124] H. F. Mannaerts, J. A. van der Heide, O. Kamp, M. G. Stoel, J. Twisk, and C. A. Visser, "Early identification of left ventricular remodelling after myocardial infarction, assessed by transthoracic 3D echocardiography," *European Heart Journal*, vol. 25, no. 8, pp. 680–7, April 2004.

[125] D. Mele, R. Teoli, C. Cittanti, G. Pasanisi, G. Guardigli, R. A. Levine, and R. Ferrari, "Assessment of left ventricular volume and function by integration of simplified 3D echocardiography, tissue harmonic imaging and automated extraction of endocardial borders," *International Journal of Cardiovascular Imaging*, vol. 20, no. 3, pp. 191–202, June 2004.

[126] T. T. Phan, G. N. Shivu, K. Abozguia, M. Gnanadevan, I. Ahmed, and M. Frenneaux, "Left ventricular torsion and strain patterns in heart failure with normal ejection fraction are similar to age-related changes." *European Journal of Echocardiography*, vol. 10, no. 6, pp. 793–800, August 2009.

[127] B. M. van Dalen, O. I. Soliman, W. B. Vletter, F. J. ten Cate, and M. L. Geleijnse, "Age-related changes in the biomechanics of left ventricular twist measured by speckle tracking echocardiography," *American Journal of Physiology. Heart and Circulatory Physiology*, vol. 295, no. 4, pp. H1705–11, October 2008.

[128] M. Takeuchi, H. Nakai, M. Kokumai, T. Nishikage, S. Otani, and R. M. Lang.

[129] H. C. Oxenham, A. A. Young, B. R. Cowan, T. L. Gentles, C. J. Occleshaw, C. G. Fonseca, R. N. Doughty, and N. Sharpe, "Age-related changes in myocardial relaxation using three-dimensional tagged magnetic resonance imaging," *Journal of Cardiovascular Magnetic Resonance*, vol. 5, no. 3, pp. 421–30, July 2003.

[130] C. G. Fonseca, H. C. Oxenham, B. R. Cowan, C. J. Occleshaw, and A. A. Young, "Aging alters patterns of regional nonuniformity in LV strain relaxation: a 3-D MR tissue tagging study," *American Journal of Physiology. Heart and Circulatory Physiology*, vol. 285, no. 2, pp. H621–30, August 2003.

[131] Y. Bizais, C. Barillot, and R. Di Paola, Eds., *Information Processing in Medical Imaging, 14th International Conference, IPMI 1995*, ser. Lecture Notes in Computer Science. Ile de Berder, France: Kluwer Academic, June 1995.

Publications

Journals

- D. C. Barber, **E. Oubel**, A. F. Frangi and D. R Hose, "Efficient computational fluid dynamics mesh generation by image registration", *Medical Image Analysis*, 11(6):648–62, December 2007.
- H. Ólafsdóttir, T. A. Darvann, N. V. Hermann, **E. Oubel**, B. K. Ersbøll, A. F. Frangi, P. Larsen, C. A. Perlyn, G. M. Morriss-Kay, and S. Kreiborg, "Computational Mouse Atlases and Their Application to Automatic Assessment of Craniofacial Dysmorphology Caused by the Crouzon Mutation Fgfr2Ĉ342Y". *Journal of Anatomy*, 211(1):37–52, July 2007.
- **E. Oubel**, M. De Craene, A. O. Hero, M. Huguet, G. Avegliano, B. H. Bijnens, and A. F. Frangi, "Cardiac Motion Estimation by Joint Alignment of tMRI sequences". Under review.
- **E. Oubel**, J. R. Cebral, M. De Craene, R. Blanc, J. Blasco, J. Macho, C. M. Putman, and A. F. Frangi, "Wall motion estimation in intracranial aneurysms from DSA sequences". Under review.
- D. Sforza, **E. Oubel**, M. De Craene, C. M. Putman, A. F. Frangi, and J. R. Cebral, "Characterization of cerebral aneurysm wall motion from dynamic angiography". Under review.
- H. Ólafsdóttir, S. Lanche, T. A. Darvann, N. V. Hermann, K. Sjöstrand, **E. Oubel**, A. F. Frangi, P. Larsen, C. A. Perlyn, D. G. Hove, J. Hukki, A. Kane, A., G. M. Morriss-Kay, S. Kreiborg, B. K. Ersbøll, and R. Larsen, "A volumetric quantification of asymmetry using non-rigid registration". Under review.
- **E. Oubel**, G. Avegliano, M. Huguet, M. De Craene, A. O. Hero, B. H. Bijnens, and A. F. Frangi, "Automatic Strain Analysis in Myocardial Infarction: Correlation with Delayed Enhancement and Cardiac Angiography". To be submitted.

Conferences

- **E. Oubel**, F. Rousseau, V. Noblet, M. Koob, J-P. Armspach, and J-L. Dietemann, "Evaluation of different strategies for distortion correction in fetal diffusion-weighted imaging". In C. Studholme and F. Rousseau, editors, *MICCAI'09 Image Analysis for the Developing Brain*, London, UK, September 2009.
- O. Camara, **E. Oubel**, G. Piella, S. Balocco, M. De Craene, A. F. Frangi, "Multi-sequence registration of cine, tagged and delay-enhancement MRI with shift correction and steerable pyramid-based detagging". In *Functional Imaging and Modeling of the Heart (FIMH'09)*, Nice, France, June 2009.
- G. Piella, M. De Craene, **E. Oubel**, I. Larrabide, M. Huguet, B. H. Bijnens and A. F. Frangi, "Myocardial deformation from tagged MRI in hypertrophic cardiomyopathy using an efficient registration strategy". In X. P. Hu and A. V. Clough, editors, *SPIE Medical Imaging 2009: Biomedical Applications in Molecular, Structural, and Functional Imaging*, volume 6511, San Diego, CA, USA, February 2009.
- H. Ólafsdóttir, S. Lanche, T. A. Darvann, N. V. Hermann, R. Larsen, B. K. Ersbøll, **E. Oubel**, A. F. Frangi, P. Larsen, C. A. Perlyn, G. M. Morriss-Kay, and S. Kreiborg, "A point-wise quantification of asymmetry using deformation fields: Application to the study of the Crouzon mouse model". In N. Ayache, S. Ourselin, and A. J. Maeder, editors, *10th International Conference on Medical Image Computing and Computer-Assisted Intervention (MICCAI'07)*, Lecture Notes in Computer Science, pages 452–59, Brisbane, Australia, October 2007. Springer.
- S. Ordás, **E. Oubel**, R. Sebastian, and A. F. Frangi, "Computational anatomy atlas of the heart". In *International Symposium on Image and Signal Processing and Analysis (ISPA'07)*, pages 338–42, Istanbul, Turkey, September 2007.
- H. Ólafsdóttir, M. S. Hansen, K. Sjöstrand, T. A. Darvann, N. V. Hermann, **E. Oubel**, B. K. Ersbøll, R. Larsen, A. F. Frangi, P. Larsen, C. A. Perlyn, G. M. Morriss-Kay, and S. Kreiborg, "Sparse statistical deformation model for the analysis of craniofacial malformation in the Crouzon mouse. In B. K. Ersbøll and K. S. Pedersen, editors, *Scandinavian Conference on Image Analysis 2007 (SCIA'07)*, volume 4522 of Lecture Notes In Computer Science, pages 112–21. Springer, June 2007.
- **E. Oubel**, M. De Craene, M. Gazzola, A. O. Hero, and A. F. Frangi. "Multiview registration of cardiac tagged MRI images". In M. Wernick and J. A. Fessler, editors, Fouth IEEE International Symposium on Biomedical Imaging: From Nano to Macro (ISBI'07), pages 388–91, Arlington, VA, USA, April 2007. IEEE.
- H. Ólafsdóttir, T. A. Darvann, N. V. Hermann, B. K. Ersbøll, **E. Oubel**, R. Larsen, A. F. Frangi, P. Larsen, C. A. Perlyn, G. M. Morriss-Kay, and S. Kreiborg, "Automatic detection of wild-type mouse cranial sutures". In *Image analysis and in-vivo pharmacology*, April 2007.
- M. S. Hansen, H. Olafsdóttir, T. A. Darvann, N. V. Hermann, **E. Oubel**, R. Larsen, B. K. Ersbøll, A. F. Frangi, P. Larsen, C. A. Perlyn, G. M. Morris-Kay, and S. Kreiborg, "Estimation of independent non-linear deformation modes for analysis of craniofacial malformations in crouzon mice". In M. Wernick and J. A. Fessler, editors, *Fouth IEEE*

International Symposium on Biomedical Imaging: From Nano to Macro (ISBI'07), Arlington, VA, USA, April 2007. IEEE.

- S. Ordás, **E. Oubel**, R. Leta, F. Carreras, and A. F. Frangi, "A statistical shape model of the heart and its application to model-based segmentation". In A. Manduca and X.P. Hu, editors, *SPIE Medical Imaging 2007: Physiology, Function, and Structure from Medical Images*, volume 6511, San Diego, CA, USA, February 2007. SPIE.

- H. Ólafsdóttir, T. A. Darvann, B. K. Ersbøll, N. V. Hermann, **E. Oubel**, R. Larsen, A. F. Frangi, P. Larsen, C. A. Perlyn, G. M. Morriss-Kay, and S. Kreiborg, "Craniofacial statistical deformation models of wild-type mice and Crouzon mice. In J. M. Reinhardt and J. P. W Pluim, editors, *SPIE Medical Imaging 2007: Image processing*, volume 6512, San Diego, CA, USA, February 2007. SPIE.

- **E. Oubel**, M. De Craene, C. M. Putman, J. R. Cebral, and A. F. Frangi, "Analysis of intracranial aneurysm wall motion and its effects on hemodynamic patterns". In A. Manduca and X.P. Hu, editors, *SPIE Medical Imaging 2007: Physiology, Function, and Structure from Medical Images*, volume 6511, San Diego, CA, USA, February 2007. SPIE.

- L. Dempere-Marco, **E. Oubel**, M. A. Castro, C. M. Putman, A. F. Frangi, and J. R. Cebral, "CFD analysis incorporating the influence of wall motion: Application to intracranial aneurysms", In R. Larsen, M. Nielsen, and J. Sporring, editors, *9th International Conference on Medical Image Computing and Computer-Assisted Intervention (MICCAI'06)*, Lecture Notes in Computer Science, pages 438–45, Copenhagen, Denmark, October 2006. Springer.

- H. Ólafsdóttir, **E. Oubel**, A. F. Frangi, T. A. Darvann, N. V. Hermann, S. Kreiborg, P. Larsen, B. K. Ersbøll, C. A. Perlyn, and G. Morriss-Kay, "Automatic assessment of global craniofacial differences between Crouzon mice and wild-type mice in terms of the cephalic index". In T. A. Darvann, N. V. Hermann, P. Larsen, and S. Kreiborg, editors, *MICCAI'06 Craniofacial Image Analysis for Biology, Clinical Genetics, Diagnostics and Treatment*, pages 49–57, Copenhagen, DK, October 2006.

- **E. Oubel**, A. F. Frangi, and A. O. Hero, "Complex wavelets for registration of tagged MRI sequences", In J. Kovačević and E. Meijering, editors, *Third IEEE International Symposium on Biomedical Imaging: From Nano to Macro (ISBI'06)*, Arlington, VA, USA, April 2006.

- **E. Oubel**, C. Tobon-Gomez, A. O. Hero, and A. F. Frangi, "Myocardial motion estimation in tagged MRI sequences by using αMI-based non rigid registration". In J. S. Duncan and G. Gerig, editors, *8th International Conference on Medical Image Computing and Computer-Assisted Intervention (MICCAI'05)*, volume 3750 of Lecture Notes in Computer Science, pages 271–8, Palm Springs, CA, USA, October 2005. Springer.

- **E. Oubel**, H. Neemuchwala, A. O. Hero, L. Boisrobert, M. Laclaustra, and A. F. Frangi, "Assessment of artery dilation by using image registration based on spatial features". In J. M. Fitzpatrick and J. M. Reinhardt, editors, *SPIE Medical Imaging 2005: Image Processing*, volume 5747, pages 1283–91, San Diego, CA, USA, February 2005. SPIE.

Abstracts

- **E. Oubel**, C. Tobon-Gomez, G. Avegliano, M. Huguet, M. De Craene, A. O. Hero , and A. F. Frangi, "Strain Analysis in Myocardial Infarction by Using Tagged MRI: Correlation with Delayed Enhancement and Perfusion". In *Computer Assisted Radiology and Surgery (CARS'08)*, Barcelona, Spain, June 2008.
- C. Tobon-Gomez, **E. Oubel**, C. Butakoff, M. Huguet, C. Moure, A. Panaro, F. Carreras, B. Bijnens y A.F. Frangi, "Herramienta de cuantificación de función cardaca a partir de estudios multimodales", In *XX Congreso de la Sociedad Catalana de Cardiología*, Barcelona, Spain, June 2008.
- M. Huguet, **E. Oubel**, C. Tobon-Gomez, C. Moure, G. Avegliano, M. de Craene, M. Petit, B. Bijnens, A. F. Frangi, "Utilidad de la resonancia magnética marcada para el análisis del strain radial en pacientes con infarto miocárdico". In *XX Congreso de la Sociedad Catalana de Cardiología*, Barcelona, Spain, June 2008.
- H. Ólafsdóttir, T. A. Darvann, **E. Oubel**, A. F. Frangi, N. V. Hermann, B. K. Ersbøll, and C. A. Perlyn, "Towards describing Crouzon syndrome via a craniofacial atlas". In *Den 15. Danske Konference i Mønstergenkendelse og Billedanalyse*, August 2006.

Resumen

La estimación de cambios morfológicos temporales de tejidos biológicos es un problema recurrente en imaginología. Los métodos de corregistro de imágenes resultan adecuados para resolver este tipo de problemas ya que permiten establecer una correspondencia punto a punto entre imágenes, la cual a su vez puede ser utilizada para cuantificar deformaciones. Dada una secuencia de imágenes $I(\mathbf{x}, t) = I(\mathbf{x}, 0), I(\mathbf{x}, 1) \cdots, I(\mathbf{x}, N-1)$, en el contexto de esta tesis, corregistrar una secuencia significa encontrar una transformación $\mathbf{T}(\mathbf{x}, t) : (\mathbf{x}, 0) \rightarrow (\mathbf{x}', t)$ que establece una correspondencia entre sus imágenes componentes. En esta tesis, nos hemos enfocado en dos aplicaciones de gran interés del corregistro de secuencias en imaginología: la estimación de movimiento de pared en aneurismas cerebrales, y la estimación de deformaciones cardíacas.

La cuantificación de la pulsación en aneurismas es importante para estudiar la conexión entre la hemodinámica y ruptura. Una de las hipótesis que intentan explicar la ruptura de aneurismas es la concentración de fuerzas sobre la pared vascular. Esta puede ser cuantificada calculando el esfuerzo de corte sobre la pared a partir de simulaciones computacionales de dinámica de fluidos (CFD). En este contexto, la información sobre el movimiento de pared puede utilizarse para imponer condiciones de frontera en simulaciones realizadas con modelos no rígidos, como se describe en el Capítulo 1.

La estimación de movimiento de pared es también de gran importancia debido a la posible conexión entre pulsación y riesgo de ruptura como se sugiere en [4–6]. La hipótesis subyacente es que la ruptura de un aneurisma se produce como consecuencia de la debilidad de la pared vascular, lo cual debería reflejarse en un cambio en la pulsación. Para estudiar la relación entre ruptura y pulsación es necesario entonces cuantificar esta última, lo cual puede realizarse midiendo los desplazamientos de la pared vascular a lo largo del ciclo cardíaco.

La mayoría de los valores de movimiento de pared que se encuentran en la literatura corresponden a experimentos realizados con fantomas [5,7], imágenes simuladas [8], o modelos experimentales [9]. Solo unos pocos intentos de cuantificación *in-vivo* han sido realizados en seres humanos [4, 10]. En esta tesis hemos desarrollado un método automático para cuantificar el movimiento de pared de aneurismas intracraneales a partir de secuencias de

angiografía digital. Este método fue luego aplicado para investigar la relación entre estado de ruptura y la pulsación (Capítulo 2).

En cuanto a los métodos de estimación de deformaciones cardíacas, estos son importantes para el estudio del corazón en condiciones normales, patológicas, y simuladas. Entre otras aplicaciones, estos métodos son útiles para estudiar los efectos mecánicos de ciertas cardiopatías [11], y para el desarrollo de modelos electromecánicos. El corregistro de imágenes basado en Información Mutua (MI) entre volúmenes componentes de secuencias de T-MRI ha probado ser una buena estrategia para estimar campos de desplazamiento en el corazón [12, 13]. Esto nos ha motivado a estudiar extensiones de los métodos basados en teoría de la información para incluir información espacial y temporal.

En general, las métricas de similaridad están basadas en la intensidad de la imagen, ignorando información espacial potencialmente relevante para guiar el proceso de corregistro. Para incluir esta información hemos explorado el uso de métricas basadas en transformadas wavelets para el corregistro no rígido de secuencias de T-MRI bidimensionales. Para incluir información temporal en el proceso de corregistro hemos realizado un corregistro conjunto de los volúmenes componentes de la secuencias, en lugar de una serie de corregistros entre pares de volúmenes (Capítulo 4). Esta nueva estrategia para la recuperación de campos de desplazamiento fue luego aplicada para estudiar diferencias regionales de deformación entre pacientes con infarto agudo de miocardio y un grupo control de sujetos sanos (Capítulo 5).

Los resultados de estas lineas de invesigación han sido presentados en diferentes conferencias, y enviados a revistas de divulgación científica para su publicación. La correspondiente lista de publicaciones se puede encontrar a continuación del Capítulo 5. En la misma lista se han agregado otras publicaciones fruto de colaboraciones realizadas con grupos externos, a las que hemos contribuido con la experiencia ganada durante estos años en el ámbito de corregistro de imágenes.

Conclusiones

Los capítulos que componen esta tesis tienen como denominador común el procesamiento de secuencia de imágenes, cada uno de ellos aborda problemáticas diferentes, mediante distintas metodologías, y con objetivos particulares. Por lo tanto, las conclusiones se presentan de manera independiente para cada uno de los capítulos.

Capitulo 1. Modelos distensibles para simulaciones computacionales de dinámica de fluidos en aneurismas intracraneales

En este estudio se ha presentado una nueva estrategia para incluir información de movimiento de pared en simulaciones CFD, para poder entender la influencia de paredes distensibles sobre los patrones de flujo sanguíneo dentro del aneurisma. Este nuevo método provee una base para simulaciones CFD potencialmente más exactas. Se ha mostrado además que es posible estimar el movimiento de pared en aneurismas aplicando técnicas de corregistro de imágenes a secuencias angiográficas, y que existen movimientos diferenciales en el aneurisma, en concordancia con la literatura [15, 16].

El método de estimación de movimiento de pared puede ser mejorado de diferentes maneras, tales como el uso mayores frecuencias de muestreo, el uso de catéteres de mayor dimension, y tasas de inyección de contraste mayores. El uso de frecuencias de muestreo más elevadas debería permitir recuperar la curva de distensión completa, lo cual eliminaría la necesidad de usar formas de onda particulares en las simulaciones. Una limitación potencial de la técnica presentada es que no se puede garantizar una distribución homogénea del contraste para las tasas de inyección y tamaños de catéter utilizados. Los avances en tecnología de adquisición de imágenes que permitan mayores resoluciones espaciales deberían incrementar la sensibilidad del método.

En cuanto a la influencia del movimiento de pared sobre la hemodinámica, se observaron pequeñas diferencias en la distribución de esfuerzos de corte obtenidas con modelos rígidos y distensibles, pero los modelos rígidos produjeron una sobreestimación de su magnitud.

Sin embargo, otras características hemodinámicas no exhibieron variaciones sustanciales (Ej: localización y tamaño de la zona de impacto). la fueron condición

Aunque se cree que el esfuerzo de corte juega un papel importante en la mecanobiología de la pared arterial, se requiere investigación adicional para determinar cuáles son las variables hemodinámicas relevantes, y el efecto del movimiento de pared sobre las mismas. Finalmente, aun cuando es generalmente aceptado que la pared del aneurisma es siempre distensible en cierto grado, el rango de variabilidad del movimiento de pared entre pacientes es aun desconocido. Se requieren estudios sobre un número mayor de casos para determinar las posibilidades de medición, y si las diferencias en distensibilidad pueden ser relacionadas a factores clínicos como crecimiento y ruptura del aneurisma.

Capitulo 2: Estimación del movimiento de pared en aneurismas intracraneales

En este capítulo se han combinado métodos de corregistro no rígido con técnicas de procesado de señales para cuantificar el movimiento de pared a partir de secuencias angiográficas. Hasta nuestro conocimiento, esta es la primera vez que la pulsación es cuantificada de manera continua a lo largo del ciclo cardíaco.

La metodología presentada fue aplicada a un grupo de secuencias y se ha encontrado que la diferencia de pulsación entre el aneurisma y la arteria es mayor en aneurismas rotos que en aneurismas no rotos. Esta observación es consistente con diferencias histológicas de la pared vascular encontradas en la literatura. Estas mediciones y observaciones pueden ayudar a estratificar el riesgo de ruptura, y a comprender los efectos del movimiento de pared sobre la hemodinámica y evolución de los aneurismas.

Varios aspectos planteados en el Capítulo 1 como posibles mejoras de la técnica de medición han sido desarrollados en mayor profundidad, y confirmando las hipótesis planteadas. En particular, el uso de mayores frecuencias de muestreo para obtener una curva de distensión continua, la conexión entre pulsación y estado de ruptura, y la aplicación de la metodología a un número mayor de casos para obtener rangos de variación de la distensión en aneurismas cerebrales.

Capitulo 3: Estimación de movimiento cardíaco mediante wavelets complejas

La información espacial presente en imágenes de resonancia magnética marcada fue introducida en métodos de corregistro mediante el uso de vectores de características formados con los coeficientes de la transformada wavelet compleja (CWT). Esta representación de imágenes es invariante al desplazamiento, discrimina correctamente direcciones espaciales, y es intrínsecamente multiresolución. Estas propiedades resultan deseables en el contexto de corregistro de imágenes.

El uso de la CWT ha permitido obtener errores menores con respecto a la wavelet de Haar e intensidad de pixel, lo cual sugiere que la inclusión de información espacial podría ser relevante para guiar el proceso de corregistro. El punto débil de esta metodología es su elevado costo computacional debido al cálculo de la CWT y al estimador de la métrica, lo

cual podría limitar su aplicación práctica a las secuencias 3D + t disponibles en la práctica clínica.

Capitulo 4: Estimación de movimiento cardíaco mediante corregistro conjunto de imágenes.

En este capítulo hemos estimado el movimiento cardíaco mediante el corregistro conjunto de las imágenes componentes de secuencias de T-MRI. La utilización de H_α conjunta en lugar de métricas definidas entre pares de imágenes fue justificado mediante desde un punto de vista probabilístico en la Section 4.2.3. Para resolver el problema del elevado costo computacional de los estimadores basados en kNNG, se ha derivado una expresión analítica para el gradiente de la métrica, obteniendo como resultado una drástica reducción en el tiempo de corregistro. La estrategia utilizada para combinar diferentes vistas proporcionó los resultados esperados, y resulta una manera simple de integrar diferentes canales de información en una métrica única.

Los resultados obtenidos mostraron errores significativamente menores, y menores varianzas con respecto al método de referencia. Aun cuando se esperaba una distribución temporal uniforme del error, este presentó un incremento durante la sístole. Estas observaciones fueron relacionadas a artefactos y métodos de adquisición de secuencias 3D, los cuales podrían ser parcialmente resueltos mediante adquisiciones 3D reales [102]. Los valores de deformaciones obtenidos para sujetos sanos se encuentran en el orden de magnitud encontrado en la literatura. Sin embargo, la falta de estandarización, y las diferentes fuentes de variabilidad dificultan una comparación directa. En pacientes con infarto agudo de miocardio, se observó una correlación entre deformación, localización del infarto, y regiones en riesgo. Se necesitan experimentos adicionales sobre un número mayor de pacientes para confirmar y generalizar estas conclusiones clínicas.

Capitulo 5: Análisis de deformaciones en el infarto agudo de miocardio

En este estudio se ha aplicado el método presentado en el capítulo 4, para estudiar las relaciones entre deformación, localización del infarto, y oclusión coronaria. Los resultados proporcionados por el método son consistentes con el conocimiento actual de la fisio y fisiopatología cardíaca. Las deformaciones obtenidas para el grupo de control se encuentran en concordancia con los modos básicos de contracción del ventrículo izquierdo durante la sístole. Las deformaciones estimadas dentro de las regiones con infarto de miocardio fueron inferiores al promedio del grupo de control en la región correspondiente. Un hallazgo interesante fue la disminución de la deformación en las regiones en riesgo, lo cual sugiere el uso potencial de la deformación como índice de riesgo de infarto, o como indicador de evolución luego de una intervención coronaria. La metodología presentada puede beneficiarse de avances en métodos de segmentación de cámaras cardíacas y extensión del infarto.

Acknowledgements

I would like to thank the following persons and institutions:

Thesis director, Alejandro F. Frangi.

Members of the jury

European reviewers: Vincent Noblet (Centre National de la Recherche Scientifique), and Jean-Paul Armspach (Institut de Physique Biologique)

Colaborators: Laura Dempere-Marco (Pompeu Fabra University), Juan R. Cebral y Marcelo Castro (George Mason University), Hildur Ólafsdóttir (Technical University of Denmark), Alfred O. Hero (University of Michigan), and David Barber (University of Sheffield).

François Rousseau, special thanks for his unvaluable help for finishing this thesis.

Spanish Ministry of Education, for the financial support.

Sebastián Ordás, my collegue and great friend who teached me to see the whole picture, to love and enjoy the work, and to become strong in the adversity.

My wife Nadège, for her inconditional support, comprehension, and patience during these years. And for giving me Valerio, who makes happy each second of my life.

My family in Argentina, who saw me leave the country looking for new horizons. Specially my son Juan Cruz, from whom I was separed for a long time.